Search for Supersymmetry in events with jets and missing energy at the LHC

Chris Lucas

School of Physics

University of Bristol

This dissertation is submitted for the degree of

Doctor of Philosophy

2015

Declaration

I, Chris Lucas, declare that the work in this dissertation was carried out in accordance with the requirements of the University's Regulations and Code of Practice for Research Degree Programmes and that it has not been submitted for any other academic award. Except where indicated by specific reference in the text, the work is the candidate's own work, or where the candidate has been the major contributor. This work has been carried out within the context of the University of Bristol CMS group and the CMS SUSY working group, itself a part of the CMS collaboration. Any views expressed in the dissertation are those of the author.

Signed: ____

Date: ____

Acknowledgements

As I sit here in my kitchen, after having read my thesis for what feels like the thousandth time, I'm left with the intimidating task of writing these final words - intimidating because there is no possible way I can portray enough my incredible grattitude to the countless number of people that have helped me get to the point I find myself in today.

I would like to thank the many people I have had the pleasure of working with over the last three and half years. In particular those in the RA1 team, notably Darren Burton, Bryn Mathias, Yossof Eshaq, Edward Laird and Zhaoxia Meng, each for the seemingly unending patience and help they've shown me throughout my work. Of course, it is to Rob Bainbridge that I owe an incredible deal - not only for his constant guidance and supervision throughout our work together, but also for what is quite possibly the longest skype conversation history since the dawn of the internet. I also extend a great deal of thanks to my supervisor Henning Flaecher for helping me throughout my PhD with continual support and challenging discussions. Also for the seemingly vast number of thesis iterations and corrections, I'm considerably greatful.

My fellow PhD students with whom I've experienced both the highs and lows of the PhD experience, have always been there to bring me back around with a laugh and a beer. Especially Emyr Clement, Jeson Jacob, Sam Harnew, Daniel Souza and Donal Hill - I thank you.

Also I am incredibly grateful to the many friends and housemates that have helped me, likely without even realising the importance of their actions, by providing such a welcome and great relief from the research world. There are far too many of you to name, but I'm sure you know who you are.

Of course, I couldn't go a whole round of thanks without mentioning the big man himself, Allan 'Ken' Lehan. For the far too many evenings spent drinking far too many whiskies and chain-watching far too many episodes of The Wire, I am hugely grateful (despite most of Season 3 still being a hazey memory). I take back everything I've ever said - you're alright.

Finally, I would like to extend the greatest of thanks to my family, without whom I simply wouldn't be in the position I am, or the person I've become today. There's not a day goes by that I'm not thankful to have such incredible parents who have encouraged and believed in me always, without fail. For your incredible never-ending love and support I will perpetually be in debt to you.

For my Dad.

I hope this is worth a McDonalds breakfast.

The work of basic scientists like Hertz,
Dobson, and Kaplan can only be driven
by curiosity, not purpose.
What is the value of a particular curiosity?
There is no way to know in advance.
Discovery is curiosity's product; everything else,
including immeasurable economic value, follows.
We cannot know the worth of something
we have not yet discovered.
The joy is the rainbow,
not the hope of gold at the rainbow's end.

Unknown author

Abstract

A search for Supersymmetry in the jets and missing energy final state is described using the CMS detector at the LHC, and the full 18.5 fb^{-1}‘Parked’ dataset of $\sqrt{s} = 8$ TeV proton-proton collisions. This dataset was collected using experimental, low-threshold triggers to increase sensitivity to softly decaying new physics signatures. The search makes use of the kinematic variable, α_{T}, to reduce contributions from QCD multijet processes by many orders of magnitude, to a level considered negligible. Remaining background sources originate from electroweak decays of heavy bosons and top quarks, and are estimated using a data-driven technique employing dedicated control regions. To maintain sensitivity to a broad range of potential manifestations of Supersymmetry, the analysis categorises events in dimensions of the scalar sum of hadronic energy, the number of jets and the number of jets originating from b quarks. While this analysis aims to remain inclusive to many hadronically decaying SUSY signatures, the work in this thesis exploits the low energy thresholds of the ‘Parked’ triggers and therefore considers models with compressed mass spectra. As no statistically significant excess is observed, results are interpreted within the context of decays of stop particles relevant in the compressed spectra region. Stop decays to charm quarks and via four-body decays to fermions are considered, both with the weakly interacting Lightest SUSY Particle in the final state. Limits are placed on the mass of the stop of up to 275 GeV for the charm decay and up to 250 GeV for the four-body decay. Natural units ($\hbar = c = 1$) are used throughout this work.

Table of contents

List of figures

List of tables

Chapter 1

Introduction

Our instinctive method of understanding is reductive - the idea of an inventor attempting to make sense of the things around them is that of toasters, clock radios, or even gearboxes broken down into their smallest constituent parts to better understand what they're made of and, ultimately, what's happening inside of them. This simple idea translates perfectly to explain the work Particle Physicists undertake with not simple everyday objects, but the Universe.

Since the fields inception, physicists have questioned the Universe around us, and what it's made of. From the early research of scientists such as Ernest Rutherford and Niels Bohr, the basic building blocks of the universe have been searched for. For Particle Physicists, this is the ultimate goal - a complete understanding of the nature of the Universe at it's most fundamental level. If a description can be written of the smallest building blocks of nature and how they interact, then ultimately we can understand the Universe from the bottom up.

Currently, our best attempt of such a description comes from the intersection of two very different fields: Quantum Mechanics, the study of microscopic objects, and Relativity, the study of very fast objects. The combination of these two contrasting worlds gave birth to the field of Relativistic Quantum Mechanics, and ultimately, the Standard Model.

First proposed in the 1960s, the Standard Model describes the properties of the fundamental constituents of matter, and outlines their interactions through three of the four fundamental forces of nature, as described in chapter 2. Through it's accurate description and predictions of not only particles such as the electrons, quarks and gluons of which atoms are composed, as well as fundamental constants of nature such as the fine structure constant α, the Standard Model has exceptionally proven itself to be a triumph of modern physics.

Despite its continued accuracy in the face of substantial scrutiny, however, the Standard Model fails to account for significant observations, for example the absent description of gravity and the 'other' 96% of the Universe - the so-called 'Dark Sector'. Similarly the Standard Model fails to unify the fundamental forces at some higher mass scale, or predict the masses of particles, such as the newly discovered Higgs boson. As such, given how successfully it describes what it can, the SM is widely considered as a smaller component of some greater, all-encompassing theory. This belief has led many to use this distinct theory as a building block on which extensions can be introduced to create Beyond the Standard Model (BSM) theories - the goal being to fill the gaps in knowledge left by the SM.

Of the plethora of BSM theories, one particularly well motivated extension is Supersymmetry (SUSY). The Supersymmetric extension to the Standard Model introduces supersymmetryic particles (or 'sparticles') differing from their SM partners by half a unit of spin - described in greater detail in chapter 2. The addition of sparticles fixes many of the Standard Model's problems, most notably that of the divergent Higgs Mass, the Unification of the fundamental gauge couplings and, crucially, provides a feasible candidate particle for the elusive Dark Matter observed in abundance in the Universe.

Particle physics as a field has developed largely via a cat and mouse game, played out between theorists and experimentalists. While theoretical physicists have developed new theories and proposed new particles, experimentalists have raced to build greater and more advanced experiments with which to discover them, and vice-versa. Today, thanks to the incredible work of thousands of physicists and engineers, we are able to test such BSM theories with the Large Hadron Collider (LHC) in Geneva, Switzerland.

The LHC, described in chapter 3, is a 27 km circumference proton synchrotron, capable of colliding protons at centre-of-mass energies far exceeding any previous experiment. Using the LHC, it is possible to reproduce the conditions observed a short time after the Big Bang, where the incredibly high energies present were able to produce countless particles that wouldn't be visible in today's universe. If such exotic particles are created in the proton-proton collisions performed at the LHC, it is the goal of detector experiments such as the Compact Muon Solenoid (CMS) to find them.

The CMS detector, also described in chapter 3, is comprised of multiple subdetector systems, each designed specifically to make precise measurements of the characteristics of the different particles created in the fierce collisions. The detector is built such that it provides almost complete hermetic coverage to detect particles travelling in all directions from the point of interaction. Energy deposits throughout the detector subsystems are used to form physics objects, as summarised in chapter 4, themselves allowing the events to be categorised by the physics processes present.

A key technique for searches for SUSY is the study of global momentum imbalances, which allows for the presence of weakly interacting particles to be inferred. If sparticles were to be produced at the LHC they would likely decay immediately to many well-understood SM particles, and finally the weakly interacting 'Lightest Supersymmetric Particle' (LSP) - the theory's Dark Matter candidate. Of the many different possible supersymmetric decays, hadronic channels offer the largest branching fractions, although can present some of the most difficult experimental challenges. Hadronic searches are of interest given their relatively simple and quick ability to provide sensitivity to early discovery at hadronic colliders such as the LHC.

The work described in this thesis consists of such a search for SUSY particles decaying to quarks and missing-energy. The analysis makes use of the full 'Parked' data sample collected throughout 2012, where experimental triggers collected events with lower energy thresholds than the standard data stream. These lowered thresholds greatly improve analysis sensitivity to soft physics processes, such as those expected from SUSY scenarios with nearly degenerate mass hierarchies. The data samples and corresponding MonteCarlo simulated samples used in this analysis are detailed in chapter 5.

The biggest obstacle to searching for hadronic signatures of new physics, is dealing with the overwhelming hadronic backgrounds from Quantum Chromodynamics (QCD). In this analysis a powerful kinematic variable, α_{T}, is used to differentiate between such QCD and potential signal events. The analysis backgrounds, selection and the α_{T} variable are described at length in chapter 6. The remaining SM sources of background are estimated using a data-driven transfer technique from dedicated control samples, orthogonal to the search region, as outlined in chapter 7. The results of the transfer technique are included as part of a simultaneous likelihood model fit to the signal and all control samples to determine final background counts as described in chapter 8.

Given the vast number of potential manifestations of SUSY, sparticles may decay in many different ways if produced. Accordingly, chapter 8 also gives the results of this analysis, categorising events in dimensions of three different event-level variables: the total sum of visible transverse hadronic energy, the number of jets and the number of b-tagged jets. Specific analysis categories are used to produce targeted interpretations of different potential final states, thereby maintaining a broad sensitivity to SUSY production, however it may present itself in nature. As motivated by Dark Matter observations, the interpretations presented in this thesis represent two different decay channels of the produced $\widetilde{t}$ sparticle in the so-called 'compressed' region, where the mass of the $\widetilde{t}$ is near-degenerate with that of the LSP. Accordingly, upper limits on the mass of the $\widetilde{t}$ and the LSP are produced. These interpretations and discussions of the related efficiencies and systematics are presented in chapter 9, before final conclusions are made in chapter 10.

Chapter 2

Theoretical Overview

The Standard Model (SM), proposed in the 1960s, has long been the most prominent and successful description of fundamental particles and their interactions at the energies currently experimentally accessible. Its power has been proven with the theoretical prediction of particles such as the charm and top quarks, and the W and Z bosons, prior to their experimental observation. Furthermore, precision electroweak measurements have shown impressive levels of agreement with SM predictions [13].

However, despite its great success, the theory is known to be valid only for low energies, and is missing significant details of both experimentally observed and theoretically predicted physical phenomena. As such, extensions to the SM have been extensively studied, assuming the SM to be the low-energy regime of some greater theory. One such strongly theoretically motivated extension to the SM is Supersymmetry (SUSY).

This chapter first outlines the SM model, including its particle content and basic mechanisms, before describing its shortcomings - the theoretical motivation for Beyond the Standard Model (BSM) theories. SUSY will then be introduced, before describing its simplest incarnations, along with a discussion of the specific models and frameworks used for interpretation within this analysis.

2.1 The Standard Model

The Standard Model is a renormalisable Quantum Field Theory describing fundamental matter particles and their interactions via the strong, weak and electromagnetic forces. It was collaboratively developed throughout the 1960s [14–18], with its current Lagrangian based formalism being finalised in the mid-1970s [19].

Requiring local gauge invariance of the SM Lagrangian, $\mathcal{L}_{SM}$, under transformations generated by universal space-time symmetry groups, interactions can be described via conserved quantities. The $SU(3)$ group describes strong force interactions through colour charge, and $SU(2)$ and $U(1)$ to describe electroweak interactions through weak isospin and hypercharge respectively.

Matter particles, summarised in table 2.1, are described by spin 1/2 fermions divided into the six quarks and six leptons. The quarks are arranged into three generations: the up(u) and down(d), the charm(c) and strange(s), and the top(t) and bottom(b), each couplet carrying individual electric charges of +2/3 and -1/2 respectively. The quarks also carry colour charge, where combinations of quarks form colour-neutral composite hadron particles which are observed in nature.

The leptons are similarly arranged into three generations, constructed from $SU(2)$ doublets of weak isospin, $(\nu_L, l)_L$, of left-handed chiral states, and singlets, l_R, of right-handed chiral states, where l represents either the electron (e), muon (μ) or tau (τ), each carrying a -1 electrical charge, and ν_L being their corresponding electrically neutral neutrinos.

Table 2.1 The fermionic particle content of the Standard Model [12].

Name	Type	Spin	Charge (e)	Mass
Electron (e)	Lepton	1/2	-1	0.511 MeV
Electron Neutrino (μ_e)	Lepton	1/2	0	$<$ 2 eV
Muon (μ)	Lepton	1/2	-1	105.658 MeV
Muon Neutrino (ν_μ)	Lepton	1/2	0	$<$ 0.19 MeV
Tau (τ)	Lepton	1/2	-1	1.776 GeV
Tau Neutrino (ν_τ)	Lepton	1/2	0	$<$ 18.2 MeV
Up (u)	Quark	1/2	+2/3	$2.3^{+0.7}_{-0.5}$ MeV
Down (d)	Quark	1/2	-1/3	$4.8^{+0.5}_{-0.3}$ MeV
Charm (c)	Quark	1/2	+2/3	1.28 ± 0.03 GeV
Strange (s)	Quark	1/2	-1/3	95.0 ± 5.0 MeV
Top (t)	Quark	1/2	+2/3	173.21 ± 0.87 GeV
Bottom (b)	Quark	1/2	-1/3	4.66 ± 0.03 GeV

Interactions between the fermions are mediated by spin-1 bosons, summarised in table 2.2. The strong force, $SU(3)$, is represented by eight electrically neutral, massless gluons (g), each carrying a colour charge. The electroweak force, $SU(2) \times U(1)$, is mediated by the electrically neutral, massless photon (γ), the massive, neutral Z^0, and the massive, electrically charged $W^{\pm}$ bosons.

Following the enforcement of local gauge invariance after an $SU(2) \times U(1)$ trans-

Table 2.2 The bosonic particle content of the Standard Model [12].

Name	Force Carried	Spin	Charge (e)	Mass
W Boson (W)	Weak	1	± 1	80.385 ± 0.02 GeV
Z Boson (Z)	Weak	1	0	91.188 ± 0.002 GeV
Gluon (g)	Strong	1/2	0	-
Photon (γ)	Electromagentism	0	0	-
Higgs Boson (H)	-	0	0	125.7 ± 0.4 GeV

formation, the bosonic mediator of the $U(1)$ symmetry, the γ, remains massless as expected, however so do the $W^{\pm}$ and Z^0, in disagreement with their experimentally observed masses. To remedy this, the $SU(2) \times U(1)$ symmetry undergoes Electroweak Symmetry Breaking (EWSB) via the Higgs Mechanism [20–22], leading to the Higgs boson, H^0, a massive, electrically neutral, spin-0 scalar particle, thereby completing the formalism of the Standard Model.

2.1.1 Failings of the Standard Model

While the Standard Model has provided many accurate predictions and descriptions which have been extensively experimentally verified [23], the theory is considered incomplete due to gaps in its description of the Universe.

The SM provides a QFT description of how the strong, weak and electromagnetic forces work on a quantum level, however it fails to include any description of the final fundamental force, gravity. A quantum description of gravity has long been sought after by particle theorists, in particular to provide an explanation for its relative weakness at the Electroweak scale with respect to the other fundamental forces.

Following the Big Bang it is believed matter and anti-matter were created in equal amounts, however given that we are in a matter dominated universe there must exist some physical process by which an asymmetry came to be between the two types of matter - the so-called ‘Baryogenesis’ process. This could be described by violation of the Charge-Parity (CP) symmetry, however the amount of CP violation described by the Standard Model does not appear to be significant enough to achieve this [24, 25].

In the SM, following the local gauge invariance requirement of the electroweak sector, $SU(2) \times U(1)$, the $SU(2)$ doublets contain massless neutrino particles. However, experimental observations of neutrino oscillation between their various flavours indicate them to have finite mass [26, 27], and therefore mix between different mass eigenstates. This is only described by extending the Standard Model to include neu-

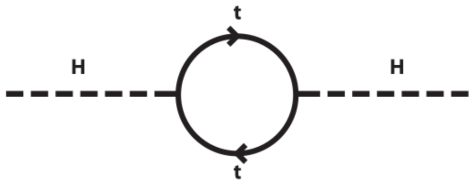

Fig. 2.1 Quantum self-corrections to the Higgs mass from a fermionic top quark loop.

trino mixing, defined by the PMNS matrix [28].

Furthermore, and of particular relevance to the work in this this thesis, are the Hierarchy Problem and the existence of Dark Matter.

The Hierarchy Problem

Particles couple to the Higgs field according to the Yukawa couplings, λ_f, proportional to the mass of the particle. For fermions, the Lagrangian interaction term is

$$\mathcal{L}_{\text{Yukawa}} = -\lambda_f \bar{\Psi} H \Psi, \tag{2.1}$$

where Ψ is a spin-1/2 Dirac field, and H the Higgs field. Higgs mass corrections due to beyond tree-level interactions with fermion fields (shown in figure 2.1) can be shown to result in

$$\Delta m_H^2 \propto -|\lambda_f|^2 \Lambda_{\text{cut}}^2, \tag{2.2}$$

where Λ_{cut} is the cut-off energy scale, up to which the SM is valid, typically taken to be the Planck scale. This therefore leads to a quadratically divergent correction to m_H. Such corrections cause significant tension between the theoretically allowed value of m_H and the experimentally measured value, $m_H \simeq 125$ GeV [29], requiring significant 'fine-tuning' to bring the two into agreement. This disagreement is known as the Hierarchy Problem.

Dark Matter

Significant amounts of Dark Matter (DM) have been indirectly observed through the study of galaxy rotation curves and gravitational lensing techniques [30]. It is estimated that Dark Matter represents 26.8% of the Universe, with normal Baryonic matter representing only 4.9% [31]. For such a large relative abundance to be present DM must be massive and weakly interacting. No candidate particle exists in the SM to describe such matter.

2.2 Supersymmetry

At its core, Supersymmetry is a new space-time symmetry between fermions and bosons [32–37]. An operator of SUSY acting on a fermion (resp. boson) state acts to change the spin by a 1/2, producing a super-partner boson (resp. fermion) state, maintaining electric charge, colour charge and weak isospin. A theory invariant under such transformations is said to be supersymmetric.

As a consequence of this new symmetry, SUSY introduces a rich phenomenology of new particles ('sparticles'). The simplest implementation of SUSY is the Minimally Supersymmetryic Standard Model (MSSM) [1] - a so-called 'complete' model, containing more than 100 free-parameters representing sparticle masses, phases and mixing angles [38]. Within the MSSM, the SU(2) doublets and singlets, $(\nu_L, l)_L$ and l_R, have super-partners $(\tilde{\nu}_L, \tilde{l})_L$ and $\tilde{l}_R$. Similarly for SU(3), $(q, q')_L$ and q_R, have super-partners $(\tilde{q}_L, \tilde{q}')_L$ and $\tilde{q}'_R$. The spin-1 SM gauge bosons have spin-1/2 gaugino partners, the gluino, winos and bino, $\tilde{g}$, $\tilde{W}^{\pm}$, $\tilde{W}^0$, $\tilde{B}^0$. The Higgs sector is extended to include two Higgs-doublets giving five mass-eigenstates, h^0, H^0, A^0 and $H^{\pm}$. Finally, the gauginos and the neutral higgsinos mix to give the neutralinos, $\tilde{\chi}^0_{i=1-4}$, and the winos and charged higgsinos mix to give the charginos, $\tilde{\chi}^{\pm}_{i=1-2}$.

Table 2.3 The particle content of the Minimally Supersymmetric Standard Model. Note that there are now two Higgs doublets present.

Sparticle	Partner	Spin	Charge (e)
$\widetilde{\chi}^0_0, \widetilde{\chi}^0_1, \widetilde{\chi}^0_2, \widetilde{\chi}^0_3$	γ, Z, H^0, h^0	1/2	0
$\widetilde{\chi}^{\pm}_0, \widetilde{\chi}^{\pm}_1$	$W^{\pm}, H^{\pm}$	1/2	±1
$\widetilde{e_{\bar{L}}}, \widetilde{e_{\bar{R}}}, \widetilde{\nu_e}, \widetilde{\mu_{\bar{L}}}$, $\widetilde{\mu_{\bar{R}}}, \widetilde{\nu_\mu}, \widetilde{\nu_\tau}$	$e, \nu_e, \mu, \nu_\mu, \nu_\tau$	1	±1, 0
$\widetilde{\tau}_L, \widetilde{\tau}_R$	τ	1	±1
$\widetilde{u_L}, \widetilde{u_R}, \widetilde{d_L}, \widetilde{d_R}$, $\widetilde{s_L}, \widetilde{s_R}, \widetilde{c_L}, \widetilde{c_R}$	u, d, s, c	1	$\pm1/3, \pm2/3$
$\widetilde{b_L}, \widetilde{b_R}$	b	1	$\pm1/3, \pm2/3$
$\widetilde{t_L}, \widetilde{t_R}$	t	1	$\pm1/3, \pm2/3$
$\widetilde{g}$	g	1/2	0

Given the lack of experimental evidence for SUSY, sparticles must have higher masses than their SM partners, implying that Supersymmetry is not an exact symmetry and must be broken by some mechanism [39, 40].

2.2.1 Why SUSY?

The Supersymmetric extension to the SM provides solutions to many of the original theory's shortcomings.

Unification of the Gauge Couplings

Within a Grand Unified Theory (GUT) it is desirable for the running constants related to the gauge couplings to unify at some higher energy scale. While not possible in the SM, with the introduction of a supersymmetric extension, such as the MSSM, the strength parameters are indeed able at some higher energy scale, as shown in figure 2.2.

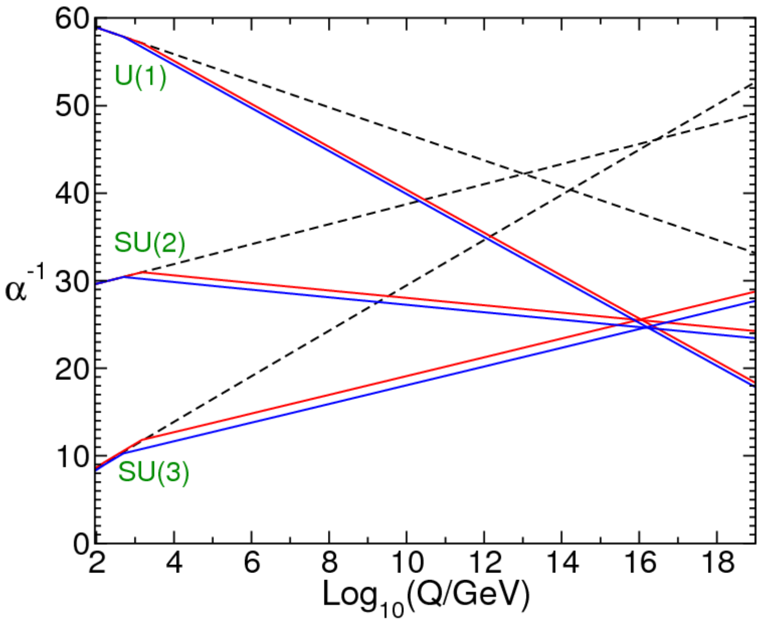

Fig. 2.2 The strengths of the gauge coupling parameters, α^{-1}_{1-3}, as a function of the energy scale Q. Dashed lines show the form of the couplings under a SM-only assumption, whereas the coloured lines show their form with the inclusion of the MSSM. [1]

Hierarchy Problem

While in the SM the Higgs gains corrections to its mass from fermion-loop induced self-interactions, the presence of bosonic super-partners to these fermions in a SUSY model provides additional diagrams (figure 2.3), which contribute oppositely signed terms,

$$\Delta m_H^2 \propto +\lambda_S \Lambda_{\mathrm{cut}}^2, \tag{2.3}$$

where λ_S is the bosonic super-partner's Yukawa coupling. The introduction of these super-partners, and therefore their additional corrective terms, provides an elegant solution to the hierarchy problem. Quadratic divergences to m_H are effectively cancelled by sparticle loop contributions, with only a logarithmic divergence remaining, arising due to the necessity of breaking SUSY.

Fig. 2.3 Quantum self-corrections to the Higgs mass from a bosonic stop loop.

Dark Matter

In many supersymmetric theories, a new conserved quantum number R_P is introduced in order to conserve lepton and baryon number [41], defined as

$$R_P = (-1)^{3B+L+2s} \left(= \begin{array}{l} +1 \text{ for SM particles} \\ -1 \text{ for SUSY particles} \end{array} \right), \tag{2.4}$$

where B is Baryon number, L is Lepton number and s is spin. SM particles have $R_P = +1$, whereas SUSY particles have $R_P = -1$. R_P is a multiplicative quantum number, therefore sparticles can only be pair-produced. The subsequent sparticle decay will therefore consist of a cascade-type decay, with each sparticle decaying to a final state containing a lighter, kinematically accessible sparticle and a SM particle. This process will continue until the lightest supersymmetric particle (LSP) is reached, which is therefore stable. Within R-Parity conserving models in which the $\widetilde{\chi}^0$ is the LSP, this particle is able to provide a stable, weakly interacting dark matter candidate [42].

2.2.2 Experimental Consequences

In order for SUSY to provide an adequate solution to the hierarchy problem, sparticle masses are required to be around the TeV scale [39, 40, 43]. This fact, coupled with strong experimental bounds on constrained models and the discovery of the Higgs in a mass-region compatible with the MSSM, have led interest towards 'Natural' SUSY models. Such models negate the limits imposed by experimental constraints by assuming the first and second generation squarks to be very heavy, while the third generation be around 1 TeV in order to solve the hierarchy problem without significant fine-tuning [44, 45].

2.2.3 Simplified Model Spectra

While 'complete' supersymmetric models offer a full description of all aspects of a given theory (e.g. mass spectra and mixing angles), the large number of free parameters becomes unmanageable for interpretations of experimental observations. Even in models such as the Constrained-MSSM (CMSSM) with 5 free parameters [46, 47], the interpretation phase-space remains vast.

In an effort to make interpretations of experimental data simpler for experimentalists, while remaining universally of use to theorists, Simplified Model Spectra (SMS) were developed [48, 49]. SMS consist of simplified decay scenarios which can later be reinterpreted within complete models. Typically SMS consist of either squark or gluino pair-production, with a subsequent decay to a given final state with a 100% branching fraction. A crucial consequence of these models is to effectively move experimental searches away from 'model-specific' interpretations and towards more 'signature-specific' interpretations [50].

SMS generally contain only two free parameters, normally the mass of a produced mother particle, m_{mother}, and the mass of the LSP, m_{LSP}. Therefore interpretations can be made over a simple 2-dimensional parameter space, making for trivial experimental comparisons.

SMS prove to be an excellent tool for the interpretation of results within the bounds of naturalness. Many SMS consider third generation squark production, allowing for direct limits to be placed on the dominant decays of stop and sbottom squarks.

2.2.4 Mass-degeneracy in the stop sector

SUSY models with particle mass hierarchies spanning a small mass range are said to be 'compressed'. When considered in terms of a simplified model scenario, this implies the pair-produced mother sparticle is close in mass to that of the LSP. The smaller the mass difference, Δm ($= m_{mother} - m_{LSP}$), the greater the experimental challenge, as visible decay products become softer and typically out of analysis acceptance.

In general, decay channels of the $\tilde{t}$ are dominated by $\tilde{t} \to b\tilde{\chi}^{\pm}$ and $\tilde{t} \to t\tilde{\chi}^{0}$. However, when $\Delta m <$ W-boson mass and a present W becomes off-shell, $\tilde{t}$ decay branching fractions become dominated by the two-body decay $\tilde{t} \to c\tilde{\chi}^{0}$, and the four-body decay $\tilde{t} \to bf\bar{f}'\tilde{\chi}^{0}$ [51]. In this region, these two decay channels can provide a dark-matter relic density consistent with cosmological observations (e.g. from WMAP [52]), where annihilation cross sections are mediated by co-annihilation with the light stop proposed by naturalness [53, 54].

This analysis will therefore focus on the two $\tilde{t}$ decays relevant in this highly-compressed region of SUSY phase space, namely the two-body charm decay ($\mathrm{pp} \to \tilde{t}\tilde{t}^{*} \to \mathrm{c}\tilde{\chi}^{0}\,\bar{\mathrm{c}}\tilde{\chi}^{0}$) and the four-body decay ($\mathrm{pp} \to \tilde{t}\tilde{t}^{*} \to \mathrm{b}ff'\tilde{\chi}^{0}\,\mathrm{b}ff'\tilde{\chi}^{0}$), shown in figure 2.4.

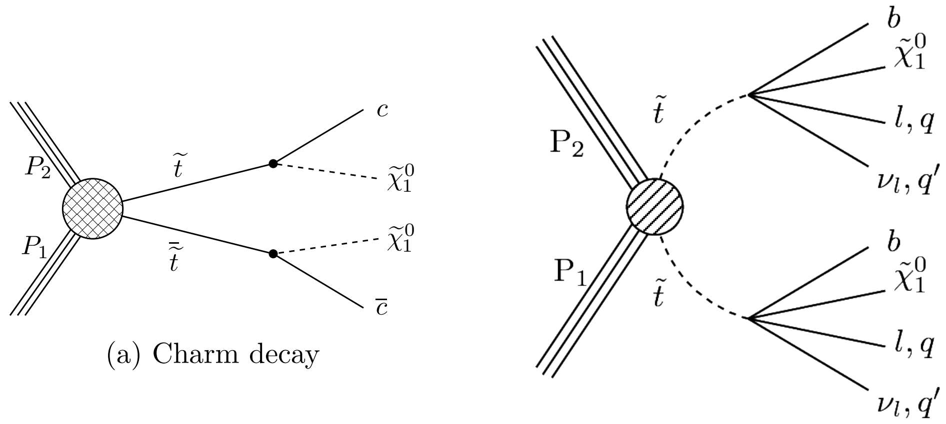

(a) Charm decay

(b) Four-body decay

Fig. 2.4 Feynman diagrams of the two SMS models considered.

Phenomenology

In the compressed region, characterised by small values of Δm, decay products of the $\tilde{t}$ pair have very low momenta given the small amounts of release in the decay following

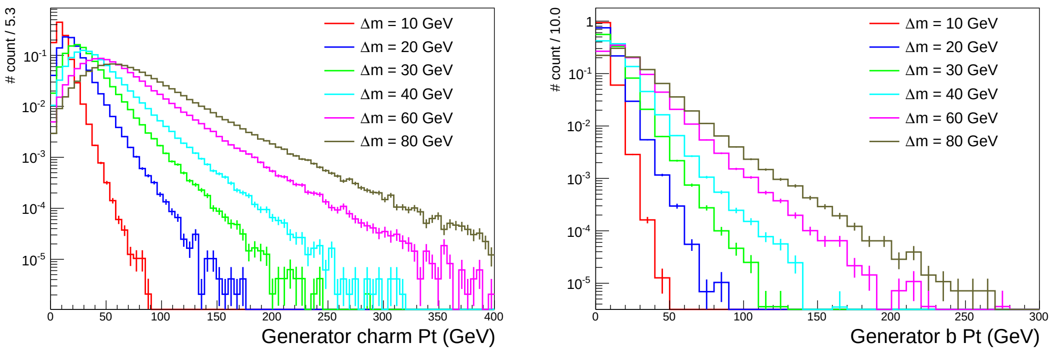

(a) Charm decay (b) Four-body decay

Fig. 2.5 Distributions of the generator level quarks produced in the two-body (left) and four-body (right) decays, prior to any event selection.

the production of the $\widetilde{\chi}^0$. For example, figure 2.5a shows the transverse momentum of the generator level charm quark originating from the decay of the $\widetilde{t}$ getting smaller with decreasing values of Δm. Figure 2.5b shows the same observation for the p_{T} of the b quark present from the decay of the $\widetilde{t}$ in the four-body decay.

The low amounts of available energy in the small Δm region present considerable experimental challenges, and as such this region in the past has typically not been considered for interpretations. The acceptance of such models in this region is heavily reliant on initial state particles radiated from the incoming partons, thereby boosting the decaying stops. This feature of compressed models and it's importance to analysis sensitivity is discussed later in chapter 9.

Current Experimental Limits

Given the current lack of experimental observation, limits for direct $\widetilde{t}$ production are shown in figure 2.6, with observed limits reaching up to $m_{\widetilde{t}} = 275$ GeV for the charm decay, and a similar reach for the four-body decay. In the both cases, sensitivity is largely restricted to extremal Δm values, with a weaker limit in the intermediate range.

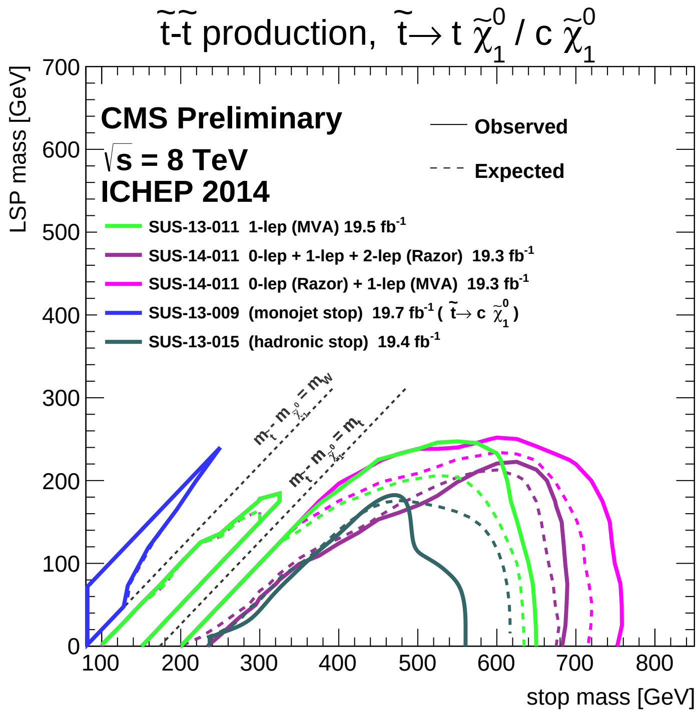

(a) CMS

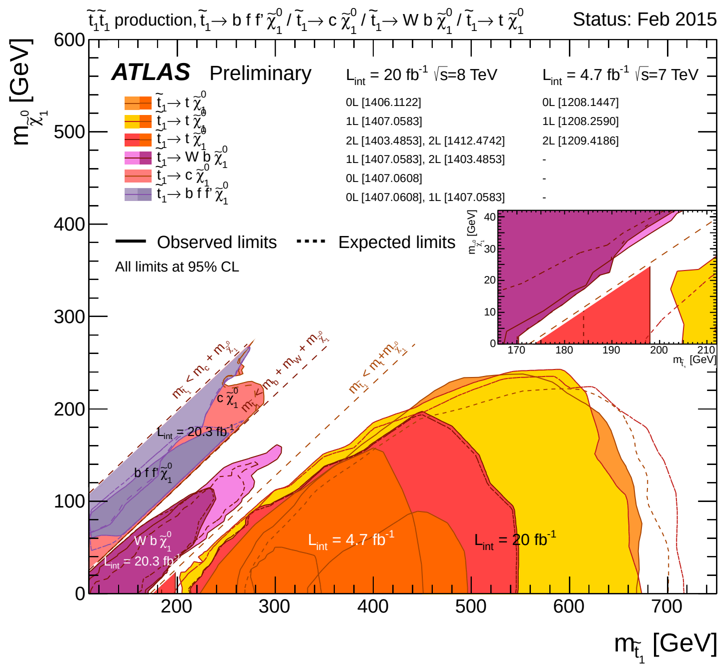

(b) ATLAS

Fig. 2.6 Current limits on direct stop production from the CMS (2.6a)[2] and ATLAS (2.6b)[3] experiments as a function of the $m_{\tilde{t}}$ vs. $m_{\tilde{\chi}^0}$ mass plane.

Chapter 3

The LHC and the CMS Detector

3.1 The Large Hadron Collider

The Large Hadron Collider (LHC) is a 27 km circumference proton-proton synchrotron with maximum design centre of mass energy $\sqrt{s} = 14$ TeV, described in detail elsewhere [55]. It is the highest energy component of the CERN accelerator complex, shown in figure 3.1. The LHC accelerates counter-rotating beams of protons using 400 MHz radio frequency (RF) cavities, focusses the beam using multiple quadrupole and higher order magnets, and maintains the beam trajectory using super-conducting, niobium-titanium dipole magnets, capable of producing an 8.4 T magnetic field. Such a high magnetic field is achieved by cooling the magnets to 1.9 K using super-fluid helium and applying a 11.85 kA electric current.

The beams, consisting of approximately up to 1380 bunches of $\mathcal{O}(10^{11})$ protons, are brought into collision at four points around the LHC ring within specialised detector systems, as shown in figure 3.2. During the first run of the LHC, 'Run I', bunches were spaced in 50 ns intervals, giving a bunch crossing rate of 20 MHz. Collisions proceed for a number of hours, while collision rates are maintained by scanning the transverse beam positions, until such a time when proton numbers are depleted and the beam recycled so that the fill process can be repeated.

The rate of collisions at each interaction point is described by the instantaneous luminosity, given by the equation:

$$L_{inst.} = \frac{f_{orbit} n_B N_p^2}{A_{eff}}, \tag{3.1}$$

where f_{orbit} is the orbital frequency of bunches in the LHC, n_B is the number of

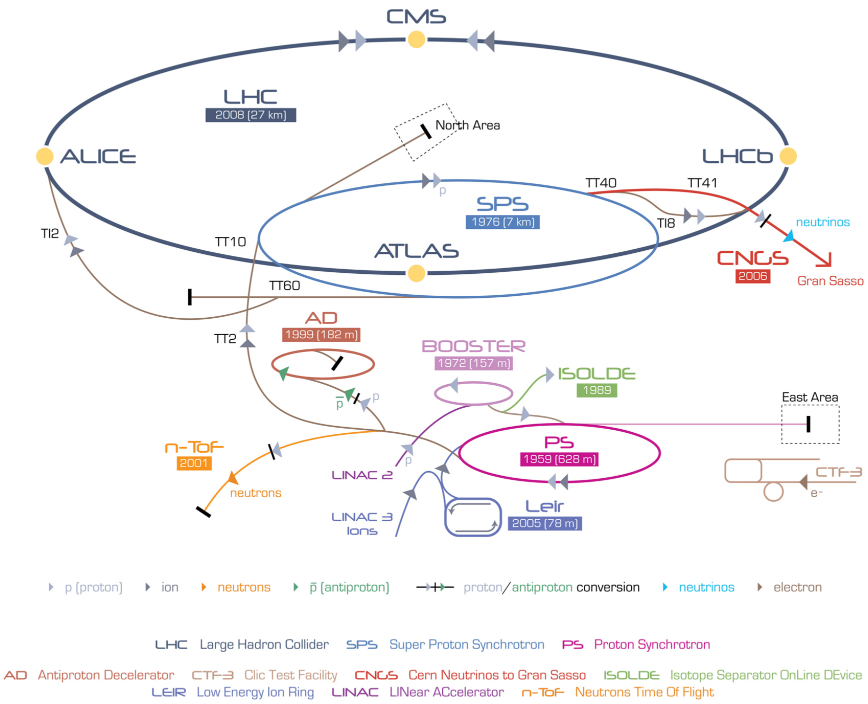

Fig. 3.1 Schematic diagram of the CERN accelerator complex, showing the various accelerators and storage rings, ultimately feeding the Large Hadron Collider [4].

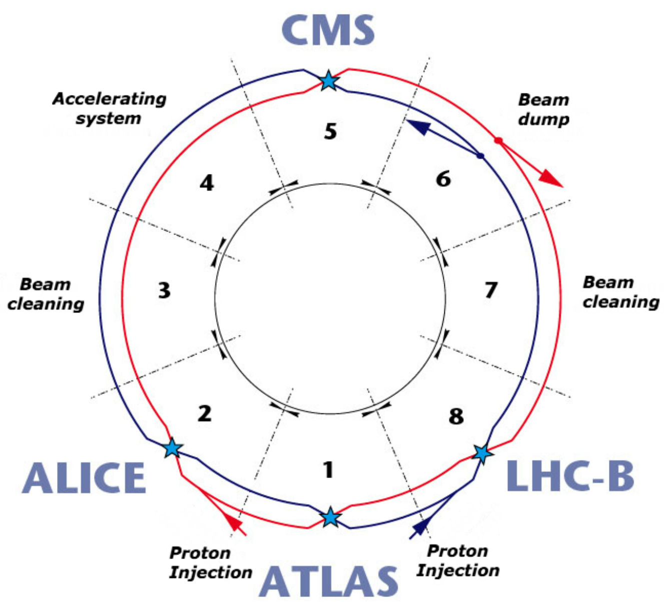

Fig. 3.2 Schematic diagram of the Large Hadron Collider, indicating the positions of the four collision points and their corresponding detector experiments [5].

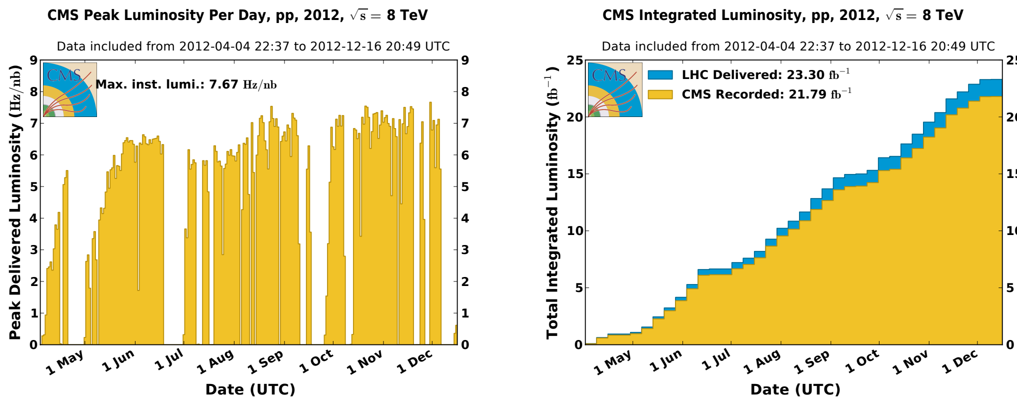

(a) (b)

Fig. 3.3 The peak instantaneous luminosity for each day throughout 2012 (a), and the integrated luminosity delivered to and recorded at CMS (b) [6].

bunches in the machine, N_p is the number of protons per bunch, and A_{eff} is the effective overlap area between colliding bunches. The peak $L_{inst.}$ per day for CMS is shown in figure 3.3a and the integral over time is shown in figure 3.3, both for the full run period through 2012.

Simultaneous interactions happening at the time of each bunch crossing are referred to as in-time pile up (PU), as opposed to overlapping particle decays from previous bunch crossings called out-of-time pile up (PU). Both phenomena cause significant experimental challenges for detector readout and event reconstruction. The average Pileup distribution for Run I is shown in figure 3.4.

3.2 Compact Muon Solenoid

The Compact Muon Solenoid (CMS), shown in figure 3.5, is a hermetic detector system optimised for the study on high-p_{T} objects and their decays [56]. It is designed to make accurate measurements of the positions and momenta of physics objects such as electrons, muons, taus, photons and jets. Owing to an almost complete 4π solid angle coverage, CMS is capable of also making accurate measurements of global momentum imbalances due to the presence of weakly interacting particles.

The cylindrical detector is 28 m in length, 15 m in diameter and has a mass of around 14,000 tonnes. The z-axis is taken to be the longitudinal dimension along the beamline, the x-axis the perpendicular direction pointing towards the centre of the LHC ring, and the y-axis pointing skywards, perpendicular to these forming a right-

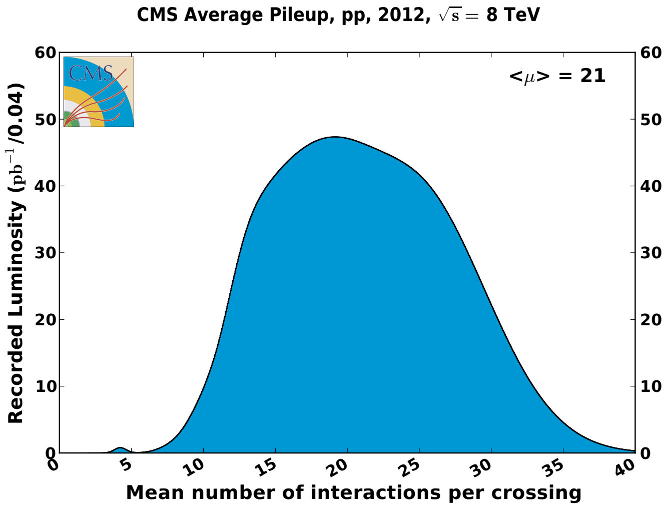

Fig. 3.4 The average Pileup distribution as seen by the CMS detector throughout Run I [6].

handed co-ordinate system. The transverse plane is taken to be the plane of the x and y axes.

Directions relative to the CMS detector are described with the variables ϕ, the angular direction in the transverse plane with range $[-\pi, \pi]$, and the Lorentz-invariant quantity 'pseudo-rapidity', η, describing an angle with respect to the z-axis, defined as:

$$\eta = -ln\ tan\left(\frac{\theta}{2}\right), \tag{3.2}$$

where θ is the polar angle between the particle trajectory and the beam pipe in the y-z plane. Differences in these two variables, namely $\Delta\phi$ and $\Delta\eta$, are invariant under Lorentz boosts, and so can be used to construct a furthermore Lorentz-invariant angular separation between particles:

$$\Delta R = \sqrt{(\Delta\eta)^2 + (\Delta\phi)^2}. \tag{3.3}$$

CMS is arranged in a layered configuration of sub-detectors, structured as a cylindrical barrel, completed by two end-caps. The barrel contains a super-conducting solenoid magnet capable of producing a 3.8 T magnetic field. Operated at 4.5 K, with a 18.5 kA current, the longitudinal field produced bends the trajectories of charged particles allowing for precise charge and momenta measurements.

The following sections describe each of the detector subsystems in more detail.

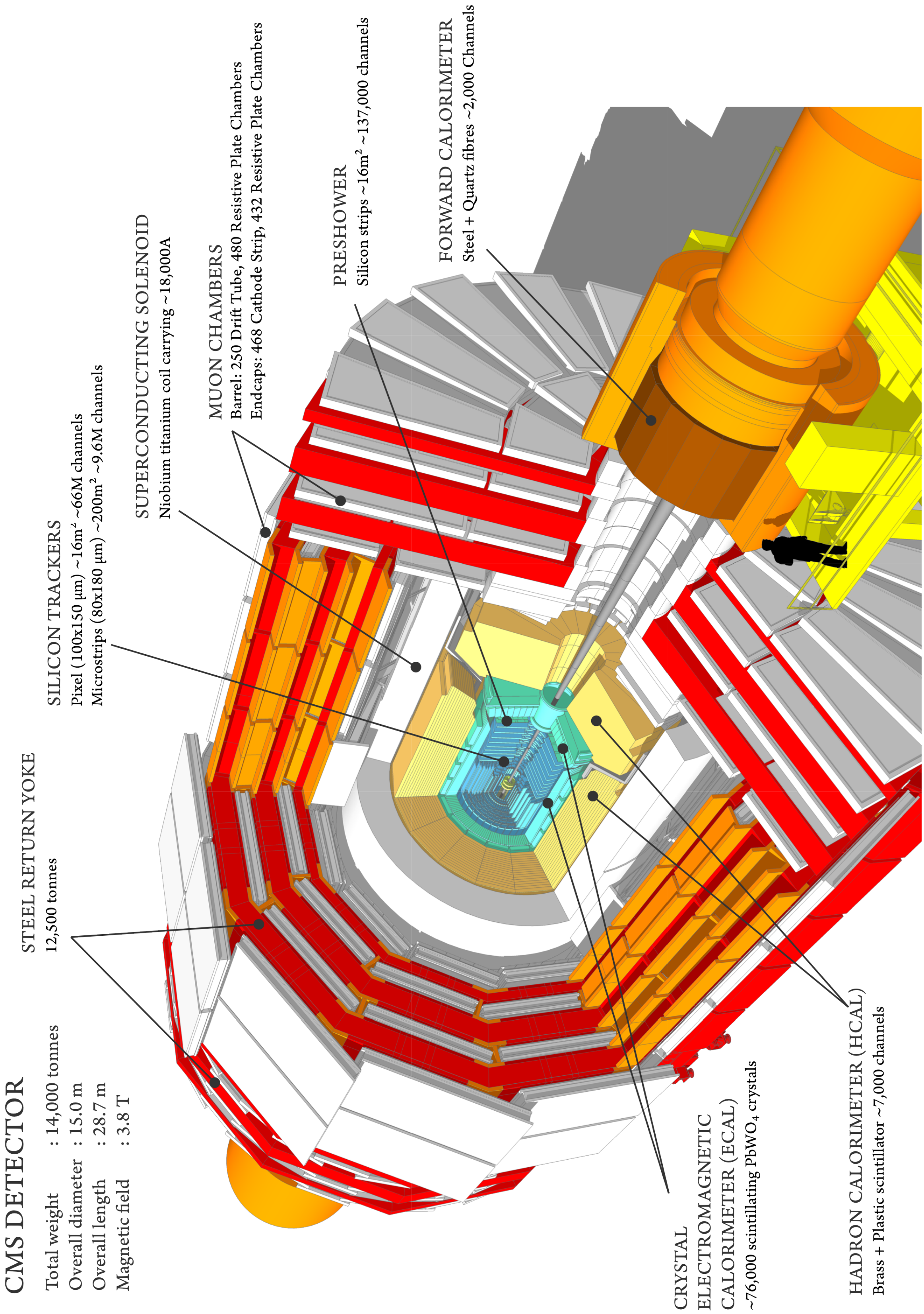

Fig. 3.5 Diagram of the Compact Muon Solenoid [7].

3.2.1 Tracker

The silicon tracker system consists of pixel-based inner and microstrip-based outer detectors.

The pixel detector consists of three layers of silicon pixel sensors situated as close as 4 cm from the beamline, capable of producing 2D hit information of charged particles for use in vertex finding with a spatial resolution of $\sim$ 10-20 μm. The barrel section is accompanied by two end-cap pixel detector disks. Each sensor contains a 52 x 80 grid of individual 100 μm x 150 μm pixels, mounted to a lightweight mechanical substrate along with front-end readout electronics.

A further 10 layers of silicon microstrip detectors are used to accurately reconstruct the track path of charged particles. The sensors collectively cover an area of over 200 m^2, are of p-in-n type, and range from 320 μm to 500 μm in thickness and pixel pitch ranging between 80 μm and 205 μm, depending on distance from the beamline. The track path can be used to determine both the charge and momentum of charged particles, the latter with a $\Delta p_{\mathrm{T}}/p_{\mathrm{T}}$ resolution of $\sim$ 1-2% for a 100 GeV particle.

All silicon detectors situated so close to the interaction point receive high-doses of radiation, eventually ageing due to the damage inflicted. Subsequently, radiation hard sensor and front-end electronics materials and designs have been selected to mitigate the effects of ageing due to radiation damage.

3.2.2 Electromagnetic Calorimeter

The Electromagnetic Calorimeter (ECAL) system provides accurate measurements of energy deposits and the identification of electromagnetically interacting particles, and can also produce spatial measurements when used in conjunction with data from the tracker system. The detector consists of scintillating lead-tungstate ($PbWO_4$) crystals, each of dimension 0.017 x 0.017 ($\Delta\eta \times \Delta\phi$) and 23 cm in length, corresponding to approximately 26 radiation lengths and providing a Molière radius of 2.2 cm. In both the barrel and the end-cap regions, individual crystals are clustered into super-towers, to match with towers in the trigger system (the calorimeter trigger system is described later in section 3.2.5).

Scintillation light produced in each crystal is collected by either avalanche photodiodes in the barrel or vacuum photo-triodes in the endcap. The detectors are required to be both radiation hard and capable of operating within the strong magnetic field environment of CMS.

The ECAL system is measured as having a $\Delta E/E$ resolution for a 100 GeV particle of $\sim 0.5\%$, exceeding it's technical design requirements.

3.2.3 Hadronic Calorimeter

The Hadronic Calorimeter (HCAL) system measures the energy of hadronic showers originating from single-quarks and gluons (i.e. jets). It is constructed from layers of alternating brass absorber and plastic scintillator, of which there are 17 in the barrel and 19 in the endcaps. The latter are spatially divided into towers measuring 0.087 x 0.087 in the barrel and end-caps. Hadronic particle showers deposit energy as scintillation light in the plastic layers, which is transmitted via wavelength shifting fibres to be measured in hybrid photo-diodes. The energy resolution of the HCAL system is calculated with respect to π-meson energy reconstruction, and is measured to be $\sim 90\%/\sqrt{E}$ in the barrel, and $\sim 100\%/\sqrt{E}$ in the endcap.

3.2.4 Muon Systems

The muon system provides identification and precision measurements of muon position and momenta. Energy deposits in the muon systems can be combined with corresponding information from the tracker to improve momentum resolution significantly. The system is designed to have an energy resolution, $\Delta p_{\mathrm{T}}/p_{\mathrm{T}}$ of $\sim 10\%$ on it's own, and $\sim 2\%$ when combined with tracker information, both measured for muons with $p_{\mathrm{T}} < 100$ GeV.

Muons are detected in the outer layers of CMS, with the muon system comprised of three different gaseous detector technologies each with different pseudo-rapidity coverage, shown in figure 3.6. The central barrel region, $|\eta| < 1.2$, is equipped with Drift Tube (DT) detectors - a traditional detector technology, optimised for low - occupancy measurements. Cathode Strip Chambers (CSC) cover the forward region, $0.9 < |\eta| < 2.4$, and dual-layered Resistive Plate Chambers (RPC) cover $|\eta| < 2.1$ - both CSC and RPC detectors being optimised for operation in the presence of both high magnetic field and neutron background environments.

3.2.5 Trigger

Events of interest are selected using a dedicated triggering system [9], split into two distinct stages: the hardware-based Level-1 Trigger (L1) and the software-based High-

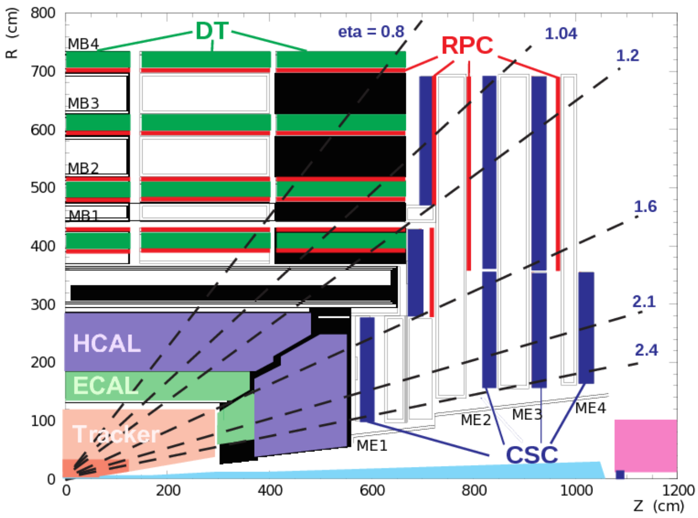

Fig. 3.6 Cross section of the CMS detector in the y-z plane, showing the three muon systems as well as other interior sub-detector systems [8].

Level Trigger (HLT).

Level-1 Hardware Trigger

The L1 system consists of a staged, modular design of custom built hardware electronics subsystems, as shown in figure 3.7. The L1 trigger reconstructs energy deposits in the calorimeter and muon systems into coarse 'trigger-primitive' physics objects. Regional information is gathered by separate modules before being combined in the Global Calorimeter Trigger (GCT) and Global Muon Trigger (GMT) systems, where physics objects are sorted according to energy. Finally, event objects are passed on to the Global Trigger (GT) where a 'Level-1 Accept' (L1A) signal is issued or not, dependent on the event meeting one of up to 128 simple object threshold and multiplicity based requirements.

The L1 system is required to run at 40 MHz, equal to the maximal bunch-crossing rate within CMS, with a L1A decision required within a latency of 3 μs. The maximum available output bandwidth of the L1 system is 100 kHz, but typically is maintained at a lower value to allow for stochastic fluctuations in rate.

High-level Trigger

Following a L1A signal, candidate events are optically transmitted to the HLT system, consisting of a large computer farm of server PCs. Due to the increase in available

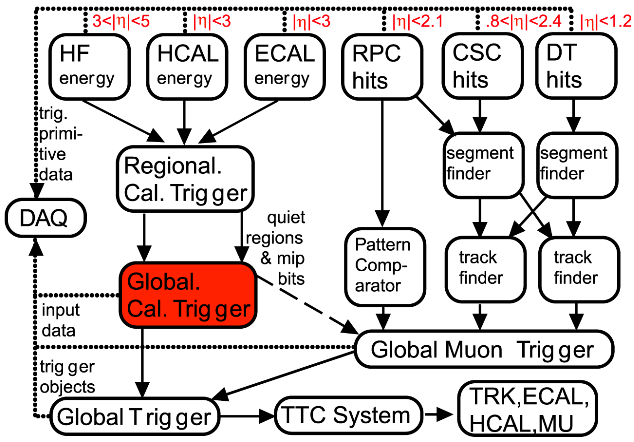

Fig. 3.7 Schematic overview of the Level-1 hardware trigger system of CMS. η coverage is shown in red and the data-flow indicated by arrow direction [9].

processing time of up to 50 ms, events can be reconstructed in greater detail allowing for a closer emulation of offline reconstruction techniques. Complex analyst-designed trigger rules are used, which can employ more sophisticated event-level variables such as α_{T} (described in detail later in chapter 6).

The HLT reduces the event rate further by around two orders of magnitude, producing an output event rate of up to 1 kHz. Events passing the HLT are transmitted to the Grid computing system [57] for full offline reconstruction.

Chapter 4

Object Definitions

Physics objects are observed as energy deposits in the various detector subsystems throughout CMS. Specific definitions for the different objects are provided by the Physics Object Groups (*POGs*), are used in this analysis and described in the following sections.

4.1 Jets

Jets objects occur when a single quark or gluon is produced, subsequently hadronizing and showering throughout the calorimeter systems. Energy deposits in the hadronic calorimeter are clustered using the anti-k_T algorithm [58] with an $R = 0.5$ cone size parameter. Table 4.1 summarises the ID requirements used in this analysis, which correspond to the "Loose" working point [59]. Raw energy measurements that form jets have the following sequential corrections [60, 61] applied:

L1 To remove energy originating from PU events, therefore removing any dependence on luminosity across a dataset [62, 63].

L2 To ensure a uniform energy response in η across the calorimeter [64].

L3 To ensure a uniform response according to the p_{T} of the deposit [64].

L2L3 Final, additional corrections to bring data and MC into agreement.

4.1.1 Identification jets from b quarks

Jets originating from b quarks can be identified using information from the vertex detector due to their increased lifetime with respect to gluons, light flavour quarks

Table 4.1 Criteria for the “loose” jet identification working point.

Requirement	Description
$f_{HPD} < 0.98$	Fractional contribution from the “hottest” Hybrid Photo Diode.
$f_{EM} > 0.01$	Minimum electromagnetic fractional component.
$N^{90}_{\text{hits}} \geq 2$	Number of HCAL channels containing at least 90% of total energy.

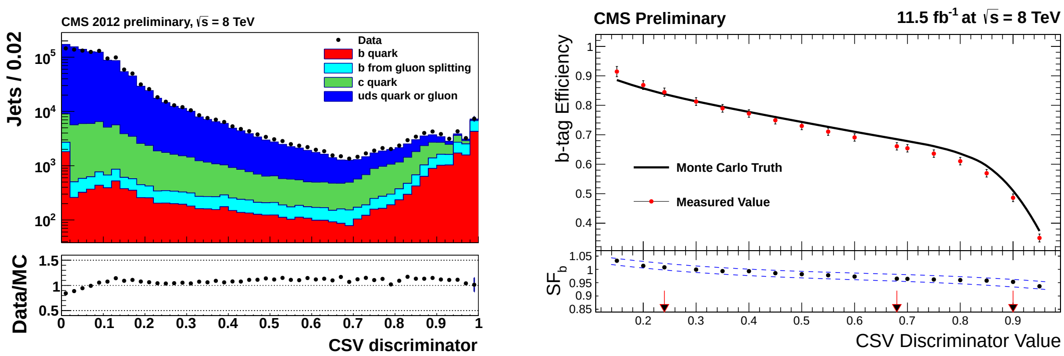

(a) CSV Discriminator (b) CSV Efficiency

Fig. 4.1 The Combined Secondary Vertex b tagging algorithm discriminator distribution (left) and the b tagging efficiency (right) as measured in both data and simulation. MC scale factors are shown in the lower plot of 4.1b [10].

(u, d, s) or charm quarks. B tagging algorithms are designed to determine the probability that a jet originates from a b quark, given, amongst other properties, track displacement from the primary vertex (PV). Each algorithm calculates a value used to discriminate between a jet originating from a b quark or other sources.

The Combined Secondary Vertex (CSV) algorithm [65] is used in this analysis. The distribution of discriminator values is shown in figure 4.1a. The “Medium” working point corresponds to a discriminator threshold of > 0.679, and is used in this analysis. This working point corresponds to a mistag rate for gluons/light-quarks of 1%, and a pT dependent efficiency in the range of 60-70%, as shown in figure 4.1b. Also shown in figure 4.1b are the MC scale factors, SF_b, defined as the ratio of the CSV b tagging algorithm efficiency in data and MC, to be applied to MC samples.

4.2 Muons

Muons are identified from energy deposits predominantly in the muon systems and the tracker using the muon *POG's* Tight working point definition [66], as summarised in table 4.2. This definition is used in both the muon selection in the μ+jets and $\mu\mu$+jets control regions, and the muon veto in the hadronic signal region.

Table 4.2 Muon identification (Tight working point).

Variable	Requirement	Description
Global Muon	True	Muon object is reconstructed from both hits in the muon systems and matched hits in the silicon tracker
PFMuon	True	Muon object reconstructed with multiple subsystems using Particle Flow techniques
$\chi^2/ndof$ of fit	< 10	Goodness of fit of the global muon track fit. Suppresses hadronic punch-through and muons decaying in flight.
Muon chamber hits	> 0	At least 1 hit in a muon chamber. Suppresses hadronic punch-through and muons decaying in flight.
Muon station hits	> 1	Muon hits in at least 2 muon stations. Suppresses punch-through and accidental track-to-segment matches. Also makes consistent with trigger muon requirements.
Transverse impact d_{xy}	< 0.2 mm	Tracker track is close to Primary Vertex in the x-y plane. Helps suppress cosmic ray muons and muons from decays in flight.
Longitudinal distance d_z	< 0.5 mm	Tracker track is close to Primary Vertex in z-direction. Suppresses muons from cosmic rays, decays in flight and PU.
Pixel hits	> 0	At least 1 pixel hit. Suppresses muons from decays in flight.
Track layer hits	> 5	Guarantees good p_{T} measurement.
PF Isolation (PU corrected)	< 0.12	Particle Flow based isolation, based on a cone size of $\Delta R <$ 0.4, with "$\Delta\beta$" PU corrections applied.

4.3 Photons

Photon definitions are made relative to their position in the ECAL, either in the barrel or the endcap, as summarised in table 4.3. This Tight working point ID is defined by the *POG* group [67] and used for both the photon selection in the γ+jets control sample and as a veto in the hadronic signal region.

4.4 Electrons

The Electron *POGs* Loose working point ID [68] is used in this analysis to veto electrons from all areas of the analysis. This cut based identification is defined separately for the barrel and endcap regions of the detector, uses information from the calorimeter systems as well as the tracker, and is summarised in table 4.4. The final two

Table 4.3 Photon identification (Tight working point).

Categories	Barrel	Endcap	Description
Single Tower H/E	< 0.05	< 0.05	Ratio of energy deposited in the HCAL towers within $\Delta R < 0.15$ of the ECAL supercluster, and the ECAL supercluster itself.
$\sigma_{i\eta i\eta}$	< 0.11	< 0.31	The cluster shape covariance of the ECAL supercluster in the η dimension.
PF charged hadron isolation	< 0.70	< 0.50	PF-based isolation requirements to ensure no hadronic or electromagnetic activity with a cone defined by $\Delta R < 0.3$. The isolation is corrected for PU effects.
PF neutral hadron isolation	$< 0.4 + 0.04 \times {p_{\mathrm{T}}}^{\gamma}$	$< 1.5 + 0.04 \times {p_{\mathrm{T}}}^{\gamma}$	
PF photon isolation	$< 0.5 + 0.005 \times {p_{\mathrm{T}}}^{\gamma}$	$< 1.0 + 0.005 \times {p_{\mathrm{T}}}^{\gamma}$	

Table 4.4 Electron identification (Loose working point).

Categories	Barrel	Endcap	Description
$\Delta\eta_{In}$	< 0.007	< 0.009	The difference between the track and ECAL supercluster in the η dimension.
$\Delta\phi_{In}$	< 0.15	< 0.10	The difference between the track and ECAL supercluster in the ϕ dimension.
$\sigma_{i\eta i\eta}$	< 0.01	< 0.03	The cluster shape covariance of the ECAL supercluster in the η dimension.
H/E	< 0.12	< 0.10	Ratio of energy deposited in the HCAL towers within $\Delta R <$ 0.15 of the ECAL supercluster and the ECAL supercluster itself.
d0 (vtx)	< 0.02	< 0.02	The transverse distance of the track from the PV.
dZ (vtx)	< 0.2	< 0.20	The longitudinal distance of the track from the PV.
$\lvert(1/E_{\mathrm{ECAL}} - 1/p_{\mathrm{trk}})\rvert$	< 0.05	< 0.05	Comparison of the ECAL supercluster energy and the track p_{T}, to suppress low p_{T} fakes.
PF relative isolation	< 0.15	$0 < .15$	PF based isolation calculated from particle activity within a cone of $\Delta R < 0.3$.
Vertex fit probability	10^{-6}	10^{-6}	Probability of fit to potential conversion tracks.
Missing hits	≤ 1	≤ 1	Number of missing tracker hits due to possible conversion.

requirements are specifically for the rejection of electrons originating from photons converted into e^-e^+ pairs.

4.5 Energy Sums

Physics objects are combined in the form of kinematic variables known as energy sums. These are calculated on the fly in the analysis using identified objects, with the exception of $\not{E}_T$ which is constructed from PF objects and subject to type-I corrections (jets used for $\not{E}_T$ calculation are subject to prescribed Jet Energy Corrections themselves).

The definitions of the energy sum variables are:

$$\begin{aligned} E_{\mathrm{T}} &= \sum_i |\overrightarrow{p_{\mathrm{T}}}_i|, \\ \not{E}_T &= -\Big|\sum_i \overrightarrow{p_{\mathrm{T}}}_i\Big|, \\ H_T &= \sum_i^{\mathrm{jets}} |\overrightarrow{p_{\mathrm{T}}}_i|, \\ \not{H}_T &= -\Big|\sum_i^{\mathrm{jets}} \overrightarrow{p_{\mathrm{T}}}_i\Big|; \end{aligned} \tag{4.1}$$

namely the total transverse energy, total missing transverse energy, total hadronic energy and total missing hadronic energy. A full set of $\not{E}_T$ filters are defined by the MET *POG* as summarised in table 4.5. The filters account for various physics and detector effects which can give unphysical or spurious $\not{E}_T$ signals.

Table 4.5 $\not{E}_T$ filters employed in the analysis, as recommended by the MET *POG*.

Filter Name	Description
Beam Halo CSC ID	Beam interactions with residual gases in the beam pipe or with mechanical apertures, causing secondary particle production. Events are vetoed if an event contains a positive beam halo ID from the CSC detectors.
HBHE Noise	Noise originating from instrumentation issues with the HCAL's Hybrid Photo Diodes (HPDs) or the Readout Boxes (RBXs). Events are vetoed if they contain isolated clusters of noisy cells in either the barrel or endcap.
Tracking Failure	Significant energy deposits in the calorimeter systems with no corresponding tracks due to tracker algorithm failure. Events are vetoed if the summed p_{T} of all tracks in the event is equal to less than 10% of the H_T.
HCAL Laser Misfire	Calibration lasers being accidentally fired through the HCAL during bunch crossings (as opposed to abort gaps). Events are removed that contain such accidental laser firings.
DeadECAL Cell TP	Dead or damaged ECAL crystals which cannot read out energy deposits correctly. Trigger primitives are checked to determine how much energy was lost, and events are appropriately masked.

4.6 Single Isolated Tracks

Single Isolated Tracks are used to identify hadronically decaying τ leptons and leptonically decaying W bosons where the corresponding lepton has failed identification for whatever reason. Summarised in table 4.6, the selection is based on particle flow candidates - objects which have been constructed from energy deposits in various detector subsystems according to ‘Particle Flow’ algorithms. This ID is used as a veto in all selections, with the selected ‘tag’ lepton ignored in the μ+jets and $\mu\mu$+jets control selections. The ID definition is taken from [69].

Table 4.6 Single Isolated Track identification.

Variable	Requirement	Description
Charge	$\neq 0$	Candidate is charged.
Track p_{T}	> 10 GeV	Track transverse momentum.
$\Delta z(track, PV)$	< 0.05 cm	Longitudinal distance of track from primary vertex.
Relative Track Isolation	< 0.1	Isolation relative to other PF candidate tracks in cone of $\Delta R < 0.3$

Chapter 5

Datasets and MonteCarlo samples

5.1 Datasets

The datasets used in this analysis are listed in Table 5.1. These include the primary signal sample datasets, named ‘HTMHTParked’, and other datasets containing events from triggers used for background estimation.

Table 5.1 8 TeV Datasets with the integrated luminosity for each.

Dataset		Luminosity (fb^{-1})
/HTMHTParked/Run2012B-22Jan2013-v1/AOD		4.41
/HTMHTParked/Run2012C-22Jan2013-v1/AOD		6.80
/HTMHTParked/Run2012D-22Jan2013-v1/AOD		7.29
	Total	18.49
/JetHT/Run2012B-22Jan2013-v1/AOD		4.39
/JetHT/Run2012C-22Jan2013-v1/AOD		6.80
/JetHT/Run2012D-22Jan2013-v1/AOD		7.29
	Total	18.48
/SingleMu/Run2012A-22Jan2013-v1/AOD		0.69
/SingleMu/Run2012B-22Jan2013-v1/AOD		4.40
/SingleMu/Run2012C-22Jan2013-v1/AOD		6.77
/SingleMu/Run2012D-22Jan2013-v1/AOD		7.27
	Total	19.13
/Photon/Run2012A-22Jan2013-v1/AOD		0.68
/SinglePhoton/Run2012B-22Jan2013-v1/AOD		4.40
/SinglePhoton/Run2012C-22Jan2013-v1/AOD		6.77
/SinglePhotonParked/Run2012D-22Jan2013-v1/AOD		7.27
	Total	19.12

5.2 MonteCarlo Background and Signal samples

The full list of MonteCarlo (MC) samples used in this analysis are listed in Table 5.2 along with the number of events, next-to-next-to-leading order (NNLO) cross section and an effective integrated luminosity for each.

The Parton Density Functions (PDF) of colliding protons are modelled according to the CTEQ6L1 distribution, the matrix-element level hard-scatter performed by MadGraph5 or Pythia6, with outgoing partons showered in Pythia6. The produced generator level particles are then put through a full detector simulation in Geant4, and detector hits 'digitized' in order to simulate the response of detector electronics. Prior to digitization, a number of 'MinimumBias' events are overlayed in order to reproduce LHC run conditions. Event-level weights are applied to each simulated sample such that both the PU and equivalent integrated luminosity are matched to a given data sample.

Additional corrections are made to simulated event samples in order to correct the efficiency of b tagging algorithms to match that observed in data. Corrections are determined as a function of jet-flavour (light/c/b), defined as:

$$SF_{light,c,b} = \frac{\epsilon^{data}_{light,c,b}(p_{\mathrm{T}}, \eta)}{\epsilon^{MC}_{light,c,b}(p_{\mathrm{T}}, \eta)}, \tag{5.1}$$

where $\epsilon^{X}_{light,c,b}$ represents p_{T} and η dependent b tagging efficiencies measured in data and MC.

Table 5.2 MC samples for Standard Model processes with their NNLO cross sections and equivalent integrated luminosity.

Sample	N_{event}	Cross section (pb)	Corrected Cross section (pb)	Luminosity (fb^{-1})
/WJetsToLNu_TuneZ2Star_8TeV-madgraph-tarball/Summer12_DR53X-PU_S10_START53_V7A-v1/AODSIM	57661905	37509.0	34133.2	1.5
/WJetsToLNu_HT-150To200_8TeV-madgraph/Summer12_DR53X-PU_S10_START53_V7C-v1/AODSIM	21414209	253.8	234.53	84.4
/WJetsToLNu_HT-200To250_8TeV-madgraph/Summer12_DR53X-PU_S10_START53_V7C-v1/AODSIM	9895771	116.5	103.94	84.9
/WJetsToLNu_HT-250To300_8TeV-madgraph_v2/Summer12_DR53X-PU_S10_START53_V7A-v1/AODSIM	4924990	57.6	51.34	85.5
/WJetsToLNu_HT-300To400_8TeV-madgraph_v2/Summer12_DR53X-PU_S10_START53_V7A-v1/AODSIM	5141023	48.4	42.41	106.2
/WJetsToLNu_HT-400ToInf_8TeV-madgraph_v2/Summer12_DR53X-PU_S10_START53_V7A-v1/AODSIM	4923847	30.8	26.36	159.9
/ZJetsToNuNu_50_HT_100_TuneZ2Star_8TeV_madgraph(_ext)/Summer12_DR53X-PU_S10_START53_V7A-v1/AODSIM	23743998	452.8	405.21	52.4
/ZJetsToNuNu_100_HT_200_TuneZ2Star_8TeV_madgraph(_ext)/Summer12_DR53X-PU_S10_START53_V7A-v1/AODSIM	9876059	190.4	173.76	51.9
/ZJetsToNuNu_200_HT_400_TuneZ2Star_8TeV_madgraph(_ext)/Summer12_DR53X-PU_S10_START53_V7A-v1/AODSIM	9649619	45.1	42.41	214.0
/ZJetsToNuNu_400_HT_inf_TuneZ2Star_8TeV_madgraph(_ext)/Summer12_DR53X-PU_S10_START53_V7A-v1/AODSIM	5079710	6.26	5.81	811.5
/TT_CT10_TuneZ2star_8TeV-powheg-tauola/Summer12_DR53X-PU_S10_START53_V7A-v1(v2)/AODSIM	27094723	234.0	271.44	115.8
/TTZJets_8TeV-madgraph_v2/Summer12_DR53X-PU_S10_START53_V7A-v1/AODSIM	210160	0.172	0.172	1221.9
/T_t-channel_TuneZ2star_8TeV-powheg-tauola/Summer12_DR53X-PU_S10_START53_V7A-v1/AODSIM	3710227	56.4	56.4	65.8
/Tbar_t-channel_TuneZ2star_8TeV-powheg-tauola/Summer12_DR53X-PU_S10_START53_V7A-v1/AODSIM	1935072	30.7	30.7	63.0
/T_s-channel_TuneZ2star_8TeV-powheg-tauola/Summer12_DR53X-PU_S10_START53_V7A-v1/AODSIM	243961	3.79	3.79	64.4
/Tbar_s-channel_TuneZ2star_8TeV-powheg-tauola/Summer12_DR53X-PU_S10_START53_V7A-v1/AODSIM	139974	1.76	1.76	79.5
/T_tW-channel-DR_TuneZ2star_8TeV-powheg-tauola/Summer12_DR53X-PU_S10_START53_V7A-v1/AODSIM	497658	11.1	11.1	44.8
/Tbar_tW-channel-DR_TuneZ2star_8TeV-powheg-tauola/Summer12_DR53X-PU_S10_START53_V7A-v1/AODSIM	493460	11.1	11.1	44.5
/DYJetsToLL_M-10To50filter_8TeV-madgraph/Summer12_DR53X-PU_S10_START53_V7A-v1/AODSIM	7116223	13124.1	12205.4	0.5
/DYJetsToLL_M-50_TuneZ2Star_8TeV-madgraph-tarball/Summer12_DR53X-PU_S10_START53_V7A-v1/AODSIM	30171503	3503.7	3258.45	8.6
/DYJetsToLL_HT-200To400_TuneZ2Star_8TeV-madgraph(_ext)/Summer12_DR53X-PU_S10_START53_V7A-v1/AODSIM	6892777	24.3	22.24	283.7
/DYJetsToLL_HT-400ToInf_TuneZ2Star_8TeV-madgraph/Summer12_DR53X-PU_S10_START53_V7A-v1/AODSIM	2695789	3.36	3.11	802.3
/GJets_HT-200To400_8TeV-madgraph/Summer12_DR53X-PU_S10_START53_V7A-v1/AODSIM	57891147	1140.8	1060.9	50.7
/GJets_HT-400ToInf_8TeV-madgraph/Summer12_DR53X-PU_S10_START53_V7A-v1/AODSIM	9459562	124.7	115.97	75.9
/WW_TuneZ2star_8TeV_pythia6_tauola/Summer12_DR53X-PU_S10_START53_V7A-v1/AODSIM	9888431	57.1	57.1	173.2
/WZ_TuneZ2star_8TeV_pythia6_tauola/Summer12_DR53X-PU_S10_START53_V7A-v1/AODSIM	9841248	12.6	12.6	781.1
/ZZ_TuneZ2star_8TeV_pythia6_tauola/Summer12_DR53X-PU_S10_START53_V7A-v1/AODSIM	9751908	8.26	8.26	1180.6
/QCD_Pt-50to80_TuneZ2star_8TeV_pythia6/Summer12_DR53X-PU_S10_START53_V7A-v2	5950860	8148778 (LO)	8148778 (LO)	0.001
/QCD_Pt-80to120_TuneZ2star_8TeV_pythia6/Summer12_DR53X-PU_S10_START53_V7A-v3	5962864	1033680 (LO)	1033680 (LO)	0.006
/QCD_Pt-120to170_TuneZ2star_8TeV_pythia6/Summer12_DR53X-PU_S10_START53_V7A-v3	5985732	156293 (LO)	156293 (LO)	0.038
/QCD_Pt-170to300_TuneZ2star_8TeV_pythia6/Summer12_DR53X-PU_S10_START53_V7A-v1(v2)	20155180	34138 (LO)	34138 (LO)	0.590
/QCD_Pt-300to470_TuneZ2star_8TeV_pythia6/Summer12_DR53X-PU_S10_START53_V7A-v1(v2,v3)	23588100	1759.5 (LO)	1759.5 (LO)	13.4
/QCD_Pt-470to600_TuneZ2star_8TeV_pythia6/Summer12_DR53X-PU_S10_START53_V7A-v2	3978848	113.9 (LO)	113.9 (LO)	34.9
/QCD_Pt-600to800_TuneZ2star_8TeV_pythia6/Summer12_DR53X-PU_S10_START53_V7A-v2	3964864	27.0 (LO)	27.0 (LO)	146.8
/QCD_Pt-800to1000_TuneZ2star_8TeV_pythia6/Summer12_DR53X-PU_S10_START53_V7A-v2	3854563	3.55 (LO)	3.55 (LO)	1085.8
/QCD_Pt-1000to1400_TuneZ2star_8TeV_pythia6/Summer12_DR53X-PU_S10_START53_V7A-v1	1964088	0.738 (LO)	0.738 (LO)	2661.4
/QCD_Pt-1400to1800_TuneZ2star_8TeV_pythia6/Summer12_DR53X-PU_S10_START53_V7A-v1	1988062	0.0335 (LO)	0.0335 (LO)	59345.1
/QCD_Pt-1800_TuneZ2star_8TeV_pythia6/Summer12_DR53X-PU_S10_START53_V7A-v1	977586	0.00183 (LO)	0.00183 (LO)	534200
/QCD_HT-100To250_TuneZ2star_8TeV-madgraph-pythia/Summer12_DR53X-PU_S10_START53_V7A-v1/AODSIM	50081518	1.036E7 (LO)	1.036E7 (LO)	0.005
/QCD_HT-250To500_TuneZ2star_8TeV-madgraph-pythia6/Summer12_DR53X-PU_S10_START53_V7A-v1/AODSIM	27062078	276000 (LO)	276000 (LO)	0.1
/QCD_HT-500To1000_TuneZ2star_8TeV-madgraph-pythia6/Summer12_DR53X-PU_S10_START53_V7A-v1/AODSIM	27613225	8426 (LO)	8426 (LO)	3.3
/QCD_HT-1000ToInf_TuneZ2star_8TeV-madgraph-pythia6/Summer12_DR53X-PU_S10_START53_V7A-v1/AODSIM	12018415	204 (LO)	204 (LO)	58.9

Interpretations are made using signal MC samples, each representing a scan in the phase space of a specific SMS model. The samples used are listed in Table 5.3. Each sample is generated at the parton level using MadGraph5 and then decayed using Pythia6. Diagrams for up to two additional partons are simulated in the initial generation step to ensure good modelling of initial state radiation (ISR), however supplementary samples were produced with up to three additional partons to allow for systematic studies into the effect on analysis acceptance, as detailed in chapter 9.

Signal MC samples use the FastSim detector simulation framework [70] in order to simulate detector and electronics responses. In comparison to the FullSim method used for all other MC backgrounds, FastSim aims to greatly reduce the processing time required to generate samples by avoiding the CPU-intensive full detector simulation using the Geant framework, instead employing detector response parametrisations tuned using FullSim samples.

Table 5.3 MC samples for Simplified Model Spectra.

Model	Sample	Description
Charm decay	/SMS-MadGraph_2J_T2cc_NoFilter_mStop-100to250_mLSP-20to230_8TeV-Pythia6Zstar/Summer12-START52_V9_FSIM-v1/AODSIM	Original scan
Charm decay	/SMS-T2cc_NoFilter_mStop-175to250_mLSP-95to240_8TeV-Pythia6Z/Summer12-START52_V9_FSIM-v1/AODSIM	Original scan
Charm decay	/SMS-T2cc_2J_mStop-250to350_mLSP-195to340_TuneZ2star_8TeV-madgraph-tauola/Summer12-START53_V19_FSIM-v2/AODSIM	Scan extension
Charm decay	/SMS-8TeV_Pythia6Z_T2cc_3jets_mStop-200_mLSP-120/Summer12-START52_V9_FSIM-v1/AODSIM	3-parton sample
Charm decay	/SMS-8TeV_Pythia6Z_T2cc_3jets_mStop-200_mLSP-190/Summer12-START52_V9_FSIM-v1/AODSIM	3-parton sample
Four-body decay	/SMS-T2DegenerateStop_2J_mStop-100to150_mLSP-20to140_TuneZ2star_8TeV-madgraph-tauolapp/Summer12-START53_V19_FSIM_PU_S12-v1/AODSIM	Original scan
Four-body decay	/SMS-T2DegenerateStop_2J_mStop-175to225_mLSP-95to215_TuneZ2star_8TeV-madgraph-tauolapp/Summer12-START53_V19_FSIM_PU_S12-v1/AODSIM	Original scan
Four-body decay	/SMS-T2DegenerateStop_2J_mStop-250to300_mLSP-170to290_TuneZ2star_8TeV-madgraph-tauolapp/Summer12-START53_V19_FSIM_PU_S12-v1/AODSIM	Original scan
Four-body decay	/SMS-T2DegenerateStop_2J_mStop-325to375_mLSP-245to365_TuneZ2star_8TeV-madgraph-tauolapp/Summer12-START53_V19_FSIM_PU_S12-v1/AODSIM	Original scan
Four-body decay	/SMS-T2DegenerateStop_2J_mStop-400_mLSP-320to390_TuneZ2star_8TeV-madgraph-tauolapp/Summer12-START53_V19_FSIM_PU_S12-v1/AODSIM	Original scan

5.3 Correcting SM sample cross sections

5.3.1 H_T^{parton} binned samples

In order to increase statistics this analysis makes use of MC samples binned according to parton-level H_T (H_T^{parton}). Leading order (LO) cross-sections are provided with these samples, which are translated into next-to-next-to-leading order (NNLO) cross-sections using translation-factors (k-factors) derived from corresponding inclusive sample cross-sections. However, recent CMS studies [71] have shown that the provided LO cross-sections for H_T^{parton} binned samples can be incorrect by up to 10%. This is shown in figure 5.1a, where unphysical steps are present in the ratio between the $\mathrm{Z}(\nu\nu) + \mathrm{jets}$ binned sample and the $\mathrm{DY} + \mathrm{jets}$ inclusive sample.

Two of the binned samples have corresponding inclusive samples to allow for a comparison to be made, namely $\mathrm{W} + \mathrm{jets}$ and $\mathrm{DY} + \mathrm{jets}$. For these two cases, the derivation of corrections for each H_T^{parton} binned sample is trivial. However, for $\mathrm{Z}(\nu\nu) +$ jets no such inclusive sample exists. This sample is compared with the inclusive $\mathrm{DY} + \mathrm{jets}$ sample, where the overall normalisation is set as the relative cross section of $Z \to \nu\bar{\nu}$ to $Z \to \ell\ell$, 0.505. An example ratio plot is shown in figure 5.1b, where a constant ratio between the samples is found following the application of corrections to the individual sample cross sections.

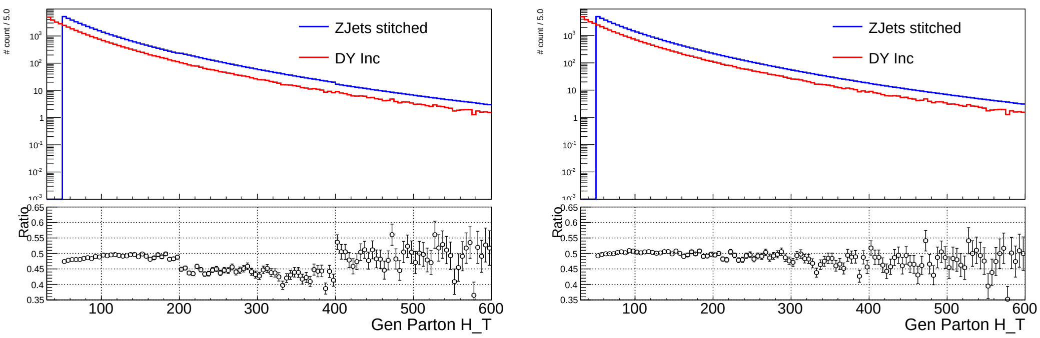

(a) No corrections. (b) With corrections.

Fig. 5.1 Generator level H_T^{parton} distributions from the inclusive DY + jets and the H_T^{parton} binned $\mathrm{Z}(\nu\nu) + \mathrm{jets}$ samples., both before and after cross section corrections.

5.3.2 H_T sideband normalisation

As mentioned in section 5.3, absolute MC normalisation is not well modelled in the high-$\not\!\!E_T$ region of phase-space in which many SUSY analyses search. As such, data and MC are seen to disagree using standard MC samples and cross-sections. While data and MC comparisons are not explicitly used in this analysis, ratios of MC yields are, and so cross-section correction factors for the main MC processes must be derived. Corrections are taken as the data to MC ratio in the $150 \leq H_T < 200$ GeV sideband region, in a given control sample with a targeted selection, designed to yield a pure sample of a background process. A summary of the selections, their relevant purities and the derived corrections are given in table 5.4.

Table 5.4 The process-specific sideband corrections applied to MC sample, with the selection used and it's corresponding purity.

Process	Selection	Purity	Correction factor
W + jets	μ+jets, $2 \leq n_{\text{jet}} \leq 3$, $n_{\text{b}} = 0$	0.91	0.93 ± 0.01
Z($\rightarrow \mu\mu$) + jets	$\mu\mu$+jets, $2 \leq n_{\text{jet}} \leq 3$, $n_{\text{b}} = 0$	0.98	0.94 ± 0.04
$\text{t}\bar{\text{t}}$	μ+jets, $n_{\text{jet}} \geq 2$, $n_{\text{b}} \geq 2$	0.87	1.21 ± 0.05

These derived correction factors are tested in the closure tests performed following their application (discussed in section 7.3.1).

5.4 Predicting high-n_{b} event yields

Determining yields for high-n_{b} analysis categories directly from simulation becomes inherently reliant on not only MC modelling, but also on the physics distribution of jet-flavours. For EWK samples, given the underlying abundance of low b-jet multiplicity events, high-n_{b} categories become dominated by mistagging of light-flavour jets, leading to large statistical uncertainties. In order to reduce this reliance on MC yields, a method has been developed using flavour tagging efficiencies and the underlying quark flavour distribution, both measured directly from simulation. This method therefore has the goal of providing more statistically precise yields, particularly for the high-n_{b} categories.

The method and its validation are described in detail in [72]. The approach can be summarised by:

$$
\begin{aligned}
N(n) = \sum_{n_b^{gen}+n_c^{gen}+n_{\text{light}}^{gen}=n_{jet}^{cat}} \ \sum_{n_b^{tag}+n_c^{tag}+n_{\text{light}}^{tag}=n} N(n_b^{gen}, n_c^{gen}, n_q^{gen}) \times \\
P(n_b^{tag}, n_b^{gen}, \epsilon_b) \times P(n_c^{tag}, n_c^{gen}, \epsilon_c) \times P(n_{\text{light}}^{tag}, n_{\text{light}}^{gen}, \epsilon_{\text{light}}),
\end{aligned} \tag{5.2}
$$

where $N(n)$ represents the predicted yield of n b-tagged events for a given analysis category and H_T bin. The jet-flavour tagging probability terms $P(n_b^{tag}, n_b^{gen}, \epsilon_b)$, $P(n_c^{tag}, n_c^{gen}, \epsilon_c)$ and $P(n_{\text{light}}^{tag}, n_{\text{light}}^{gen}, \epsilon_{\text{light}})$ are measured for each H_T bin and analysis category for each simulated sample, including the flavour tagging efficiencies ϵ_b, ϵ_c and ϵ_{light} as also measured from each sample. Finally, $N(n_b^{gen}, n_c^{gen}, n_q^{gen})$ represents the distribution of actual generator-level jet flavours in the events.

In the large-statistic sample limit this technique would not be necessary, as enough high-n_{b} events would be present to sufficiently reduce statistical uncertainties. However, in the absence of this infeasible scenario, this technique makes uses of all events in a sample, thereby reducing uncertainties and ultimately delivering more precise yields from simulation.

Chapter 6

The α_{T} Analysis

6.1 Analysis Overview

Analyses searching in the jets and $\not\!\!E_T$ final state encounter significant backgrounds from SM sources of both genuine and fake $\not\!\!E_T$. Genuine $\not\!\!E_T$ originates from $\mathrm{t\bar{t}}$, W and Z boson production, with one or more neutrinos in the final state. In this analysis background predictions are made for these processes using extrapolations into the signal region from independent, process-specific control samples, as described in chapter 7. Fake $\not\!\!E_T$ predominantly originates from mismeasurements of QCD multijet (MJ) production, which is the dominant process in the hadronic environment and phase space considered in this analysis due to it's very large cross section. Small inconsistencies in the handling of such large backgrounds or rare detector effects can therefore have a significant impact on an analysis. This background is reduced to an entirely negligible level using the dimensionless kinematic variable, α_{T}.

In this analysis events are binned in exclusive categories of H_T, and the multiplicity of jets and b-tagged jets, n_{jet} and n_{b}, as summarised in table 6.1. Such binning allows for targeted interpretations across the vast array of possible simplified model final states, while reducing background yields to a minimum.

The main analysis search region is described in the remainder of this chapter.

6.1.1 The α_{T} kinematic variable

Attempting to accurately measure the QCD contribution to the total background is particularly challenging given the hadronic environment of the LHC and the lack of precise measurements and calculations of the large multijet cross sections involved. As an alternative approach, the goal of this analysis is to reduce QCD down to an en-

Table 6.1 H_T bin lower bounds used for each n_{jet} and n_{b} category.

(n_{jet},n_{b})	H_T bins (GeV)									
(2-3,0)	200	275	325	375	475	575	675	775	875	975	>1075
(2-3,1)	200	275	325	375	475	575	675	775	875	975	>1075
(2-3,2)	200	275	325	375	475	575	675	775	>875		
(≥4,0)	200	275	325	375	475	575	675	775	875	975	>1075
(≥4,1)	200	275	325	375	475	575	675	775	875	975	>1075
(≥4,2)	200	275	325	375	475	575	675	775	>875		
(≥4,3)	200	275	325	375	475	575	675	775	>875		
(≥4,≥4)	200	275	325	>375							

tirely negligible levels with respect to background processes with genuine $\not\!\!E_T$, achieved through the use of the dimensionless kinematic variable, α_{T}. The di-jet variable α was first proposed by Randall et al. in 2008 [73], and later translated into the transverse plane for use with LHC analyses [74, 75]. α_{T} is defined for di-jets as:

$$\alpha_{\mathrm{T}} = \frac{\sqrt{E_T^{j_2}/E_T^{j_1}}}{\sqrt{2(1 - cos(\Delta\phi))}}, \tag{6.1}$$

where $E_T^{j_1}$ and $E_T^{j_2}$ are the reconstructed transverse energies of the first and second jets respectively, and $\Delta\phi$ is the separation between the two jets in the ϕ plane.

A perfectly measured di-jet event containing back to back jets in ϕ of equal energy will have an α_{T} value of 0.5, whereas events with $\not\!\!E_T$ originating from jet energy mismeasurements will have values of $\alpha_{\mathrm{T}} < 0.5$. Only events containing sources of genuine $\not\!\!E_T$, whether from SM or BSM sources, can have values of $\alpha_{\mathrm{T}} > 0.5$.

The α_{T} variable can be generalised to an n-jet case by considering the event as a pseudo-di-jet system, constructing each pseudo-jet such that the difference in H_T between each pseudo-jet system, ΔH_T, is minimised. α_{T} then takes the form:

$$\alpha_{\mathrm{T}} = \frac{1}{2} \times \frac{H_T - \Delta H_T}{\sqrt{H_T^2 - \not\!\!H_T^2}} = \frac{1}{2} \times \frac{1 - \frac{\Delta H_T}{H_T}}{\sqrt{1 - \left(\frac{\not\!\!H_T}{H_T}\right)^2}}. \tag{6.2}$$

The α_{T} variable introduces a correlation between the two variables of $\not\!\!H_T$ and ΔH_T. This relationship is demonstrated in figure 6.1 by the black contours of constant α_{T}. Different physics processes will populate various regions of this plane, as also shown in the MC study in figure 6.1. Most notably QCD exhibits a strong correlation

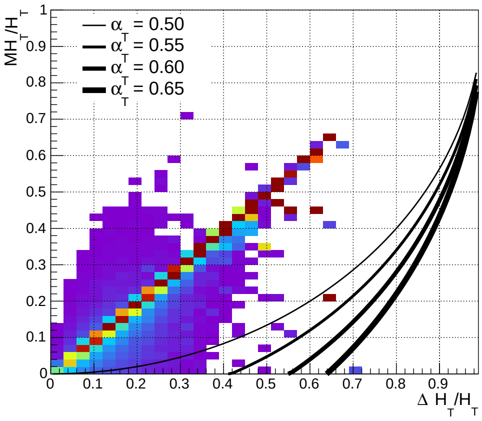

(a) QCD

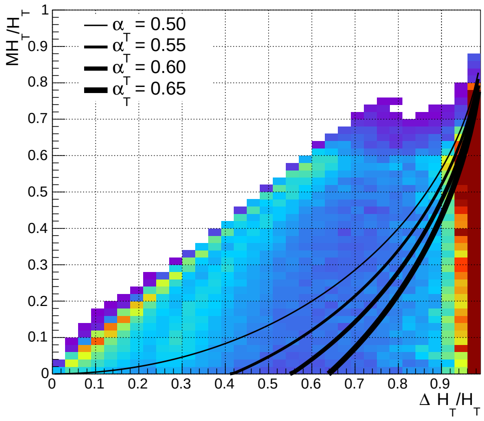

(b) $Z \to \nu\bar{\nu}$

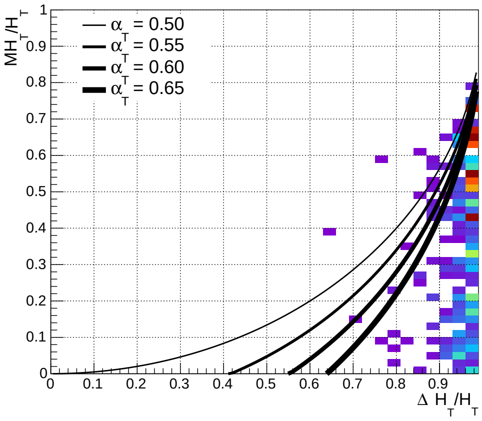

(c) Charm decay model (250, 240)

Fig. 6.1 The correlation between $\not{H}_T$ and ΔH_T for MC samples of QCD, $Z \to \nu\bar{\nu}$ and an example mass point of the charm decay signal model ($m_{\tilde{t}} = 250$ GeV, $m_{\tilde{\chi}^0} = 240$ GeV). Contours of constant α_{T} are shown in black. Each axis is normalised according to the events H_T.

between the two variables at low values of α_{T} (figure 6.1a), while processes with real $\not{E}_T$ break this correlation, sitting also at higher values of α_{T} (figures 6.1b and 6.1c).

Through the requirement of α_{T} in a given region of H_T, a certain missing energy threshold is implied. Figure 6.2 demonstrates this, relationship for the assumption of $\Delta H_T = 0$ - an assumption which yields the minimum $\not{H}_T$ values. Given this correlation, the implicit missing energy threshold can be maintained across the H_T range by lowering the α_{T} thresholds in the high H_T region.

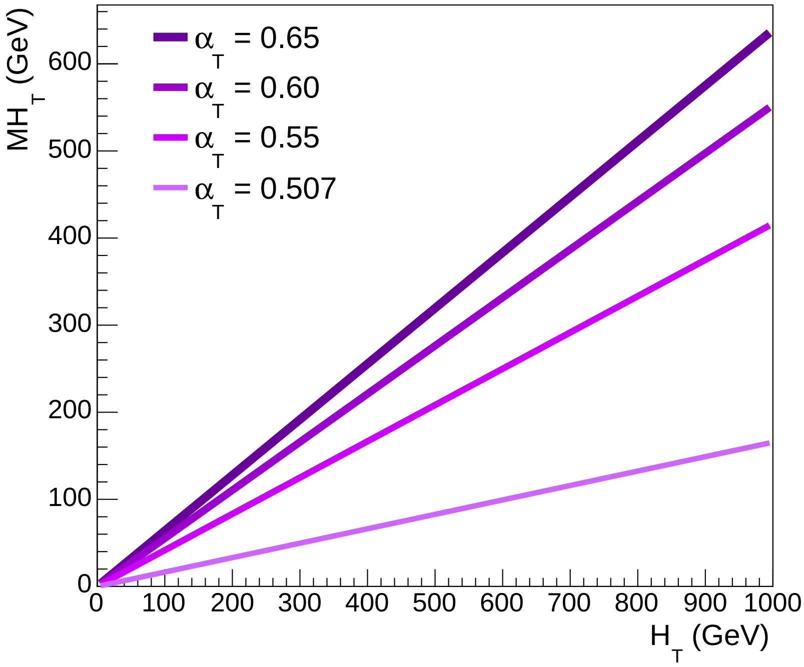

Fig. 6.2 The correlation between H_T and $\not{H}_T$ for different α_{T} values, with the assumption of $\Delta H_T = 0$.

6.2 Standard Model Backgrounds

6.2.1 Genuine $\not{E}_T$

The dominant Electroweak (EWK) source of genuine missing energy comes from Z-boson production where the Z decays to neutrinos, $Z \to \nu\bar{\nu}$, with associated jets. This source of background is considered irreducible.

Events containing leptonic decays of W bosons, $W \to \ell\nu$, originating either from direct W production, or via the decay of a top quark from $\mathrm{t\bar{t}}$ production, are sources of genuine missing energy due to the presence of a weakly interacting neutrino which evades detection. Such events are vetoed in the signal region due to the presence of a lepton. However, if the lepton is not detected, leptonic W decays can pass the signal selection, forming a significant SM background.

Leptons can be 'lost' for a variety different reasons, but ultimately for failing the lepton ID criteria. There are numerous potential causes, the most prevalent being soft-leptons below the ID's p_{T} threshold or non-isolated leptons which pass the ID quality cuts but fail the isolation requirement.

Following the hadronic selection requirements (outlined in section 6.4), any remaining contributions from SM EWK backgrounds are estimated using a fully data-driven transfer factor technique, described in detail in Section 7.1.

6.2.2 Fake $\not\!\!E_T$

As mentioned previously, the dominant source of background for analyses searching for a multijet final state is from QCD. A fully-measured QCD event would consist of multiple jets balancing each other in all planes. However, in order to enter the signal region an event must contain missing energy, $\not\!\!H_T$ (equivalent to $\not\!\!E_T$ in all-hadronic events).

The most common way for a balanced multijet (MJ) event to gain $\not\!\!H_T$ occurs if one or more of the jets are mismeasured, such that their vectorial sum then leads to non-zero $\not\!\!H_T$. This can occur due to detector issues, or due to stochastic fluctuations within the inherant jet-resolution of the detector. The former is protected against by the $\not\!\!E_T$ filters summarised in table 4.5 and using a further filter to remove events affected by non-functioning or damaged regions of the ECAL system, where events are vetoed if they contain significant energy deposits within a given distance from a known problematic region. The latter is dealt with using a cut on the α_{T} variable where events with fake missing energy signatures give values < 0.5.

QCD MJ events can also appear to contain non-zero missing energy due to the threshold requirements of jets. If an event contains one or more jets below the analysis threshold, then the event is measured as imbalanced and containing $\not\!\!H_T$. Events such as these are largely removed with the α_{T} requirement, however in addition a requirement is made on the ratio $\not\!\!H_T/\not\!\!E_T$.

Details of residual QCD cleaning cuts are given later in section 7.4.

6.3 Signal Triggers

Events are collected at the HLT using a dedicated suite of signal triggers. For an event to pass the trigger requirements, it must exceed both a H_T and an α_{T} threshold. Trigger rate can be maintained by varying the threshold on each of these independent requirements, as shown in Table 6.2. Each H_T bin in the analysis is seeded by a specific signal trigger, with a 25 GeV offset between online and offline H_T, with the exception of the 200 GeV bin.

Exclusively for this analysis, the additional 'Parked' trigger `HT200_AlphaT0p57` is included, seeding the new $H_T > 200$ GeV bin. Such a low threshold allows sensitivity to be maintained for softer physics signatures, such as those expected from compressed spectra SUSY decays studied in this work.

Table 6.2 Signal triggers, the L1 seed triggers and their efficiencies measured for per H_T and n_{jet} category.

Offline H_T region (GeV)	Offline α_{T} threshold	L1 seed (`L1_?`) (highest thresholds)	Trigger (`HLT_?`)	Efficiency (%) $2 \leq n_{\mathrm{jet}} \leq 3$	$n_{\mathrm{jet}} \geq 4$
$200 < H_T < 275$	0.65	`DoubleJetC64`	`HT200_AlphaT0p57`	$81.8^{+0.4}_{-0.4}$	$78.9^{+0.3}_{-0.4}$
$275 < H_T < 325$	0.60	`DoubleJetC64`	`HT200_AlphaT0p57`	$95.2^{+0.3}_{-0.4}$	$90.0^{+1.2}_{-1.3}$
$325 < H_T < 375$	0.55	`DoubleJetC64 OR HTT175`	`HT300_AlphaT0p53`	$97.9^{+0.3}_{-0.3}$	$95.6^{+0.9}_{-1.0}$
$375 < H_T < 475$	0.55	`DoubleJetC64 OR HTT175`	`HT350_AlphaT0p52`	$99.2^{+0.2}_{-0.2}$	$98.7^{+0.5}_{-0.7}$
$H_T > 475$	0.55	`DoubleJetC64 OR HTT175`	`HT400_AlphaT0p51`	$99.8^{+0.1}_{-0.3}$	$99.6^{+0.3}_{-0.7}$

Trigger efficiencies are measured using an unbiased single-muon reference trigger, `HLT_IsoMu24_eta2p1`, via a muon tag and probe method where a single-muon is selected and then subsequently ignored from the analysis when calculating event level variables such as H_T, $\not{H}_T$ and α_{T}. Efficiencies are measured for each H_T bin and for each n_{jet} category, as summarised in table 6.2. Example trigger 'turn-on' curves are shown for the 3 lowest H_T bins in figures 6.3 and 6.4. The curves are shown both differentially and cumulatively, to show the efficiency for events of a given α_{T} value and above an α_{T} threshold respectively. Across the higher H_T bins the triggers are measured as fully efficient. Inefficiencies in the low H_T bins are understood as being due to the relatively high threshold L1 seed trigger used for this region, in order to maintain low rates in the high PU environment encountered throughout Run I. Lower efficiencies are also observed in the $n_{\mathrm{jet}} \geq 4$ category attributed to the presence of softer jets, as an increased number of jets must equate to the same total H_T requirement of a given bin.

All triggers were present throughout Run I, however the `HLT_HT200_AlphaT0p57` trigger was used as part of the 'Parked' data stream which was reconstructed at a later date, following the active data-taking period. During data-taking triggers may have 'prescale' factors applied to them such that only every n triggered events are actually recorded, however all of the signal triggers remained without a prescale for the entirety of the 8 TeV data-taking.

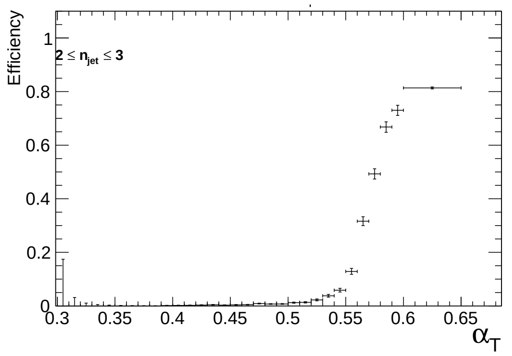

(a) Differential, $200 < H_T < 275$ GeV

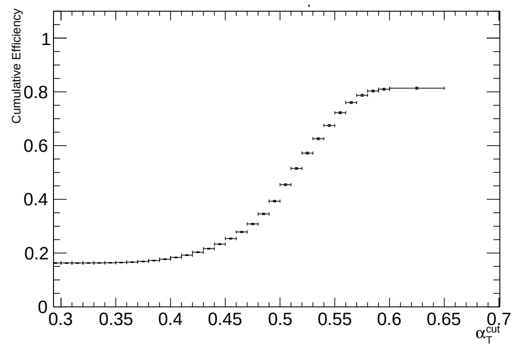

(b) Cumulative, $200 < H_T < 275$ GeV

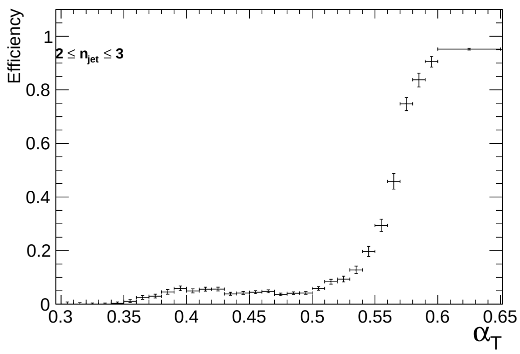

(c) Differential, $275 < H_T < 325$ GeV

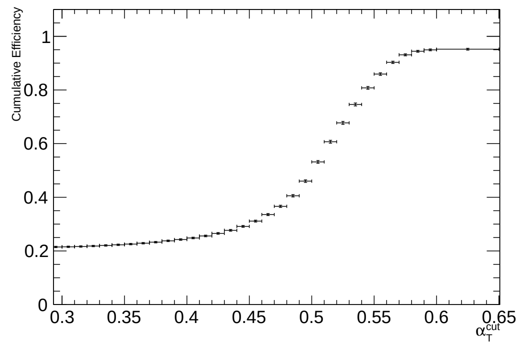

(d) Cumulative, $275 < H_T < 325$ GeV

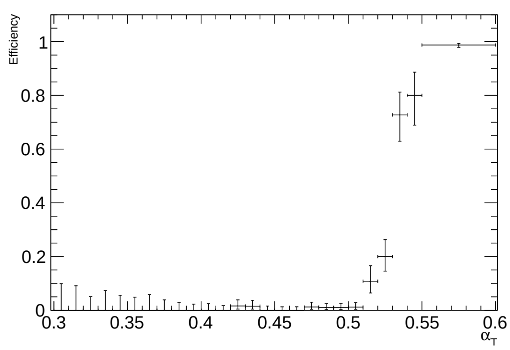

(e) Differential, $325 < H_T < 375$ GeV

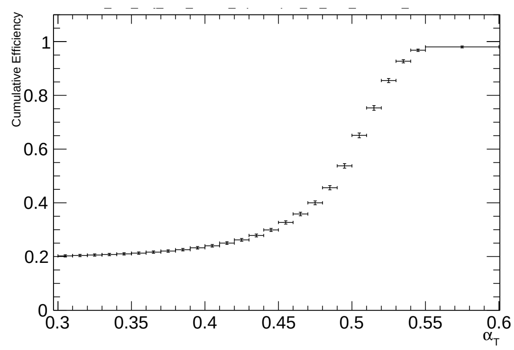

(f) Cumulative, $325 < H_T < 375$ GeV

Fig. 6.3 Differential (left) and cumulative (right) efficiency turn-on curves for the signal triggers, for the three lowest H_T bins and $2 \leq n_{\text{jet}} \leq 3$.

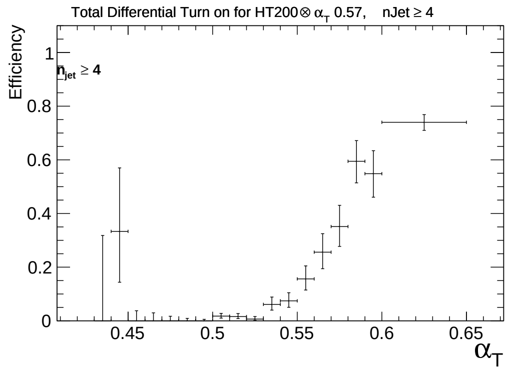

(a) Differential, $200 < H_T < 275$ GeV

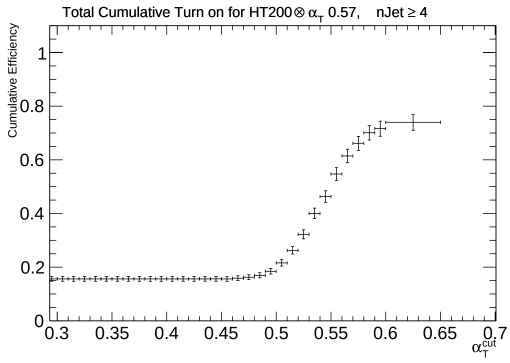

(b) Cumulative, $200 < H_T < 275$ GeV

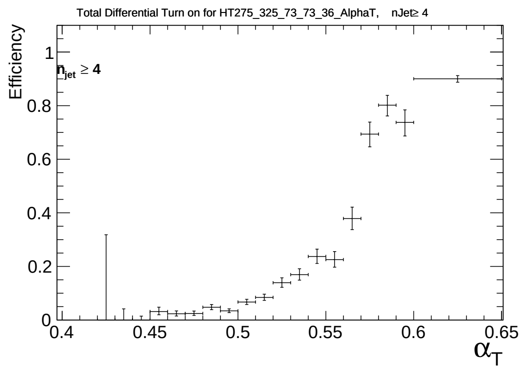

(c) Differential, $275 < H_T < 325$ GeV

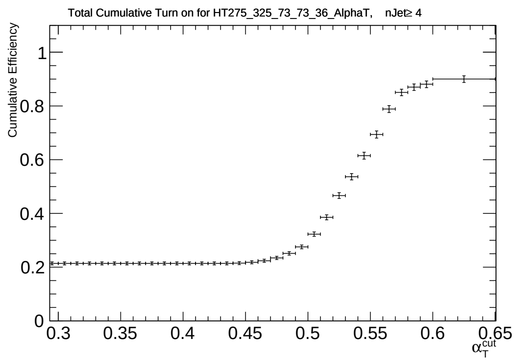

(d) Cumulative, $275 < H_T < 325$ GeV

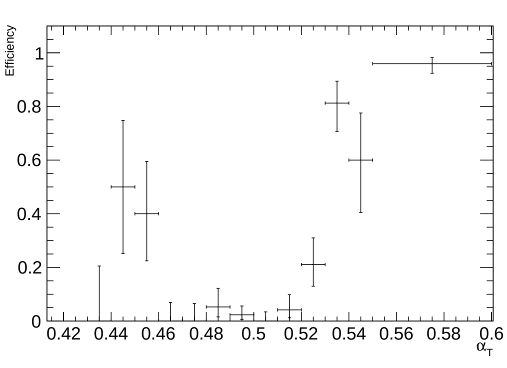

(e) Differential, $325 < H_T < 375$ GeV

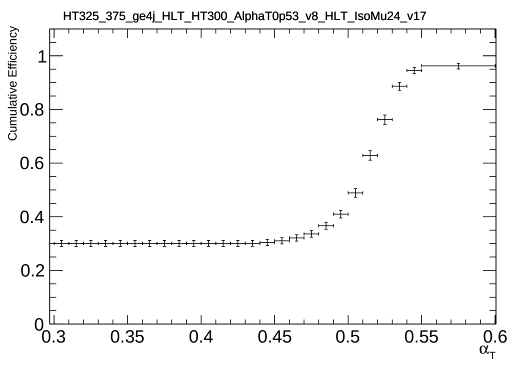

(f) Cumulative, $325 < H_T < 375$ GeV

Fig. 6.4 Differential (left) and cumulative (right) efficiency turn-on curves for the signal triggers, for the three lowest H_T bins and $n_{\mathrm{jet}} \geq 4$.

6.4 Selection Criteria

Event selection requirements for the hadronic signal region are chosen with an aim to maintain sensitivity to hadronically decaying sparticle production, while rejecting as many QCD-type processes as possible. To do so, requirements are made on:

Jets Events are required to contain at least two jets, and have $H_T > 200$ GeV, to ensure the presence of significant hadronic activity. They are categorised by H_T, with jet p_{T} requirements on the two leading and the remaining additional jets separately. The jet p_{T} thresholds vary as a function of the H_T bin of the event, as shown in Table 6.3, in order to maintain a similar kinematic phase space throughout the H_T range.

Leptons Any events containing leptons are vetoed to ensure only hadronic events are considered, thereby suppressing events with genuine $\not{E}_T$ from leptonic decays to neutrinos such as $W \to \ell\nu$.

Photons Events containing photons are vetoed, for similar reasons as the leptonic vetoes, in order to maintain a purely hadronic environment.

Single Isolated Tracks Events containing a Single Isolated Track (SIT) are vetoed from the signal region. This tracker based veto is particularly useful for vetoing additional events that contain leptons which have failed our lepton ID requirements entirely and are therefore not considered by the leptonic vetoes. Additionally, the veto also removes background contributions from single-pronged hadronic decays of τ leptons.

Event The topology of the event is required to pass a threshold of at least $\alpha_{\mathrm{T}} > 0.55$, a requirement which itself varies as a function of the H_T category being considered, chosen such that the signal triggers are in the efficiency plateau, as summarised

Table 6.3 Jet E_{T} and α_{T} thresholds per H_T bin.

H_T bin	200–275	275–325	325–375	>375
Lead jet (GeV)	73.3	73.3	86.7	100.0
Second jet (GeV)	73.3	73.3	86.7	100.0
All other jets (GeV)	36.7	36.7	43.3	50.0
α_{T}	0.65	0.60	0.55	0.55

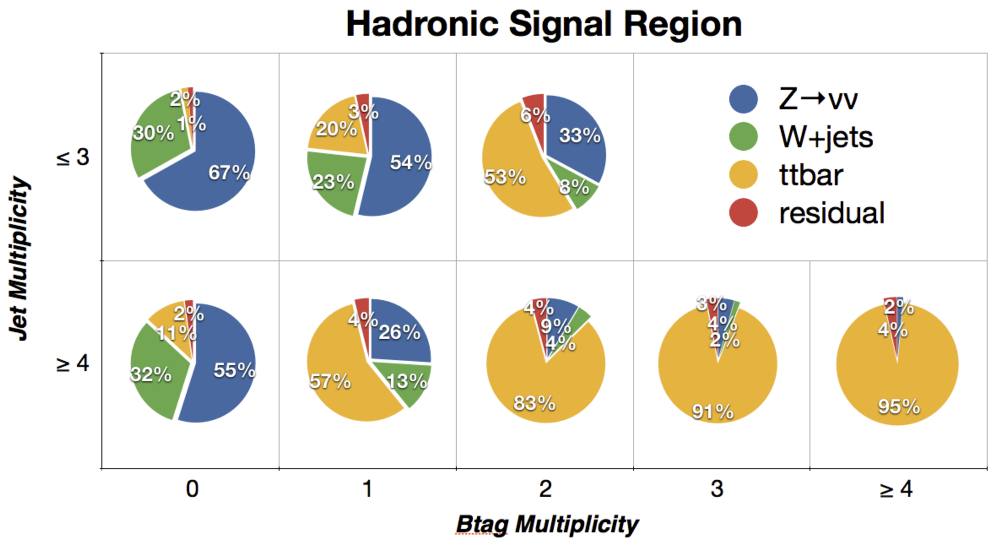

Fig. 6.5 The breakdown of the total electroweak background into component processes as a function of n_{jet} and n_{b}, for H_T >200 GeV.

in table 6.3. While no absolute $\not{E}_T$ requirement is made, the cut on α_{T} imposes an implied threshold, maintaining the analysis' sensitivity to very low regions of $\not{E}_T$ as shown by figure 6.2. Furthermore, events are required to have $\not{H}_T/\not{E}_T < 1.25$ and $\Delta\phi^*_{min} > 0.3$ (defined later in chapter 7).

A breakdown of the EWK background composition is shown in Figure 6.5, split into the main categories of $Z \to \nu\bar{\nu}$, $\mathrm{W} + \mathrm{jets}$, $\mathrm{t\bar{t}}$ and all remaining residual backgrounds, such as single top quark, diboson and Drell-Yann processes.

6.5 Example distributions and cutflow

Example distributions from MC simulations of α_{T}, H_T, $\not{H}_T$ and jet p_{T} are shown in figure 6.6. Example cutflow yields are shown in table 6.4 for data in the $H_T > 375$ GeV region, with an inclusive selection on n_{jet} and n_{b}.

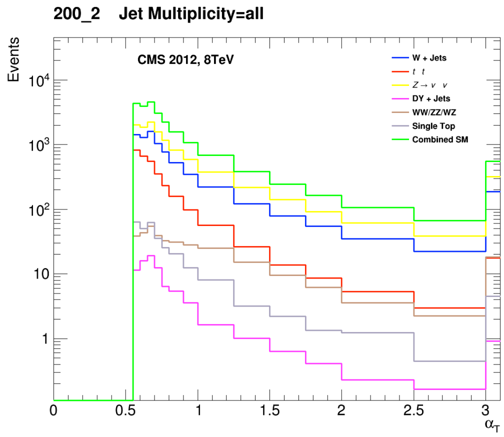

(a) α_{T}

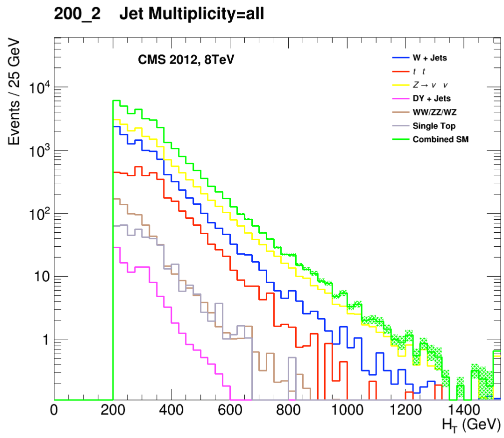

(b) H_T

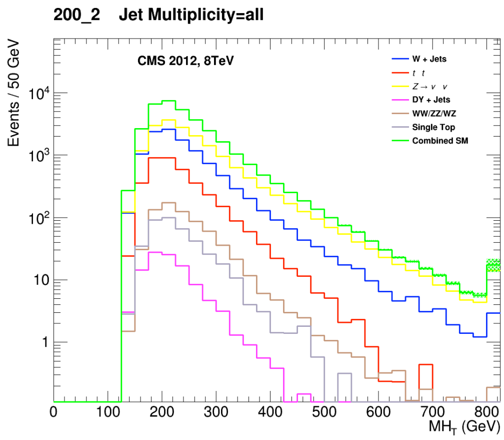

(c) $\not{H}_T$

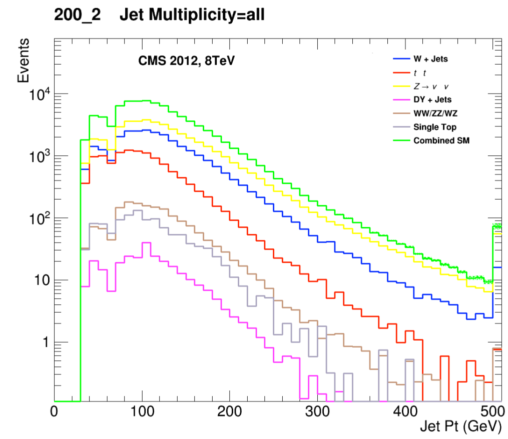

(d) Jet p_{T}

Fig. 6.6 MC distributions for the full hadronic signal selection. The sum of the individual sample contributions is shown in green. Plots are for $H_T > 200$ GeV, $n_{\text{jet}} \geq 2, n_{\text{b}} \geq 0$.

Table 6.4 The cutflow of the hadronic selection in data. The subscript 'fail' indicates an object which did not meet all ID requirements, and so is not considered as a 'common object'. The event selection follows an inclusive selection in data of $H_T > 375$ GeV, $n_{\mathrm{jet}} \geq 2$ and $n_{\mathrm{b}} \geq 0$.

Cut Name	Eff (%)	N
Trigger	100.00	12843698.00
Good Event JSON Filter	95.32	12242217.00
$n_{\mathrm{jet}} \geq 2$	98.93	12110634.00
MET Filters	98.68	11951541.00
Vertex Noise Filter	99.92	11941983.00
DeadECAL Filter	25.59	3056360.00
$n_e = 0$	98.62	3014305.00
$n_\gamma = 0$	97.82	2948741.00
$n_\mu = 0$	98.77	2912517.00
Leading jet $p_{\mathrm{T}} > 100$ GeV	98.20	2860068.00
Leading jet $\eta < 2.5$	97.29	2782463.00
Sub-Leading jet $p_{\mathrm{T}} > 100$ GeV	84.24	2343910.00
$n_{j,fail} = 0$	83.45	1955899.00
$\Delta R(\mu^i_{fail}, jet^j) < 0.5$	98.87	1933858.00
$(\sum^{n_{vertices}} p_{\mathrm{T}})$ / H_T	100.00	1933855.00
recHitCut	98.44	1903597.00
$n_{SIT} = 0$	85.61	1629716.00
$H_T > 375$ GeV	93.45	1522986.00
$\alpha_{\mathrm{T}} > 0.55$	0.55	8305.00
$\not{H}_T / \not{E}_T < 1.25$	66.82	5549.00
$\Delta\phi^*_{min} > 0.3$	90.83	5040.00

Chapter 7

Background Estimation

Predictions of EWK SM backgrounds are made using independent control regions designed to mimic a specific background process observed in the signal region. These regions are orthogonal to the signal region due to the selection of leptons or photons - particles which are subsequently ignored such that the selection kinematics of each event is kept similar to the corresponding process. For each sample, Transfer Factors (TF) are constructed from yields in MC, to extract a prediction in the signal region for a given process. This process is described at length in section 7.1. The validity of this procedure is extensively tested using a suite of Closure Tests, probing multiple characteristics of the prediction technique while allowing for H_T-dependent systematic errors to be derived on the prediction.

Predictions made using this technique alone are considered as "primitive" predictions and are used only in analysis development and the derivation of background systematics. In order to determine final background counts for interpretation and limit-setting, a fit is made across all signal and control regions, using the likelihood model as described later in chapter 8. The derived transfer factors and individual yields enter as terms in the likelihood, where all related systematics, potential correlations and signal contamination are accounted for.

Residual contamination from QCD processes are removed through additional cleaning cuts. Studies performed in a QCD enriched sideband region in α_{T} lead to the definition of these cuts, as described in section 7.4, ensuring no significant QCD remains.

7.1 Overview of Electroweak background prediction method

A transfer factor is constructed from MC samples as the ratio of the yield in the signal region,
$N_{MC}^{signal}\Big(H_T, n_{\rm jet}, n_{\rm b}\Big)$, and the yield of a given control region,
$N_{MC}^{control}\Big(H_T, n_{\rm jet}, n_{\rm b}\Big)$, as a function of the analysis binning, H_T, $n_{\rm jet}$ and $n_{\rm b}$, defined as:

$$TF = \frac{N_{MC}^{signal}\Big(H_T, n_{\rm jet}, n_{\rm b}\Big)}{N_{MC}^{control}\Big(H_T, n_{\rm jet}, n_{\rm b}\Big)}. \tag{7.1}$$

For a given H_T, $n_{\rm jet}$ and $n_{\rm b}$ bin, the TF is used to extrapolate a yield in data from the control region, $N_{data}^{control}\Big(H_T, n_{\rm jet}, n_{\rm b}\Big)$, to give a prediction in the signal region $N_{pred}^{signal}\Big(H_T, n_{\rm jet}, n_{\rm b}\Big)$, using:

$$N_{pred}^{signal}\Big(H_T, n_{\rm jet}, n_{\rm b}\Big) = N_{data}^{control}\Big(H_T, n_{\rm jet}, n_{\rm b}\Big) \times TF. \tag{7.2}$$

The control samples are statistically independent and each used for predicting specific background processes.

MC yields are defined by process from the following samples: W + jets ($N_{\rm W}$), $\rm t\bar{t}$ + jets ($N_{\rm t\bar{t}}$), DY + jets ($N_{\rm DY}$), γ + jets(N_γ), single top + jets ($N_{\rm top}$), WW + jets, WZ + jets and ZZ + jets ($N_{\text{di-boson}}$), and $Z \to \nu\bar{\nu}$ + jets ($N_{Z\to\nu\bar{\nu}}$).

The denominator of each transfer factor is constructed using the sum of *all* MC sample yields, for a given control region and analysis category:

$$N_{MC}^{control}\Big(H_T, n_{\rm jet}, n_{\rm b}\Big) = N_{\rm W} + N_{\rm t\bar{t}} + N_{\rm DY} + N_\gamma + N_{\rm top} + N_{\text{di-boson}} + N_{Z\to\nu\bar{\nu}}. \tag{7.3}$$

The numerator is constructed according to the b tag multiplicity being considered. For $n_{\rm b} \leq 1$, the μ+jets control region is used to predict lost-lepton background, e.g. $\rm t\bar{t}$ + jets and W + jets. All MC samples are therefore used with the exception of $Z \to \nu\bar{\nu}$ + jets:

$$N_{MC}^{signal}\Big(H_T, n_{\rm jet}, n_{\rm b} \leq 1\Big) = N_{\rm W} + N_{\rm t\bar{t}} + N_{\rm DY} + N_\gamma + N_{\rm top} + N_{\text{di-boson}}. \tag{7.4}$$

In this $n_{\rm b}$ region the $Z \to \nu\bar{\nu}$ + jets component of the background is predicted with the $\mu\mu$+jets and γ+jets control samples, using only the $Z \to \nu\bar{\nu}$ MC yields:

$$N_{MC}^{signal}\Big(H_T, n_{\text{jet}}, n_{\text{b}} \leq 1\Big) = N_{Z\to\nu\bar{\nu}}. \tag{7.5}$$

For $n_{\text{b}} \geq 2$, the μ+jets sample is used to produce a prediction for all SM processes, including $Z \to \nu\bar{\nu}$, and therefore the numerator of the TF is defined as:

$$N_{MC}^{signal}\Big(H_T, n_{\text{jet}}, n_{\text{b}} \geq 2\Big) = N_{\text{W}} + N_{\text{t}\bar{\text{t}}} + N_{\text{DY}} + N_{\gamma} + N_{\text{top}} + N_{\text{di-boson}} + N_{Z\to\nu\bar{\nu}}, \tag{7.6}$$

or equivalently:

$$N_{MC}^{signal}\Big(H_T, n_{\text{jet}}, n_{\text{b}} \geq 2\Big) = N_{MC}^{signal}\Big(H_T, n_{\text{jet}}, n_{\text{b}} \leq 1\Big) + N_{Z\to\nu\bar{\nu}}. \tag{7.7}$$

The $\mu\mu$+jets and γ+jets control samples are not used beyond the $n_{\text{b}} \leq 1$ categories due to the statistical limitations of such samples at high b tag multiplicities. A full summary of the control regions used for predictions per analysis category is shown in table 7.1.

It should be noted that although two separate control samples are used to estimate the $Z \to \nu\bar{\nu}$ background contribution, the result of each is considered by the global likelihood fit to produce the final background prediction.

Table 7.1 The control samples used to produce SM background predictions for each analysis category (n_{b}, n_{jet}).

n_{jet}	n_{b}	Control samples
2–3	0	μ+jets, $\mu\mu$+jets, γ+jets
2–3	1	μ+jets, $\mu\mu$+jets, γ+jets
2–3	2	μ+jets
≥4	0	μ+jets, $\mu\mu$+jets, γ+jets
≥4	1	μ+jets, $\mu\mu$+jets, γ+jets
≥4	2	μ+jets
≥4	3	μ+jets
≥4	≥ 4	μ+jets

By employing a technique that uses a ratio of MC yields, direct dependence on MC modelling is greatly reduced. Sources of error inherent to MC samples, such as mismodelling effects, will cancel in the ratio. These errors can potentially include kinematic mismodelling, which would affect analysis acceptance, and mismodelling of instrumental effects, which could affect object reconstruction efficiencies. However, any remaining systematics such as these and others are probed using dedicated Closure Tests (CT), described in detail in section 7.3.1.

7.2 Control samples

Control sample definitions are designed such that they are as kinematically similar as possible to the signal region, with the exception of a selected 'tag' muon or photon. The 'tagged' particle is then subsequently ignored for the calculation of all analysis variables, such as H_T, $\not{E}_T$, α_{T} etc. Other differences include mass-window and minor kinematic cuts, aimed at enriching the control samples in certain processes. Due to the selection of the tagged lepton or photon, the control samples are orthogonal to the signal region and therefore minimise any possible signal contamination. However, a full treatment of the signal-contamination and sample cross-correlation is taken into account in the background fit and final limit-setting.

The following sections will describe the control regions in more detail, including their targeted background estimations, selection cuts specific to each and their trigger requirements.

7.2.1 μ+jets

The μ+jets control sample is constructed by selecting a single muon with associated jets. This region is used to predict backgrounds from processes such as W + jets and $\mathrm{t\bar{t}}$ + jets. This covers not only the leptonic decays of such productions, where the lepton is not identified for whatever reason, but also the hadronic decays of tau leptons [from high-p_{T} W bosons]. The event selection therefore is optimised to select W bosons decaying to a muon and a neutrino in the phase-space of the signal.

Triggers

Events are collected using the loosely-isolated, η-restricted `HLT_IsoMu24_eta2p1` trigger, which was in place throughout the 8 TeV data-taking period. The efficiency of this trigger was measured by the muon *POG* in bins of the muon p_{T} and η, as summarised in table 7.2. Statistical uncertainties are at the per-mille level, and systematics are taken to be 1%.

Table 7.2 Muon trigger efficiencies (%) for the μ+jets selection listed by H_T bin and n_{jet} category.

n_{jet}	HT bin low edge (GeV)											
	150	200	275	325	375	475	575	675	775	875	975	1075
2–3	87.2	87.5	87.8	87.9	88.1	88.2	88.4	88.5	88.6	88.8	88.7	88.4
≥4	88.1	88.1	88.2	88.4	88.6	88.8	88.9	89.0	89.1	89.0	89.0	89.6

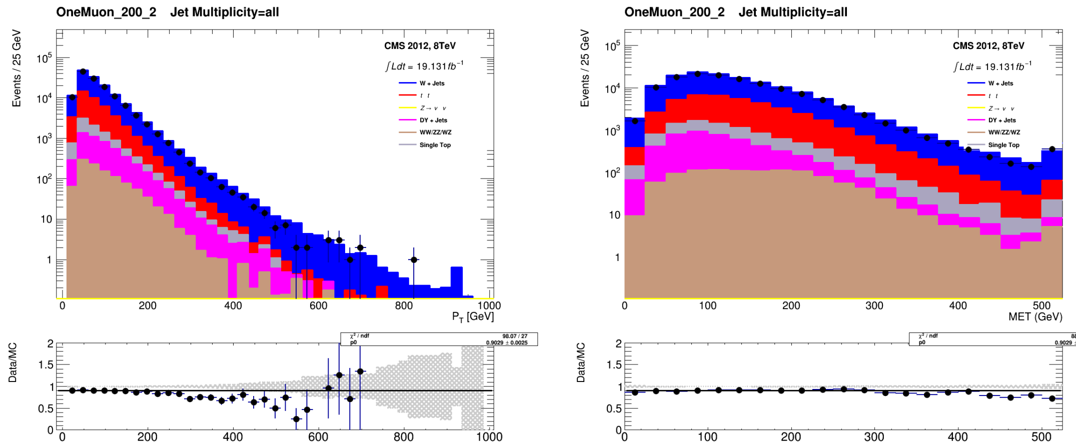

(a) μ p_{T} (b) $\not{E}_T$ (corrected for μ)

Fig. 7.1 Comparison of data with MC for the μ+jets control selection. Plots are for $H_T > 200$ GeV, $n_{\text{jet}} \geq 2, n_{\text{b}} \geq 0$.

Selection Criteria

A single tight isolated muon is selected, with $p_{\text{T}} > 30$ GeV and $|\eta| <2.1$. The transverse mass of the W, reconstructed by the μ and the $\not{E}_T$ (originating from the ν_μ), is required to be in a loose window around m_W, $30 < M(\mu, \not{E}_T) < 125$ GeV. Events are vetoed if $\Delta R(\mu, jet_i) < 0.5$, for all jets i in the event. To keep the selection as close to the signal region as possible, other cuts such as the single isolated track veto and $\not{H}_T/\not{E}_T$ cuts are also applied.

Specifically for the μ+jets (and $\mu\mu$+jets) control samples, no α_{T} requirement is made in order to increase the statistics and therefore the predictive power of the samples. This is possible as other requirements, in particular the requirement of a single muon and a specific invariant mass window, greatly reduce any potential contamination from QCD MJ events. The viability of this is specifically tested by dedicated closure tests described later in section 7.3.1.

Example distributions of μ p_{T} and μ-corrected $\not{E}_T$ for this selection are shown in figure 7.1.

7.2.2 $\mu\mu$+jets

The $\mu\mu$+jets sample is constructed to predict background contributions from $Z \to \nu\bar{\nu}$ decays, mimicking this decay via the kinematically similar $Z \to \mu\mu + jets$ process where both muons are subsequently ignored. The sample is used to provide low H_T coverage for the $Z \to \nu\bar{\nu}$ background prediction, where the γ+jets sample (section 7.2.3) is unable to do so.

Triggers

The trigger used is the same as for the μ+jets sample, as described in section 7.2.1. Trigger efficiencies are significantly improved for the dimuon selection given that either of the muons can cause a positive trigger decision, as shown in table 7.3. Systematic errors are considered of the same magnitude as for the μ+jets trigger efficiencies.

Table 7.3 Muon trigger efficiencies (%) for the $\mu\mu$+jets selection listed by H_T bin and n_{jet} category.

n_{jet}	HT bin low edge (GeV)											
	150	200	275	325	375	475	575	675	775	875	975	1075
2–3	98.4	98.5	98.5	98.6	98.6	98.6	98.6	98.7	98.6	98.7	98.7	98.7
≥ 4	98.4	98.4	98.4	98.6	98.5	98.6	98.6	98.6	98.6	98.6	98.8	98.7

Selection Criteria

The selection for the $\mu\mu$+jets sample is very similar to that of the μ+jets sample, described in section 7.2.1, with differences chosen to enrich the sample in Z bosons decaying to pairs of muons in the kinematic phase space of the signal region. Two tight isolated muons are selected, each with $p_{\text{T}} > 30$ GeV and $|\eta| < 2.1$. Their invariant mass is required to be tight around m_Z, $m_Z - 25 < M_{\mu_1\mu_2} < m_Z + 25$ GeV. Furthermore, a veto is made on events satisfying $\Delta R(\mu_i, jet_j) < 0.5$, for every muon i and every jet j. Similarly as in the μ+jets sample selection, no α_{T} requirement is made.

Example distributions of transverse mass of the muon pair, $M_T(\mu\mu)$, and μ_2 p_{T} for this selection are shown in figure 7.2.

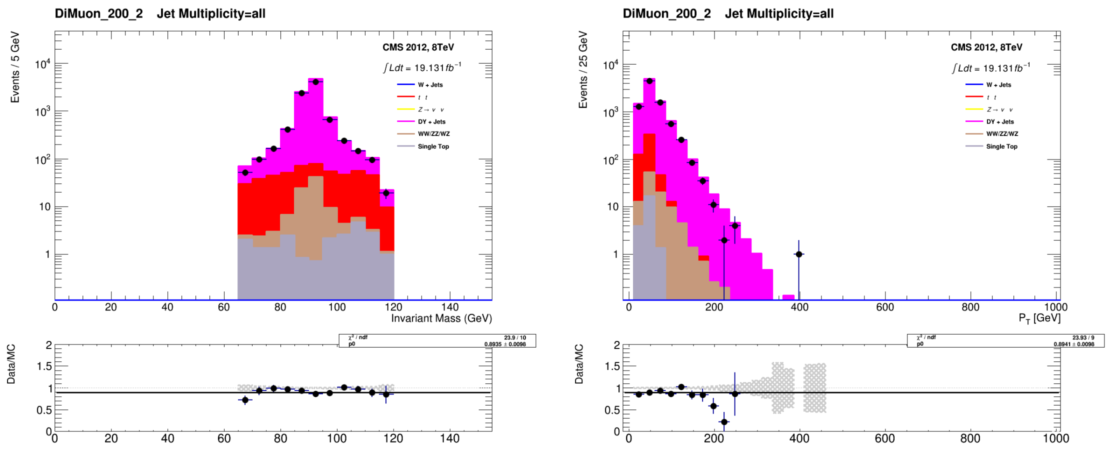

(a) $M_T(\mu,\mu)$ (b) Second μ p_{T}

Fig. 7.2 Comparison of data with MC for the $\mu\mu$+jets control selection. Plots are for $H_T > 200$ GeV, $n_{\mathrm{jet}} \geq 2, n_{\mathrm{b}} \geq 0$.

7.2.3 γ+jets

The γ+jets sample is used to predict the $Z \to \nu\bar{\nu}$ background contribution, given it's similar kinematics when the γ is ignored from the event, as well as a larger production cross section relative to $\mu\mu$+jets. Due to trigger thresholds, the γ+jets sample cannot make predictions for $H_T < 375$ GeV, and so is complimentary to the $\mu\mu$+jets sample prediction.

Triggers

Events are collected using the `HLT_Photon150` trigger. The trigger's efficiency is measured using the `HLT_Photon90` trigger as a reference and is found to be 100% efficient for $E_T^{\gamma} > 165$ GeV and $H_T > 375$ GeV,

as shown by the turn on curves in figure 7.3.

Selection Criteria

Exactly one photon satisfying tight isolation criteria is required, with $p_{\mathrm{T}} > 165$ GeV and $|\eta| < 1.45$. In addition, events are vetoed if $\Delta R(\gamma, jet_i) < 1.0$ is satisfied, for all jets i in the event.

An example distribution of the γ p_{T} for this selection is shown in figure 7.4.

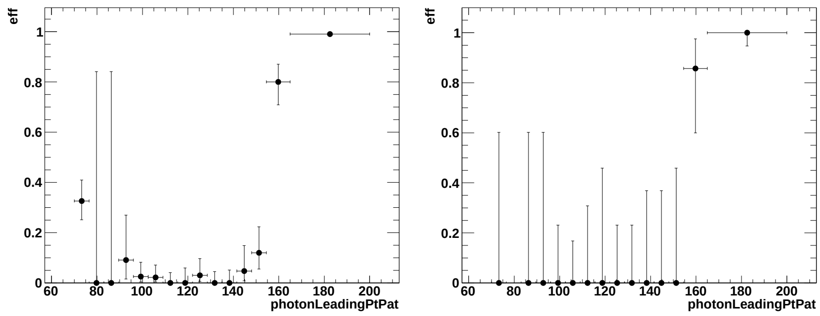

(a) $2 \leq n_{\mathrm{jet}} \leq 3$ (b) $n_{\mathrm{jet}} \geq 4$

Fig. 7.3 Efficiency turn-on curves for the photon trigger, based on the γ+jets selection, for $H_T > 375$ GeV, with $2 \leq n_{\mathrm{jet}} \leq 3$ (Left) and $n_{\mathrm{jet}} \geq 4$ (Right).

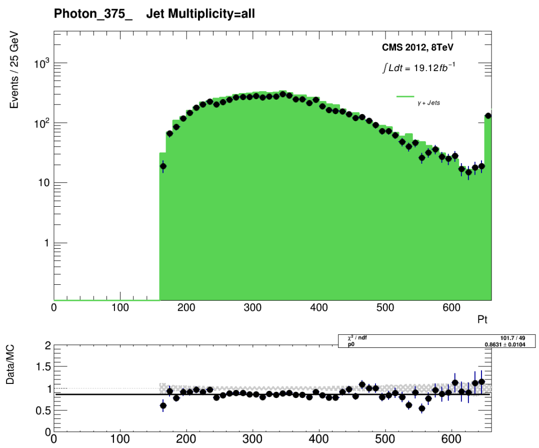

(a) γ p_{T}

Fig. 7.4 Comparison of data with MC for the γ+jets control selection. Plot is for $H_T > 200$ GeV, $n_{\mathrm{jet}} \geq 2, n_{\mathrm{b}} \geq 0$.

7.3 Systematic uncertainties on SM background predictions

In order to probe the levels at which the transfer factors are sensitive to relevant uncertainties, a statistically powerful ensemble of Closure Tests (CT's) have been designed. The CT method works by constructing a TF to extrapolate from one sub-region of a particular control sample into another control sample sub-region. In doing so, tests can be designed to specifically probe any potential sources of bias in the transfer factors.

7.3.1 Closure tests

Closure tests are performed as a function of H_T, in the two n_{jet} categories, $2 \leq n_{\text{jet}} \leq 3$ and $n_{\text{jet}} \geq 4$. The level of closure is represented by the statistical consistency between predicted and observed yields for each test, in the absence of any assumed systematic uncertainty. The test statistic is defined as $(N_{obs} - N_{pred})/N_{pred}$, with any bias being observed as a statistically significant deviation from zero, or trend in H_T.

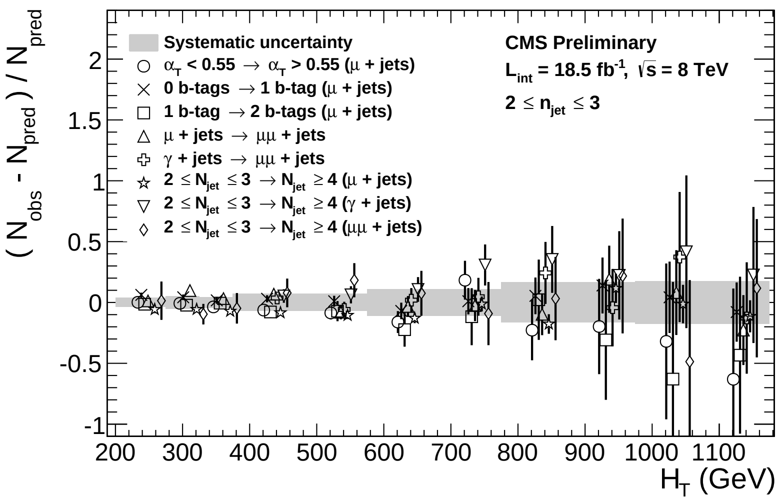

(a) $2 \leq n_{\text{jet}} \leq 3$

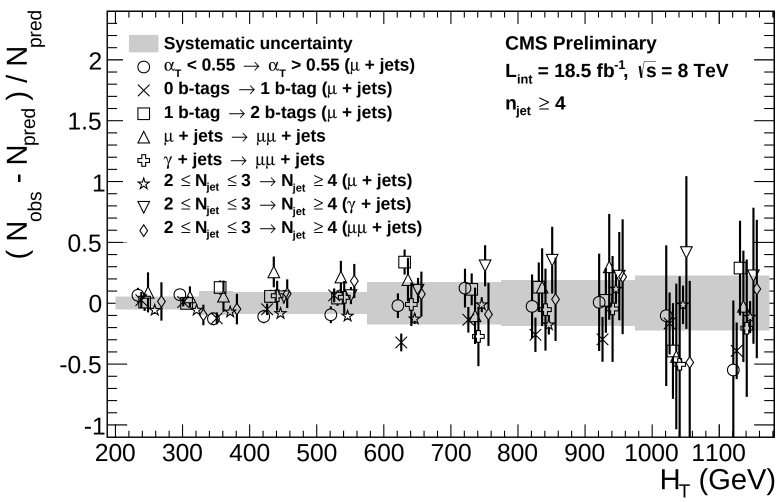

(b) $n_{\text{jet}} \geq 4$

Fig. 7.5 The results of the eight core closure tests (open symbols), shown over the systematic uncertainty bands for each of the five H_T regions (shaded grey), for the two jet multiplicity regions (a) $2 \leq n_{\text{jet}} \leq 3$ and (b) $n_{\text{jet}} \geq 4$.

Figure 7.5 shows a summary of the eight closure tests considered as 'core' tests for the analysis, split into both $2 \leq n_{\mathrm{jet}} \leq 3$ (figure 7.5a) and $n_{\mathrm{jet}} \geq 4$ (figure 7.5b). It should be noted that numerous other tests are also considered, but that these eight represent those deemed most important to the background prediction and are therefore used to derive related uncertainties.

The first test, represented by open circles, tests the modelling of the α_{T} variable in the μ+jets control sample. In the analysis a prediction is made between the μ+jets sample, which has no α_{T} requirement, and the signal region, with it's tight α_{T} requirement. This particular test probes the validity of the prediction between the 'bulk' of the α_{T} distribution in the control sample and the 'tail' of the distribution in the signal region. A similar test, not shown here, is performed for the $\mu\mu$+jets control sample.

The next two tests, represented by crosses and open squares, probe the different b tag multiplicities in the μ+jets control sample. The b tag requirements greatly change the relative admixture of, for example, $\mathrm{W} + \mathrm{jets}$ (n_{b} =0) and $\mathrm{t\bar{t}} + \mathrm{jets}$ (n_{b} =1) events. It is important to note that this test is considered conservative, given that the admixture of $\mathrm{W} + \mathrm{jets}$ to $\mathrm{t\bar{t}} + \mathrm{jets}$ events varies minimally between control and signal regions, where this extrapolation is made between identical n_{b} categories in the analysis. Given the focus on b tagging, these tests also investigate the modelling of b quark jets in the simulated data.

Represented by open triangles, a similar test is made for the relative admixture of $\mathrm{Z}(\nu\nu) + \mathrm{jets}$ to $\mathrm{W} + \mathrm{jets}$ and $\mathrm{t\bar{t}} + \mathrm{jets}$, by predicting between the μ+jets and $\mu\mu$+jets control regions. Again, this test is considered conservative, and also probes the muon reconstruction and trigger efficiencies between the different muon multiplicities. These are however already well studied by the muon *POG* using data-driven techniques.

As described in section 7.1, the $Z \to \nu\bar{\nu}$ prediction is made from both the γ+jets and $\mu\mu$+jets samples, and so a test is constructed to predict between these two orthogonal control regions, as shown by the open crosses.

The final three tests, indicated by open stars, triangles and diamonds, make predictions between the two different jet multiplicity categories in each control sample, thereby testing jet reconstruction and modelling. These tests are also considered conservative as the analysis only predicts between identical n_{jet} categories in the control and signal regions.

Summary plots of these eight tests are shown in figure 7.5, indicating no statistically significant biases or H_T dependencies. Figures 7.6a and 7.6c show zeroeth order polynomial fits (blue lines) made to each individual test to assess the level of any

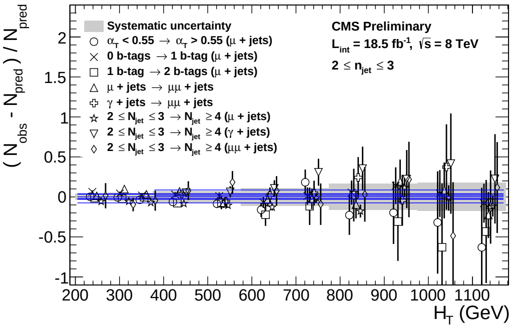

(a) $2 \leq n_{\mathrm{jet}} \leq 3$ (constant function fits)

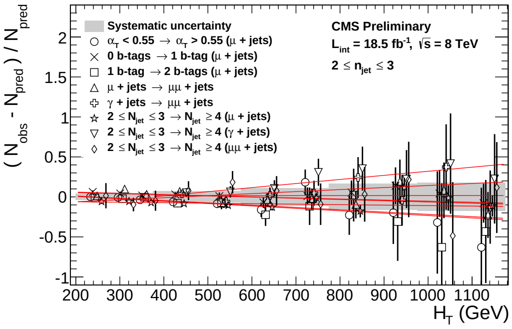

(b) $2 \leq n_{\mathrm{jet}} \leq 3$ (linear function fits)

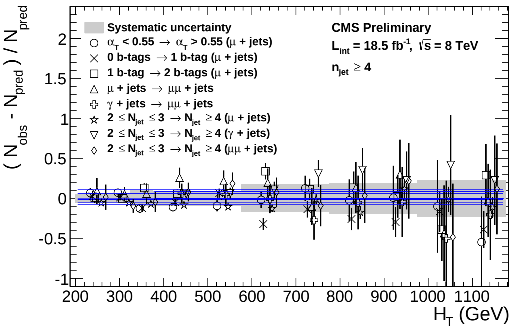

(c) $n_{\mathrm{jet}} \geq 4$ (constant function fits)

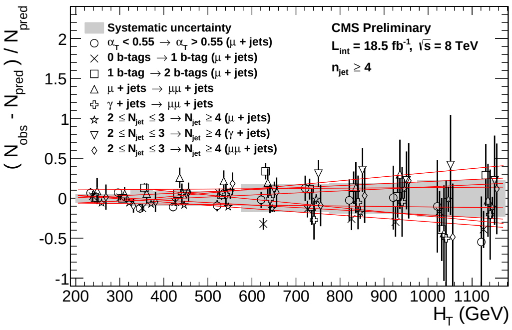

(d) $n_{\mathrm{jet}} \geq 4$ (linear function fits)

Fig. 7.6 The results of the eight core closure tests (open symbols), shown over the systematic uncertainty bands for each of the five H_T regions (shaded grey), for the two jet multiplicity regions (a) $2 \leq n_{\mathrm{jet}} \leq 3$ and (b) $n_{\mathrm{jet}} \geq 4$ separately. Included are zeroeth order (left column, blue) and first order (right column, red) fits to each individual closure test.

potential bias present. In addition, first order polynomial fits (red lines) are made to assess any potential H_T dependence present in the tests, as shown in figures 7.6b and 7.6d. The best-fit values, χ^2 and p-values obtained from both fits are summarised for each n_{jet} category in tables 7.4, 7.5 and 7.6.

The fits show no significant biases or trends and therefore indicate good closure. The only exception is the 0 b-jets $\rightarrow$1 b-jet (μ+jets) test for the $n_{\mathrm{jet}} \geq 4$ category which has a sub-optimal goodness of fit value. This is attributed to upwards and downwards fluctuations in the adjacent 475-575 GeV and 575-675 GeV bins respectively. Also shown in table 7.5, when the same fit is made after summing these two bins significantly improved fit parameters are observed. This leads to the conclusion that these two bins contain a statistical fluctuation as opposed to a systematic bias.

Table 7.4 Results of zeroeth (i.e. constant) and first order (i.e. linear) fits for five sets of closure tests, performed in the $2 \leq n_{\text{jet}} \leq 3$ category.

		Constant fit				Linear fit	
Closure test	Symbol	Best fit value	χ^2	d.o.f.	p-value	Slope (10^{-4})	p-value
$\alpha_{\text{T}} < 0.55 \rightarrow \alpha_{\text{T}} > 0.55$ (μ+jets)	Circle	-0.02 ± 0.01	11.3	10	0.34	-2.9 ± 1.1	0.83
0 b-jets $\rightarrow$1 b-jet (μ+jets)	Times	0.04 ± 0.01	5.8	10	0.83	-1.5 ± 0.9	0.97
1 b-jet $\rightarrow$2 b-jets (μ+jets)	Square	-0.03 ± 0.02	5.3	10	0.87	-3.0 ± 1.7	0.99
μ+jets $\rightarrow \mu\mu$+jets	Triangle	0.03 ± 0.02	12.3	10	0.27	-1.3 ± 1.1	0.28
γ+jets $\rightarrow \mu\mu$+jets	Cross	-0.02 ± 0.03	3.0	7	0.88	0.0 ± 2.7	0.81

Table 7.5 Results of zeroeth (i.e. constant) and first order (i.e. linear) fits for five sets of closure tests, performed in the $2 \leq n_{\text{jet}} \leq 3$ category. An additional test marked with a † is listed, as described in the text.

		Constant fit				Linear fit	
Closure test	Symbol	Best fit value	χ^2	d.o.f.	p-value	Slope (10^{-4})	p-value
$\alpha_{\text{T}} < 0.55 \rightarrow \alpha_{\text{T}} > 0.55$ (μ+jets)	Circle	-0.02 ± 0.02	17.6	10	0.06	-3.1 ± 1.7	0.11
0 b-jets $\rightarrow$1 b-jet (μ+jets)	Times	-0.06 ± 0.02	31.2	10	0.00	-4.1 ± 1.2	0.02
0 b-jets $\rightarrow$1 b-jet (μ+jets)†	Times	-0.05 ± 0.02	13.4	9	0.15	-3.9 ± 1.3	0.78
1 b-jet $\rightarrow$2 b-jets (μ+jets)	Square	0.06 ± 0.02	13.7	10	0.19	2.5 ± 1.6	0.28
μ+jets $\rightarrow \mu\mu$+jets	Triangle	0.11 ± 0.05	4.8	10	0.90	0.4 ± 2.7	0.85
γ+jets $\rightarrow \mu\mu$+jets	Cross	-0.00 ± 0.07	2.3	7	0.94	-5.3 ± 4.7	0.99

Table 7.6 Results of zeroeth (i.e. constant) and first order (i.e. linear) fits for the three sets of closure tests probing the accuracy of jet multiplicity modelling in MC, for each control sample.

		Constant fit				Linear fit	
Sample	Symbol	Best fit value	χ^2	d.o.f.	p-value	Slope (10^{-4})	p-value
μ+jets	Star	-0.08 ± 0.01	9.3	10	0.50	0.6 ± 0.7	0.48
γ+jets	Inverted triangle	0.09 ± 0.04	3.7	7	0.82	5.1 ± 3.2	0.98
$\mu\mu$+jets	Diamond	-0.00 ± 0.05	4.7	10	0.91	2.5 ± 2.9	0.92

7.3.2 Background systematic uncertainty summary

Under the assumption of closure for the eight core tests, systematic errors are derived for each n_{jet} category in seven regions of H_T. Values are calculated by summing in quadrature the weighted mean and sample variance for all eight tests in a given H_T region. These values are summarised in table 7.7 and also in the summary plots of figure 7.5, shown as grey bands.

Systematic values are considered as fully uncorrelated between the different analysis categories and the H_T regions, which is again considered as a conservative approach given that some correlation is to be expected, for example between adjacent H_T bins.

Table 7.7 Summary of the magnitude of systematic uncertainties (%) derived from the eight core closure tests, for each n_{jet} category and H_T region.

	H_T region (GeV)						
n_{jet}	200–275	275–325	325–375	375–575	575–775	775-975	> 975
2–3	4	6	6	8	12	17	19
$\geq$4	6	6	11	11	18	20	26

7.4 Eliminating QCD events

While the α_{T} requirement removes many orders of magnitude of QCD events, there still exist scenarios in which these events may pass the signal region selection. Accordingly, further requirements are made to ensure the search region is free of any residual QCD contamination, such that it is negligible when compared to the uncertainty on the EWK background prediction.

7.4.1 Multiple jets below threshold

Events are able to acquire non-negligible amounts of $\not{H}_T$ without the presence of real $\not{E}_T$ if multiple jets are below the jet p_{T} threshold and their configuration conspires to form a topology that gives high values of α_{T}. Such events will contain a disparity between the $\not{E}_T$ and $\not{H}_T$ variables, given that the former is reconstructed using energy deposits and the latter with reconstructed jet objects. Figure 7.7 shows the contribution of QCD at high $\not{H}_T/\not{E}_T$ values, even following the α_{T} requirement. To protect against this scenario, events are required to have $\not{H}_T/\not{E}_T < 1.25$.

7.4.2 Instrumental effects

Fake $\not{H}_T$ may also be produced if jets overlap with areas of the calorimeter system which are damaged or known to be faulty (hereby referred to as 'dead'), and jets are mismeasured or lost as a result. To protect against this, for a given jet j the angular separation between the event $\not{H}_T$, calculated excluding jet j, and the jet itself is defined as:

$$\Delta\phi^*_j = \Delta\phi\Big(\overrightarrow{p_{\text{T}}}_j, -\sum_{i\neq j}\overrightarrow{p_{\text{T}}}_i\Big). \tag{7.8}$$

An advantage of this variable with respect to the often used $\Delta R(\overrightarrow{p_{\text{T}}}_j, \not{H}_T)$ is it's detection of spurious missing energy vectors caused by both under-measurements and

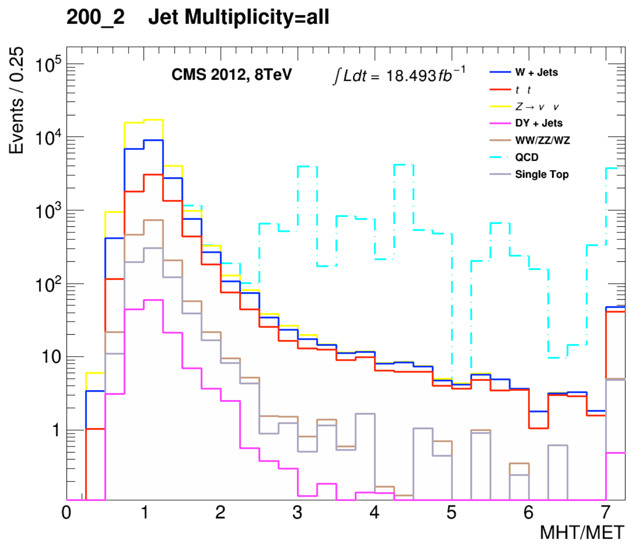

Fig. 7.7 The $\not{H}_T/\not{E}_T$ distribution of MC events following the hadronic selection criteria, minus the nominal $\not{H}_T/\not{E}_T$ requirement.The MC yields are stacked, with the QCD contribution shown in cyan. The plot is for a fully inclusive selection of $n_{\mathrm{b}} \geq 0$, $n_{\mathrm{jet}} \geq 2$ and $H_T > 200$ GeV.

over-measurements of a jets energy. A small value of $\Delta\phi^*_j$ indicates that the momentum vector of the jet j is aligned with the $\not{H}_T$ vector, implying the jet to be mismeasured. Events are vetoed if a jet with $\Delta\phi^* < 0.5$ is within $\Delta R < 0.3$ of a known dead region of the calorimeter.

To protect against further jet mismeasurements arising due to instrumental effects, multiple event filters are applied. However, previously undiscovered and therefore rare detector effects may still be present. To check for such issues the jet giving the minimum $\Delta\phi^*$ value in an event, $\Delta\phi^*_{min}$, is found and a single entry of the η and ϕ direction of the jet's axis is entered into a map of the detector, as shown in figure 7.8. Any areas of instrumental issue would be visible as clusters of high event counts. Figures 7.8a and 7.8b show the detector map and the 1D distribution of counts before the dead ECAL filter is applied, with areas of potential instrumental defects clearly visible, notably as outliers in 1D distribution. Following the application of the dead ECAL filter the hotspot areas and the corresponding outliers are removed, as seen in figures 7.8c and 7.8d. The lack of localised high-count regions or the presence of a tail in the 1D distribution indicate there to be no significant instrumental issues remaining.

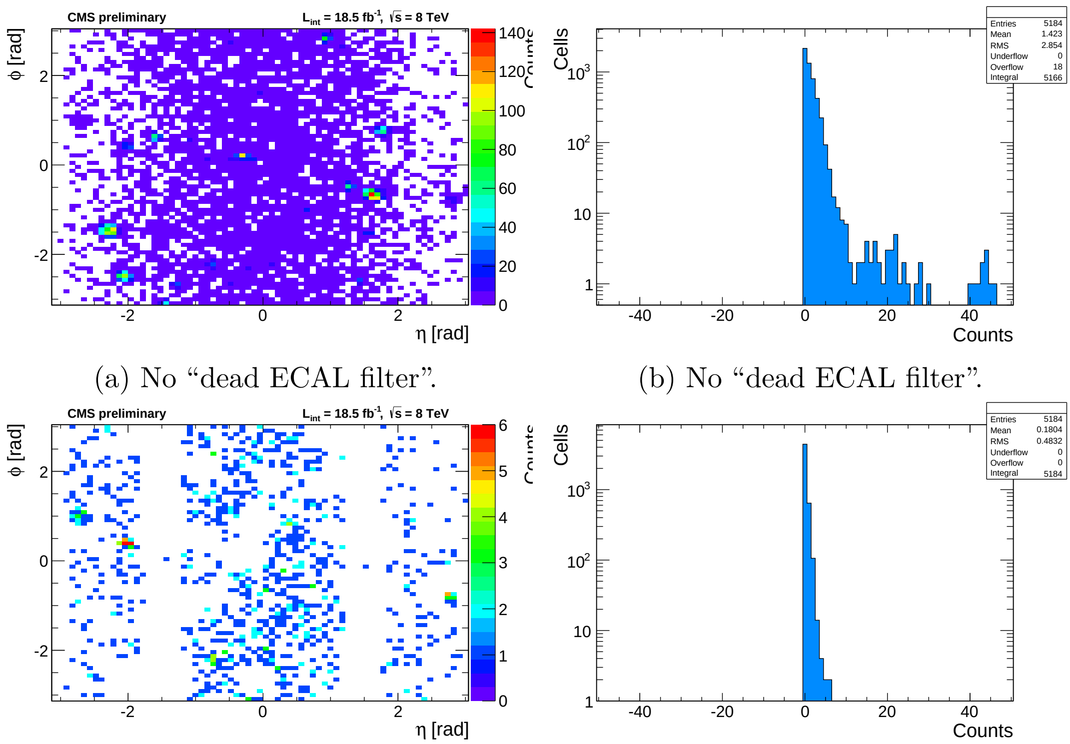

(a) No "dead ECAL filter".

(b) No "dead ECAL filter".

(c) With "dead ECAL filter".

(d) With "dead ECAL filter".

Fig. 7.8 Distribution of jets in (η, ϕ)-space that are responsible for the $\Delta\phi^*_{min}$ value of an event, with (a, b) and without (c, d) the "dead ECAL filter" requirement applied as part of the signal region selection.

7.4.3 Heavy-flavour jet decays

Jets can also appear to be mismeasured if the parton shower contains heavy flavour mesons which decay semi-leptonically. In rare circumstances, these decays can give the largest fraction of the available momenta to the subsequent neutrino, leading to significant amounts of real $\not\!\!E_T$ and soft-leptons which can evade the lepton vetoes. This effect is compounded when multiple neutrinos are produced in the shower, with a significant fraction of the jet's energy therefore evading detection.

An event display of a typical event is shown in figure 7.12. It is important to note the high amount, 185 GeV, of generator level $\not\!\!E_T$ ('genmetP4True', thin pink arrow) pointing along the axis of a reconstructed jet with $p_\mathrm{T} = 119$ GeV (bold blue arrow) - a configuration which, coupled with multiple additional jets, can conspire to give large values of α_T. The sum of the generator level $\not\!\!E_T$ and the p_T of the jet, equate to the p_T of the generator level jet (bold black arrow), indicating that the missing energy of the

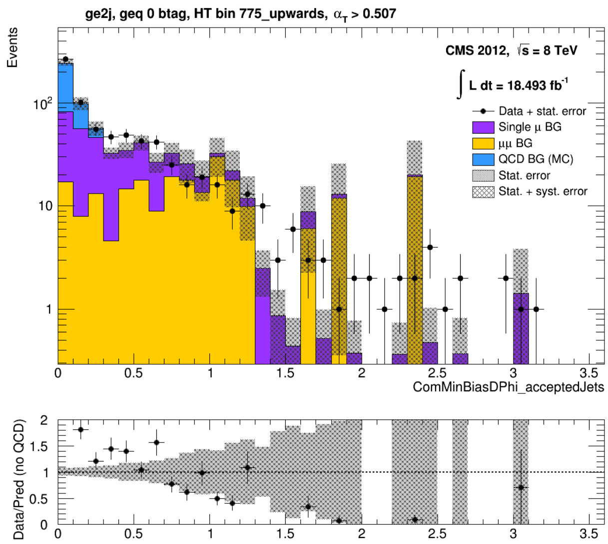

Fig. 7.9 Data (black points) against the EWK background prediction (stacked, yellow and purple) as a function of $\Delta\phi^*_{min}$. The expected yield from QCD MC (cyan) is stacked on top of the EWK prediction, but not included in the ratio plot. The plot represents the QCD control study region, with $n_{\mathrm{b}} \geq 0$, $n_{\mathrm{jet}} \geq 2$, $H_T > 775\ GeV$ and $\alpha_{\mathrm{T}} > 0.507$.

event comes almost entirely from the neutrinos in the decay of the jet. Furthermore, this implies the ratio $\not{H}_T/\not{E}_T$ to be near unity, therefore allowing events to also evade the $\not{H}_T/\not{E}_T < 1.25$ requirement of the signal region.

To better study events of this type a study region is defined, populated by the the single-object H_T trigger, `HLT_HT750`, which remained unprescaled throughout Run I. As opposed to a typical signal trigger, the lack of an α_{T} requirement allows events with lower values of α_{T} to be studied. The region is therefore defined by $H_T > 775$ GeV and $0.507 < \alpha_{\mathrm{T}} < 0.55$. Due to the intrinsic correlation of H_T and $\not{H}_T$ within the α_{T} variable (figure 6.2), this selection provides an effective $\not{H}_T$ requirement similar to that of the low H_T categories of the nominal analysis.

Jets containing a $\not{E}_T$ source appear as mismeasured and therefore populate a region of low $\Delta\phi^*$ (equation 7.8). Figure 7.9 shows the data compared to the EWK background prediction as a function of the $\Delta\phi^*_{min}$ value of each event. The disagreement observed at low $\Delta\phi^*_{min}$ is well accounted for by the yield from QCD MC. However, it should be noted that while simulated MC can provide a qualitative understanding of the QCD contamination, it should not be relied upon to determine a quantitative understanding of the phenomenon.

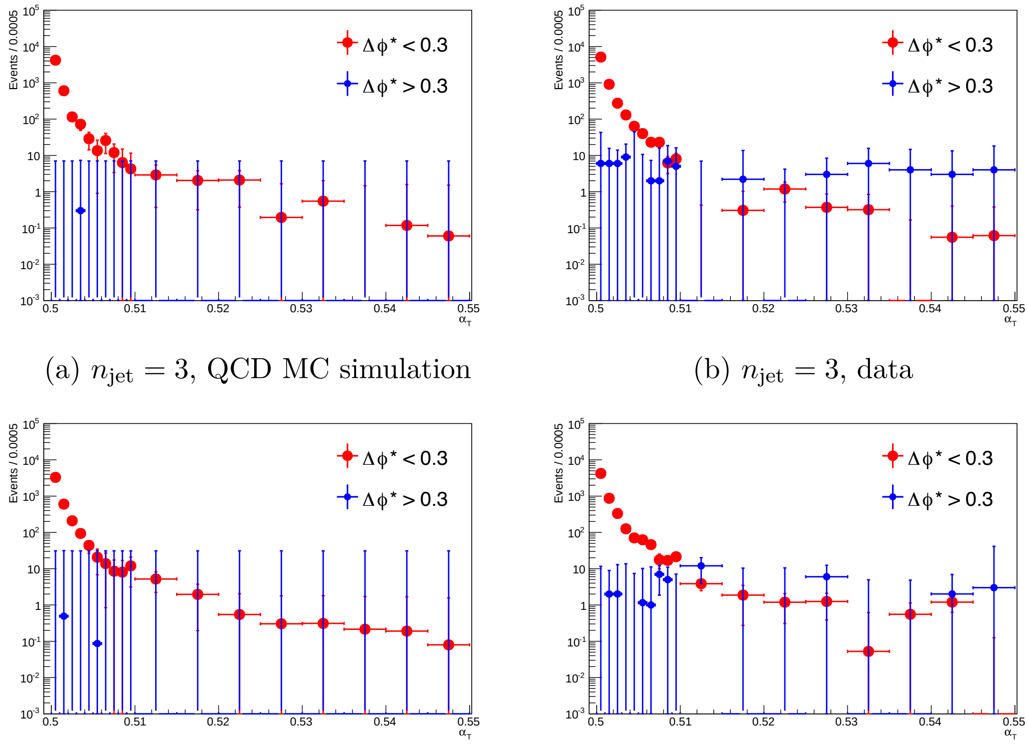

(a) $n_{\text{jet}} = 3$, QCD MC simulation (b) $n_{\text{jet}} = 3$, data

(c) $n_{\text{jet}} = 4$, QCD MC simulation (d) $n_{\text{jet}} = 4$, data

Fig. 7.10 The α_{T} distribution for events with no $\Delta\phi^*_{min}$ requirement (red circles) and with the $\Delta\phi^*_{min} > 0.3$ requirement (blue circles) as determined from QCD multijet simulation (left column) or data (right column) and the exclusive $n_{\text{jet}} = 3$ (top row) or $n_{\text{jet}} = 4$ (bottom row). Note that negligible QCD contamination is seen in the $n_{\text{jet}} = 2$ category and consequently is not shown here. The QCD control study region requirements have been applied, $H_T > 775$ GeV and $\alpha_{\text{T}} > 0.507$, with $n_{\text{b}} \geq 0$.

As motivated by figure 7.9, the residual QCD events appear to be well isolated in the region $\Delta\phi^*_{min} < 0.3$. The effect of applying this threshold in the QCD control study region is shown in figure 7.10. When considering simulation (figures 7.10a and 7.10c), the requirement of $\Delta\phi^*_{min} > 0.3$ removes all QCD events. However care must be taken when interpreting the same plots for data (figures 7.10b and 7.10d). To extract the expected QCD MJ contribution from data, observed event counts are corrected to subtract the expected contribution from EWK background processes, as estimated using the standard EWK background prediction method. Given this subtraction, the remaining number of events is expected to be compatible with zero within errors as opposed to exactly zero, as is seen in the data distributions. This supports the conclusion found in simulation that the heavy flavour QCD events are removed by the

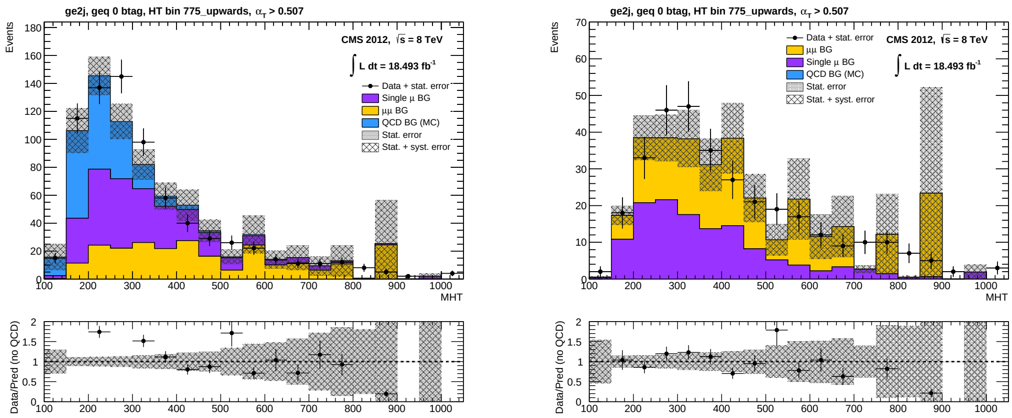

(a) $\Delta\phi^*_{min} < 0.3$ (b) $\Delta\phi^*_{min} > 0.3$

Fig. 7.11 Observations in data compared to the EWK background prediction as a function of the $\not{H}_T$ variable. An inclusive selection is made in the QCD study region, $H_T > 775$ GeV, $\alpha_{\rm T} > 0.507$, $n_{\rm jet} \geq 2$ and $n_{\rm b} \geq 0$. Plots are shown for both the QCD-enriched $\Delta\phi^*_{min} < 0.3$ and QCD-cleaned $\Delta\phi^*_{min} > 0.3$ regions. Yields from QCD MC (cyan) are shown stacked on the total EWK background prediction, but not included in the ratio.

application of the $\Delta\phi^*_{min} > 0.3$ requirement.

Figure 7.11 shows data observations compared to the EWK background prediction as a function of $\not{H}_T$ for the QCD study region, with both the $\Delta\phi^*_{min} < 0.3$ (figure 7.11a) and $\Delta\phi^*_{min} > 0.3$ (figure 7.11b) requirements applied. Following the removal of the low $\Delta\phi^*_{min}$ events, observations agree well with the EWK prediction. As a consequence of these studies, the analysis additionally requires that all events have $\Delta\phi^*_{min} > 0.3$ in the signal region.

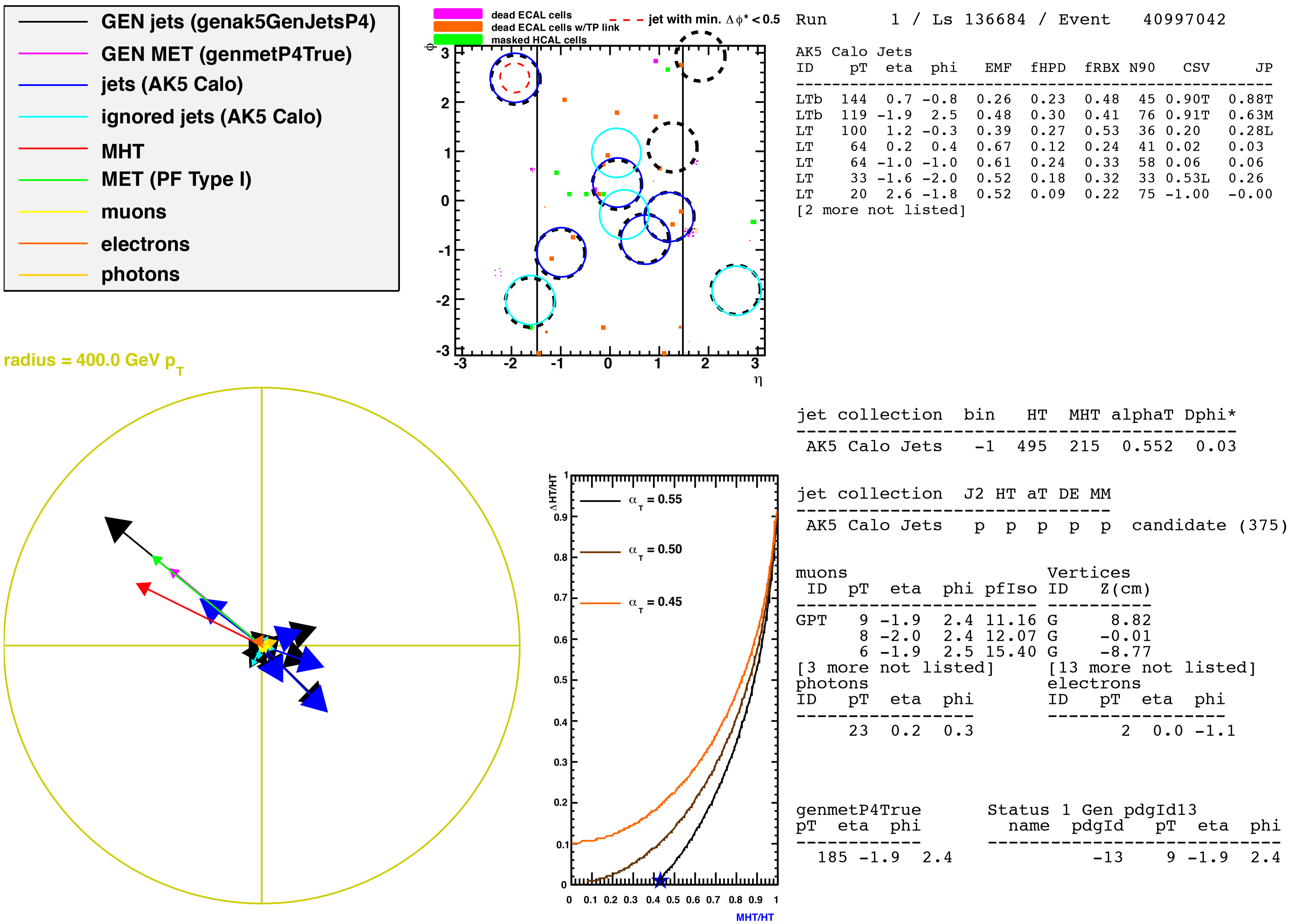

Fig. 7.12 An event display of a typical heavy flavour QCD event, with a jet decaying semi-leptonically with high-p_T neutrinos and therefore considerable generator-level $\not\!\!E_T$.

Chapter 8

Results

8.1 Likelihood Model

The likelihood is defined for each analysis category of n_{b} and n_{jet} as follows.

8.1.1 Hadronic Signal Region

Let n^i be the observed number of events following the full selection in the i^{th} of N bins of H_T. The likelihood is constructed as:

$$L_{hadronic} = \prod_i \mathrm{Pois}(n^i | b^i + s^i), \tag{8.1}$$

where b^i and s^i represent the expected number of background events from SM processes and the expected number of signal events in the bin i. Pois is the Poisson distribution:

$$f(k; \lambda) = \frac{1}{k!}\lambda^k e^{-\lambda}. \tag{8.2}$$

8.1.2 Electroweak Background Contribution

The background is considered to be entirely EWK in origin ($b^i = \mathrm{EWK}^i$), as QCD is made negligible, so can be de-constructed using the relative fraction of $Z \to \nu\bar{\nu}$ events, f_{Zinv} as:

$$\mathrm{Z}^i_{inv} = f_{\mathrm{Zinv}} \times \mathrm{EWK}^i, \tag{8.3}$$

$$\mathrm{ttW}^i = (1 - f_{\mathrm{Zinv}}) \times \mathrm{EWK}^i, \tag{8.4}$$

where EWK^i is number of expected events from the total EWK background, $\mathrm{Z}^i_{\mathrm{inv}}$ is the number of expected events from the $Z \to \nu\bar{\nu}$ contribution and ttW^i is the number of expect events from the W boson production and top quark decay contribution, all in the i^{th} bin. The variable f_{Zinv} is allowed to float between 0 and 1.

EWK backgrounds are predicted using sideband control samples and transfer factors (chapter 7). Let n^i_γ, n^i_μ and $n^i_{\mu\mu}$ be the observed event counts in the γ+jets, μ+jets and $\mu\mu$+jets control samples, respectively, with corresponding yields in MC: MC^i_γ, MC^i_μ, $MC^i_{\mu\mu}$. These are further separated into contributions from $Z \to \nu\bar{\nu}$, $MC_{\mathrm{Z_{inv}}}$, and ttW, $MC_{\mathrm{t\bar{t}+W}}$. Transfer factors are defined as the inverse as those of the analysis:

$$r^i_\gamma = \frac{MC^i_\gamma}{MC_{\mathrm{Z_{inv}}}}; \quad r^i_{\mu\mu} = \frac{MC^i_{\mu\mu}}{MC_{\mathrm{Z_{inv}}}}; \quad r^i_\mu = \frac{MC^i_\mu}{MC_{\mathrm{t\bar{t}+W}}}, \tag{8.5}$$

and so likelihoods are written as:

$$L_\gamma = \prod_i \mathrm{Pois}(n^i_\gamma | \rho^j_{\gamma Z} \cdot r^i_\gamma \cdot Z^i_{\mathrm{inv}}), \tag{8.6}$$

$$L_{\mu\mu} = \prod_i \mathrm{Pois}(n^i_{\mu\mu} | \rho^j_{\mu\mu Z} \cdot r^i_{\mu\mu} \cdot Z^i_{\mathrm{inv}}), \tag{8.7}$$

$$L_\mu = \prod_i \mathrm{Pois}(n^i_\mu | \rho^j_{\mu W} \cdot r^i_\mu \cdot ttW^i + s^i_\mu). \tag{8.8}$$

Both equations 8.6 and 8.7 are used to estimate the maximum likelihood value for Z^i_{inv}, alongside equation 8.8 for ttW^i, all considered simultaneously through the relationships defined in equations 8.3 and 8.4.

The terms $\rho^j_{\gamma Z}$, $\rho^j_{\mu\mu Z}$ and $\rho^j_{\mu W}$ are correction factors accommodating the systematic uncertainties associated with the control sample based background predictions. The relative uncertainties are derived in section 7.3 and represented by the terms $\sigma^j_{\gamma Z}$, $\sigma^j_{\mu\mu Z}$ and $\sigma^j_{\mu W}$, their values summarised in table 7.7. Systematics enter the total likelihood as:

$$L_{\gamma\ \mathrm{syst.}} = \prod_j \mathrm{Logn}(1.0 | \rho^j_{\gamma Z}, \sigma^j_{\gamma Z}), \tag{8.9}$$

$$L_{\mu\mu\ \mathrm{syst.}} = \prod_j \mathrm{Logn}(1.0 | \rho^j_{\mu\mu Z}, \sigma^j_{\mu\mu Z}), \tag{8.10}$$

$$L_{\mu\ \mathrm{syst.}} = \prod_j \mathrm{Logn}(1.0 | \rho^j_{\mu W}, \sigma^j_{\mu W}), \tag{8.11}$$

where Logn is the log-normal distribution (as recommended by [76]):

$$\mathrm{Logn}(x|\mu,\sigma) = \frac{1}{x\sqrt{2\pi}\mathrm{ln}k} exp\left(- \frac{\mathrm{ln}^2\left(\frac{x}{\mu}\right)}{2\mathrm{ln}^2 k}\right); k = 1 + \sigma. \tag{8.12}$$

These terms are combined as:

$$L_{EWK \text{ syst.}} = L_{\gamma \text{ syst.}} \times L_{\mu\mu \text{ syst.}} \times L_{\mu \text{ syst.}}. \tag{8.13}$$

For $n_{\mathrm{b}} \geq 2$ categories, the μ+jets control sample is used to predict $Z \rightarrow \nu\bar{\nu}$ and ttW combined, giving:

$$r'^{i}_{\mu} = \frac{MC^i_\mu}{MC^i_{\mathrm{t\bar{t}+W+Z_{inv}}}}; \tag{8.14}$$

$$L_\mu = \prod_i \mathrm{Pois}(n^i_\mu | \rho^j_{\mu W} \cdot r'^{i}_{\mu} \cdot EWK^i + s^i_\mu). \tag{8.15}$$

Terms corresponding to the $\mu\mu$+jets and γ+jets samples are subsequently dropped.

8.1.3 Signal Contribution

Let x be the cross section of the signal model under test, which can be varied according to a multiplicative factor f (a.k.a. the "mu-factor"), and l be the luminosity of the relevant collected data sample. ϵ^i_{had} and ϵ^i_μ are the signal acceptances of the hadronic and muon selections, respectively, for the given signal model. Finally, let δ be the relative systematic uncertainty on that signal acceptance, and ρ_{sig} be the corrective factor to the signal yield floated to accommodate this uncertainty. Therefore the yield of signal events for the hadronic sample, s^i, and the yield of signal events in the muon sample (i.e. "signal contamination"), s^i_μ, can be written as:

$$s^i = f\rho_{sig} x l \epsilon_{had}, \tag{8.16}$$

$$s^i_\mu = f\rho_{sig} x l \epsilon_\mu. \tag{8.17}$$

Furthermore, the signal systematic contribution to the likelihood is included as the term:

$$L_{signal} = \mathrm{Logn}(1.0|\rho_{sig}, \delta). \tag{8.18}$$

8.1.4 Total Likelihood

For a given analysis category k (n_{b}, n_{jet}), the total likelihood is constructed as:

$$L^{k}_{total} = L^{k}_{hadronic} \times L^{k}_{\mu} \times L^{k}_{\gamma} \times L^{k}_{\mu\mu} \times L^{k}_{\mathrm{EWK\ syst.}}. \tag{8.19}$$

The number of nuisance parameters varies between different analysis categories, dependent on the number of H_T bins and control samples, as summarised in table 8.1.

Table 8.1 Summary of likelihood nuisance parameters.

Description	Categories	Nuisance Parameters
11 H_T bins, $(\mu, \mu\mu, \gamma)$	$2 \leq n_{\mathrm{jet}} \leq 3/n_{\mathrm{jet}} \geq 4$, $n_{\mathrm{b}} = 0, 1$	$\{EWK^i, f_{\mathrm{Zinv}}\}^{10}_{i=0}, \{\rho^j_{\gamma Z}\}^6_{i=3}, \{\rho^j_{\mu\mu Z}, \rho^j_{\mu W}\}^6_{i=0}$
8 H_T bins, (μ)	$2 \leq n_{\mathrm{jet}} \leq 3/n_{\mathrm{jet}} \geq 4$, $n_{\mathrm{b}} = 2, 3, \geq 4$	$\{EWK^i, f_{\mathrm{Zinv}}\}^{8}_{i=0}, \{\rho^j_{\mu WZ}\}^6_{i=0}$
3 H_T bins, (μ)	$2 \leq n_{\mathrm{jet}} \leq 3/n_{\mathrm{jet}} \geq 4$, $n_{\mathrm{b}} = 2, 3, \geq 4$	$\{EWK^i\}^{3}_{i=0}, \{\rho^j_{\mu WZ}\}_{i=0}$

When considering signal an additional term is introduced:

$$L = L_{signal} \times \prod_{k} L^{k}_{total}. \tag{8.20}$$

8.2 Fit Results

The likelihood model described in section 8.1 is used to relate the observations in the signal and control samples, accommodate the calculated background systematic uncertainties, and allow for the presence of any potential signal. In order to test the compatibility with a Standard Model only hypothesis, signal contribution is set to zero and the likelihood is maximized over all parameters using RooFit [77] and Minuit [78], for each analysis category of n_{b} and n_{jet}.

Uncertainties are determined by performing a number of pseudo-experiments for each (n_{b}, n_{jet}) category and H_T bin, with the fit yields being entered into a histogram, appropriate quantiles taken, using their difference from the maximum likelihood (ML) value taken as the fit uncertainty value.

Two different procedures are used to determine fits to observations, as described in the following sections.

8.2.1 Fit without Signal region

An “a priori” fit is made by considering only yields from the control samples, and not data observations in the hadronic signal region. The results of this fit are shown in figs. 8.2 to 8.3 and 8.5 to 8.9 and summarised in table 8.2.

8.2.2 Fit with Signal region

An “a posteriori” fit is made by considering every region, including the hadronic signal region observation in data, and is shown in figs. 8.2 to 8.3 and 8.5 to 8.9 and summarised in table 8.3.

Table 8.2 Summary of the “a priori” fit.

			H_T (GeV)										
$n_{\rm jet}$	$n_{\rm b}$		200–275	275–325	325–375	375–475	475–575	575–675	675–775	775–875	875–975	975–1075	1075–∞
2–3	0	SM	12412^{+369}_{-412}	5535^{+338}_{-234}	3331^{+126}_{-167}	2400^{+122}_{-94}	663^{+34}_{-26}	225^{+21}_{-17}	$68.5^{+6.9}_{-6.7}$	$26.5^{+3.9}_{-3.0}$	$10.3^{+1.9}_{-2.1}$	$5.1^{+1.0}_{-1.1}$	$4.5^{+0.9}_{-0.9}$
2–3	0	Data	13090	5331	3354	2326	671	206	76	29	10	9	2
2–3	1	SM	1669^{+65}_{-67}	853^{+50}_{-46}	525^{+37}_{-24}	391^{+23}_{-21}	$94.3^{+6.0}_{-5.6}$	$24.5^{+2.5}_{-3.6}$	$9.0^{+1.2}_{-1.4}$	$2.8^{+0.6}_{-0.8}$	$2.5^{+0.8}_{-0.9}$	$0.3^{+0.2}_{-0.1}$	$0.2^{+0.1}_{-0.1}$
2–3	1	Data	1733	833	527	356	90	31	6	4	1	0	1
2–3	2	SM	187^{+7}_{-8}	118^{+7}_{-7}	$98.7^{+7.1}_{-7.0}$	$61.3^{+5.9}_{-5.5}$	$12.3^{+1.7}_{-1.0}$	$2.8^{+0.5}_{-0.6}$	$0.7^{+0.2}_{-0.2}$	$0.2^{+0.1}_{-0.1}$	$0.1^{+0.0}_{-0.0}$		
2–3	2	Data	172	116	101	55	16	9	0	0	0		
≥ 4	0	SM	108^{+10}_{-12}	497^{+34}_{-36}	403^{+36}_{-33}	327^{+25}_{-22}	193^{+14}_{-13}	$94.6^{+13.0}_{-10.7}$	$40.3^{+5.9}_{-4.4}$	$14.5^{+3.5}_{-2.4}$	$7.1^{+1.7}_{-1.4}$	$3.2^{+0.7}_{-1.0}$	$2.9^{+0.7}_{-0.5}$
≥ 4	0	Data	99	568	408	336	211	117	38	13	9	4	6
≥ 4	1	SM	$39.2^{+3.0}_{-3.5}$	215^{+12}_{-16}	208^{+24}_{-22}	150^{+15}_{-11}	$75.8^{+7.8}_{-6.6}$	$28.6^{+3.8}_{-3.7}$	$10.3^{+2.1}_{-1.4}$	$5.1^{+1.3}_{-0.9}$	$2.0^{+0.7}_{-0.5}$	$0.8^{+0.4}_{-0.3}$	$0.9^{+0.6}_{-0.4}$
≥ 4	1	Data	38	195	210	159	83	33	7	10	4	1	1
≥ 4	2	SM	$12.3^{+1.0}_{-1.0}$	$76.7^{+5.6}_{-5.2}$	$92.6^{+11.0}_{-9.3}$	$63.0^{+7.8}_{-5.7}$	$34.0^{+3.6}_{-3.4}$	$10.1^{+2.6}_{-1.8}$	$3.4^{+0.9}_{-0.6}$	$1.0^{+0.2}_{-0.2}$	$0.7^{+0.1}_{-0.2}$		
≥ 4	2	Data	16	81	88	64	43	14	5	1	1		
≥ 4	3	SM	$1.1^{+0.2}_{-0.1}$	$8.2^{+0.6}_{-0.9}$	$11.1^{+2.0}_{-1.6}$	$7.4^{+1.1}_{-1.0}$	$4.0^{+0.5}_{-0.6}$	$1.1^{+0.3}_{-0.3}$	$0.4^{+0.2}_{-0.1}$	$0.1^{+0.1}_{-0.0}$	$0.1^{+0.0}_{-0.0}$		
≥ 4	3	Data	0	7	5	5	6	1	1	0	0		
≥ 4	≥ 4	SM	$0.0^{+0.0}_{--0.0}$	$0.2^{+0.1}_{-0.1}$	$0.5^{+0.3}_{-0.3}$	$0.3^{+0.2}_{-0.2}$							
≥ 4	≥ 4	Data	0	0	0	2							

Table 8.3 Summary of the “a posteriori” fit.

			H_T (GeV)										
n_{jet}	n_{b}		200–275	275–325	325–375	375–475	475–575	575–675	675–775	775–875	875–975	975–1075	1075–∞
2–3	0	SM	13034^{+89}_{-117}	5348^{+85}_{-67}	3351^{+56}_{-50}	2351^{+38}_{-45}	655^{+14}_{-11}	218^{+12}_{-17}	$68.5^{+4.9}_{-4.8}$	$27.2^{+3.0}_{-3.0}$	$10.4^{+1.5}_{-1.6}$	$5.6^{+1.0}_{-1.0}$	$4.3^{+0.7}_{-1.0}$
2–3	0	Data	13090	5331	3354	2326	671	206	76	29	10	9	2
2–3	1	SM	1711^{+37}_{-33}	839^{+21}_{-25}	526^{+20}_{-17}	372^{+12}_{-14}	$90.6^{+5.1}_{-4.6}$	$25.8^{+2.9}_{-2.6}$	$8.7^{+0.8}_{-1.4}$	$3.0^{+0.7}_{-0.6}$	$2.2^{+0.8}_{-0.6}$	$0.3^{+0.2}_{-0.1}$	$0.2^{+0.1}_{-0.2}$
2–3	1	Data	1733	833	527	356	90	31	6	4	1	0	1
2–3	2	SM	184^{+5}_{-7}	117^{+7}_{-5}	$99.4^{+5.4}_{-4.6}$	$60.2^{+3.5}_{-3.8}$	$12.4^{+1.2}_{-1.0}$	$3.3^{+0.6}_{-0.5}$	$0.7^{+0.2}_{-0.2}$	$0.2^{+0.1}_{-0.1}$	$0.1^{+0.0}_{-0.0}$		
2–3	2	Data	172	116	101	55	16	9	0	0	0		
≥ 4	0	SM	104^{+6}_{-8}	544^{+21}_{-18}	407^{+18}_{-18}	337^{+15}_{-10}	202^{+10}_{-8}	105^{+9}_{-7}	$42.5^{+4.5}_{-3.3}$	$14.3^{+1.7}_{-2.5}$	$7.5^{+1.4}_{-1.5}$	$3.5^{+0.8}_{-0.8}$	$3.4^{+1.0}_{-0.7}$
≥ 4	0	Data	99	568	408	336	211	117	38	13	9	4	6
≥ 4	1	SM	$38.9^{+2.2}_{-3.7}$	206^{+12}_{-10}	209^{+13}_{-10}	157^{+9}_{-9}	$79.3^{+5.2}_{-4.7}$	$29.4^{+3.8}_{-2.2}$	$9.9^{+1.9}_{-1.3}$	$6.2^{+1.2}_{-1.1}$	$2.3^{+0.7}_{-0.7}$	$0.9^{+0.3}_{-0.3}$	$0.9^{+0.3}_{-0.4}$
≥ 4	1	Data	38	195	210	159	83	33	7	10	4	1	1
≥ 4	2	SM	$12.5^{+1.0}_{-1.0}$	$77.8^{+4.7}_{-4.6}$	$90.2^{+9.0}_{-6.5}$	$66.1^{+4.6}_{-4.8}$	$36.3^{+3.4}_{-2.9}$	$11.4^{+1.8}_{-1.9}$	$3.9^{+0.8}_{-0.7}$	$1.0^{+0.2}_{-0.3}$	$0.7^{+0.1}_{-0.2}$		
≥ 4	2	Data	16	81	88	64	43	14	5	1	1		
≥ 4	3	SM	$1.1^{+0.2}_{-0.2}$	$8.1^{+0.9}_{-0.9}$	$9.9^{+1.5}_{-1.3}$	$7.2^{+0.9}_{-0.7}$	$4.1^{+0.6}_{-0.6}$	$1.1^{+0.3}_{-0.3}$	$0.4^{+0.1}_{-0.1}$	$0.1^{+0.1}_{-0.0}$	$0.1^{+0.0}_{-0.0}$		
≥ 4	3	Data	0	7	5	5	6	1	1	0	0		
≥ 4	≥ 4	SM	$0.0^{+0.0}_{--0.0}$	$0.1^{+0.1}_{-0.1}$	$0.4^{+0.2}_{-0.3}$	$0.4^{+0.2}_{-0.2}$							
≥ 4	≥ 4	Data	0	0	0	2							

8.2.3 Pulls and p-values

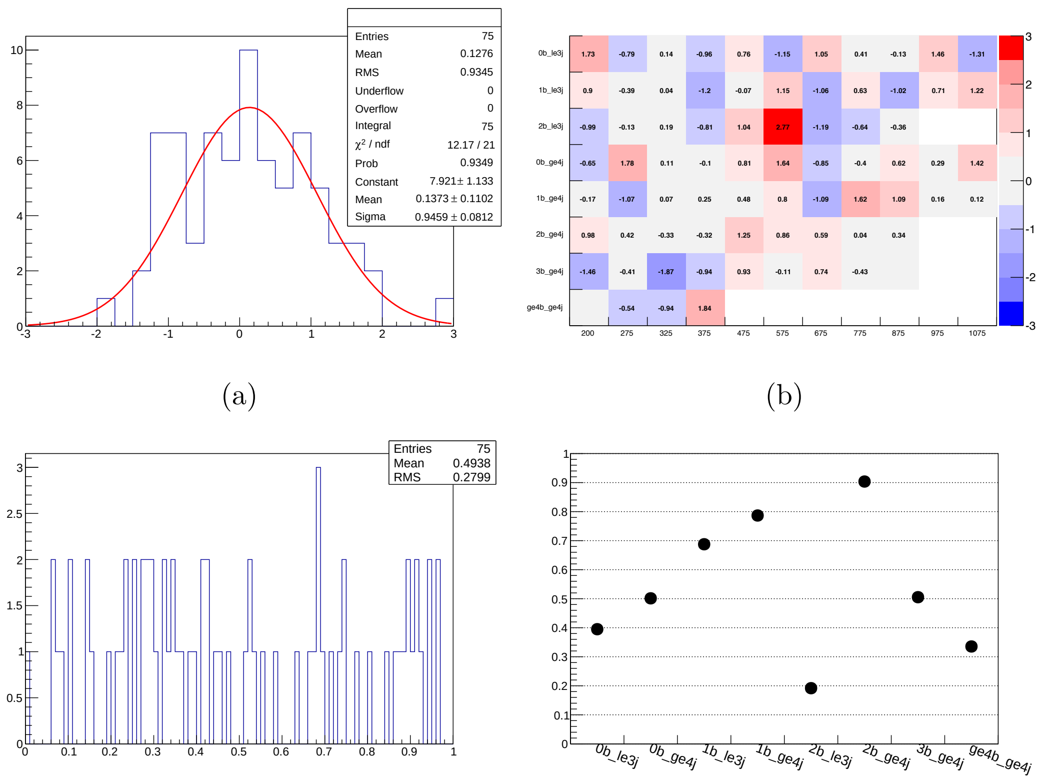

(a) (b)

(c) (d)

Fig. 8.1 Pulls for each analysis bin shown as a 1D distribution (figure 8.1a) and as a function of the H_T bin and analysis category (n_{jet}, n_{b}) (figure 8.1b). P-values for every analysis bin shown as a 1D distribution (figure 8.1c) and for each analysis category, for an inclusive H_T range (figure 8.1d).

Pulls and p-values are determined using a profile-likelihood method and are summarised for various different analysis categories and individual H_T bins in the plots shown in figure 8.1.

The 1D distribution of the pulls is shown in figure 8.1a, with a Gaussian fit (red) indicating good Gaussian behaviour, with mean and sigma values statistically significant with 0 and 1, respectively. Furthermore, the distribution of these pulls as a function of the H_T bin and the analysis category (n_{b}, n_{jet}) is shown in figure 8.1b to be randomly distributed, with no apparent pattern to a given region.

The distribution of p-values for every bin of H_T and analysis category can be seen in figure 8.1c to be uniformly distributed between 0 and 1. The same information is shown in figure 8.1d when a single p-value is calculated for an entire H_T range, for each analysis category, where the lowest value is 0.19.

These tests indicate no significant excesses, and that all observations are compatible with statistical fluctuations.

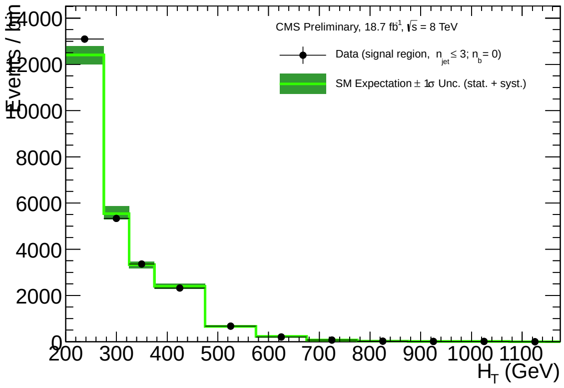

(a) Hadronic sample (linear scale)

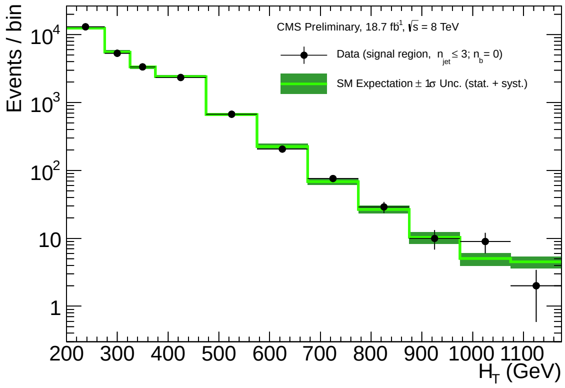

(b) Hadronic sample (logarithmic scale)

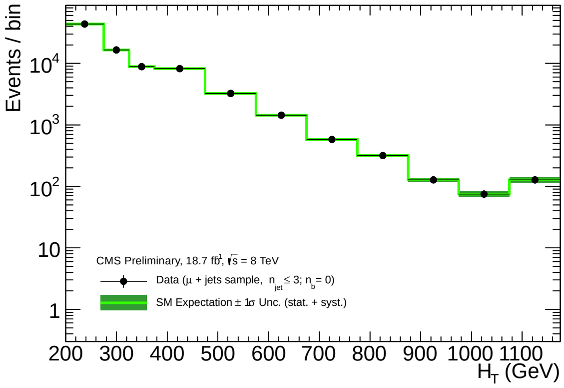

(c) μ+jets sample

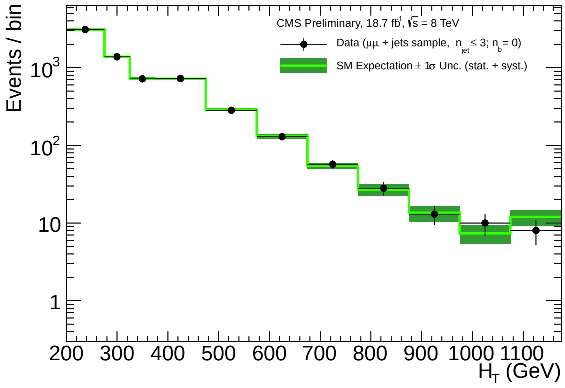

(d) $\mu\mu$+jets sample

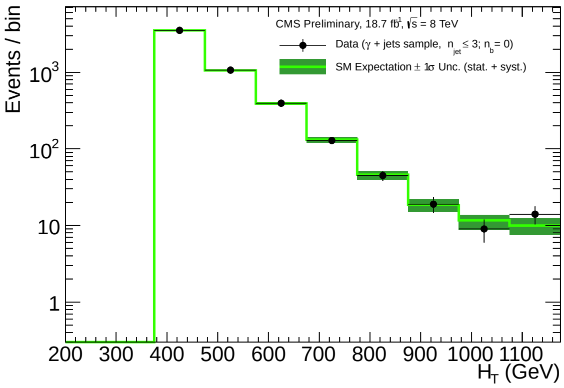

(e) γ+jets sample

Fig. 8.2 Observations in data for the signal and control regions of the analysis, compared to the result of the full likelihood model simultaneous fit, when the hadronic data observations are not considered. The plots shown are for the $2 \leq n_{\mathrm{jet}} \leq 3$, $n_{\mathrm{b}} = 0$ analysis category.

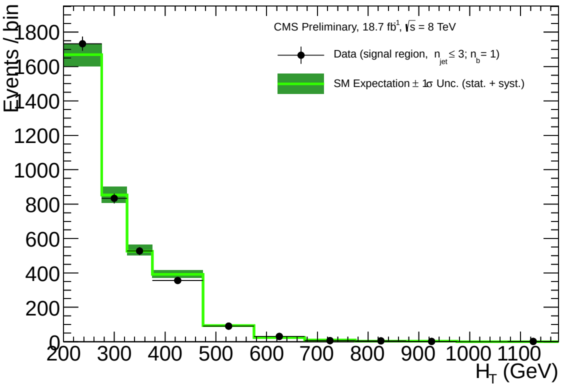

(a) Hadronic sample (linear scale)

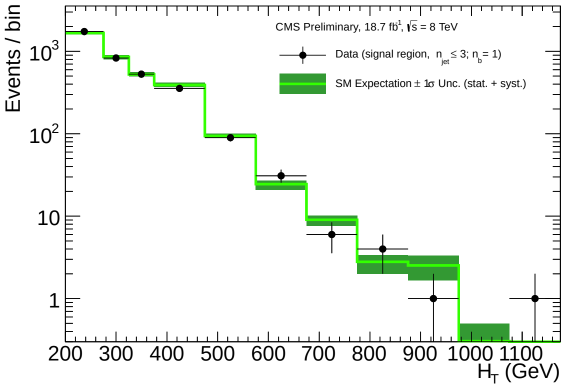

(b) Hadronic sample (logarithmic scale)

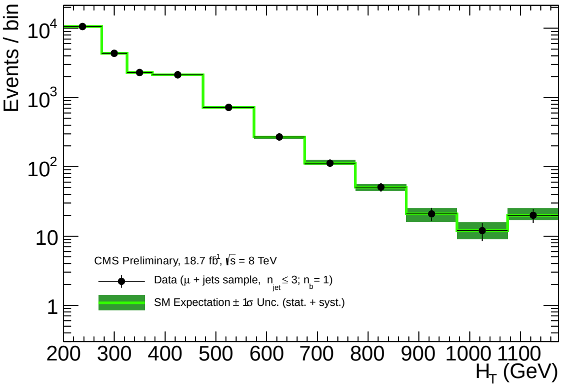

(c) μ+jets sample

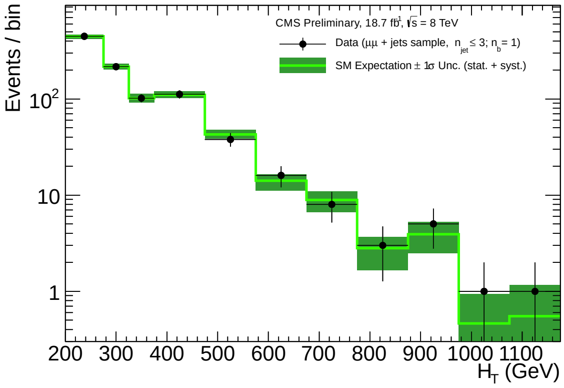

(d) $\mu\mu$+jets sample

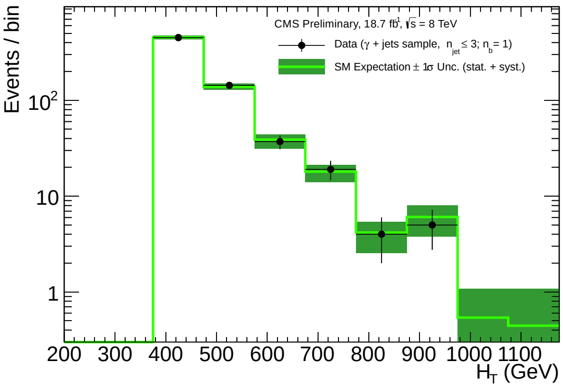

(e) γ+jets sample

Fig. 8.3 Observations in data for the signal and control regions of the analysis, compared to the result of the full likelihood model simultaneous fit, when the hadronic data observations are not considered. The plots shown are for the $2 \leq n_{\mathrm{jet}} \leq 3$, $n_{\mathrm{b}} = 1$ analysis category.

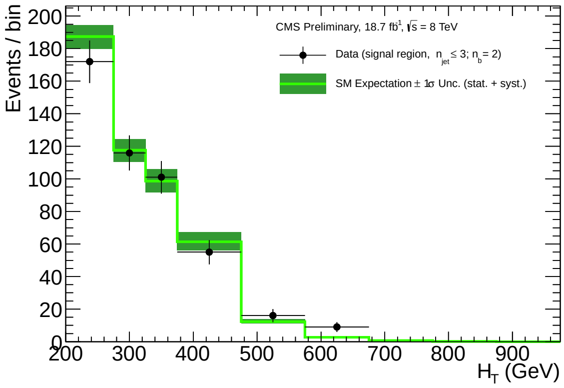

(a) Hadronic sample (linear scale)

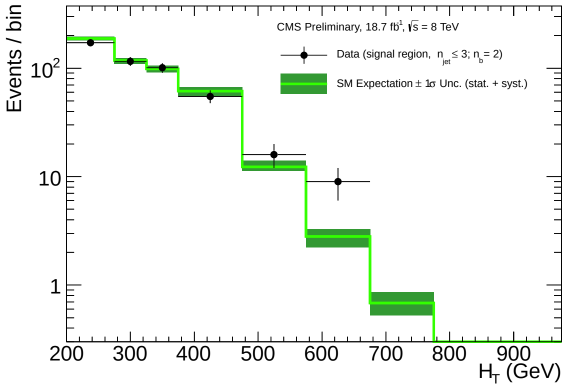

(b) Hadronic sample (logarithmic scale)

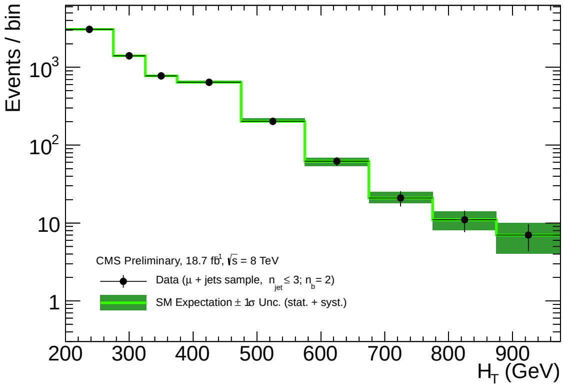

(c) μ+jets sample

Fig. 8.4 Observations in data for the signal and control regions of the analysis, compared to the result of the full likelihood model simultaneous fit, when the hadronic data observations are not considered. The plots shown are for the $2 \leq n_{\mathrm{jet}} \leq 3$, $n_{\mathrm{b}} = 2$ analysis category.

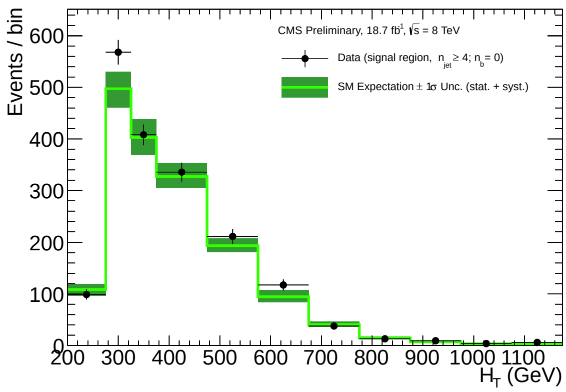

(a) Hadronic sample (linear scale)

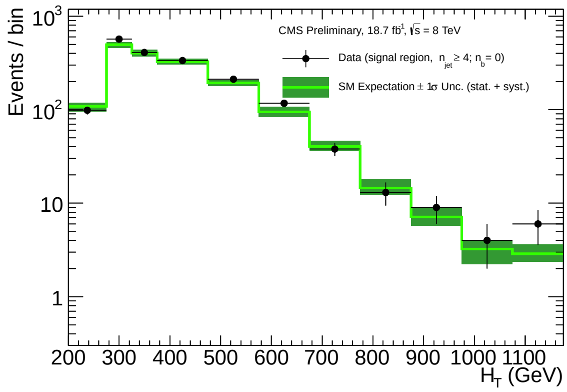

(b) Hadronic sample (logarithmic scale)

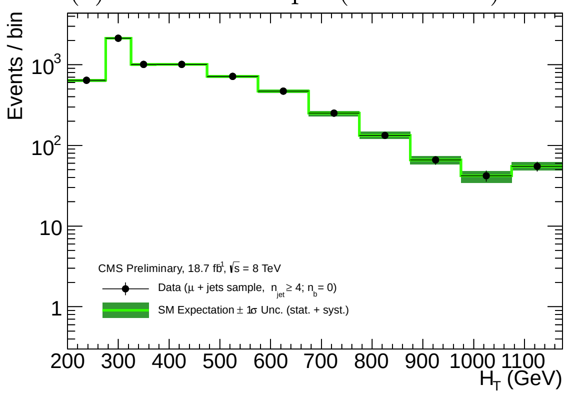

(c) μ+jets sample

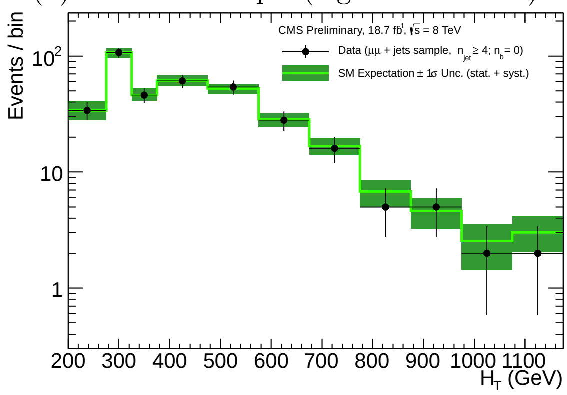

(d) $\mu\mu$+jets sample

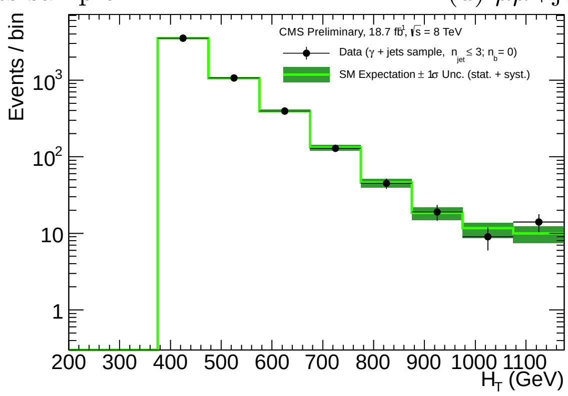

(e) γ+jets sample

Fig. 8.5 Observations in data for the signal and control regions of the analysis, compared to the result of the full likelihood model simultaneous fit, when the hadronic data observations are not considered. The plots shown are for the $n_{\mathrm{jet}} \geq 4$, $n_{\mathrm{b}} = 0$ analysis category.

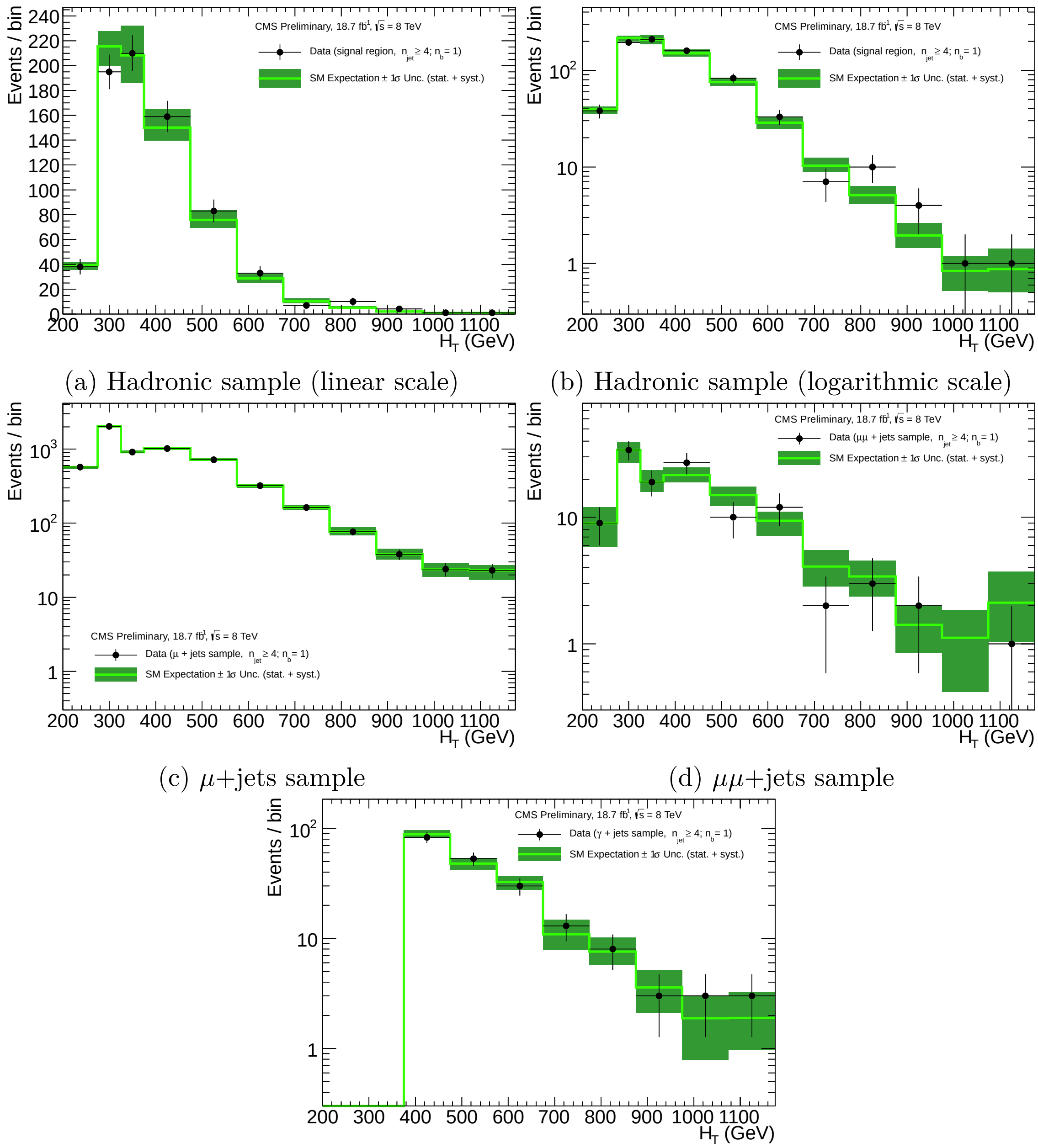

(a) Hadronic sample (linear scale)

(b) Hadronic sample (logarithmic scale)

(c) μ+jets sample

(d) $\mu\mu$+jets sample

(e) γ+jets sample

Fig. 8.6 Observations in data for the signal and control regions of the analysis, compared to the result of the full likelihood model simultaneous fit, when the hadronic data observations are not considered. The plots shown are for the $n_{\rm jet} \geq 4$, $n_{\rm b} = 1$ analysis category.

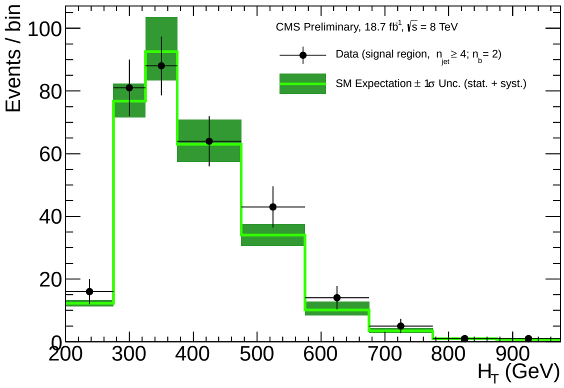

(a) Hadronic sample (linear scale)

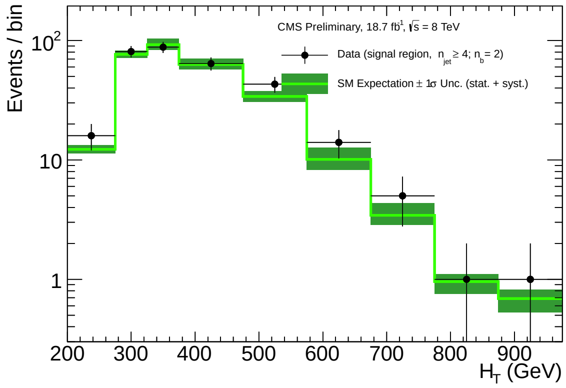

(b) Hadronic sample (logarithmic scale)

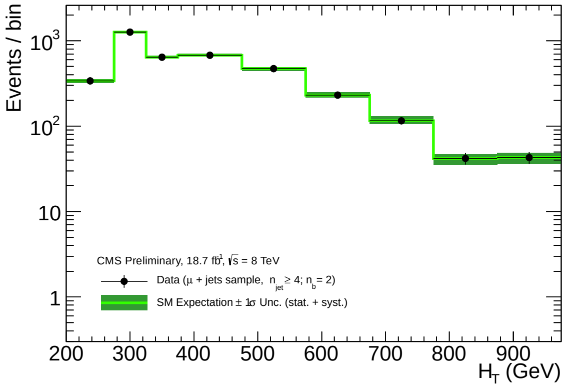

(c) μ+jets sample

Fig. 8.7 Observations in data for the signal and control regions of the analysis, compared to the result of the full likelihood model simultaneous fit, when the hadronic data observations are not considered. The plots shown are for the $n_{\text{jet}} \geq 4$, $n_{\text{b}} = 2$ analysis category.

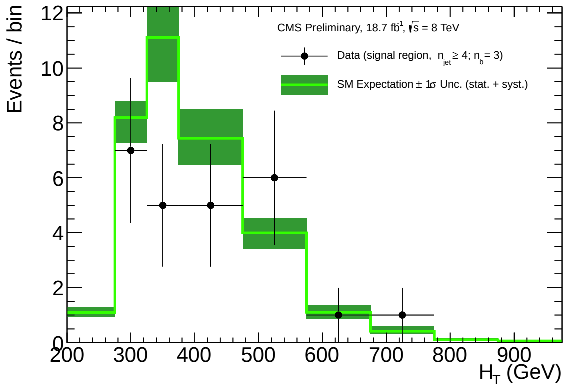

(a) Hadronic sample (linear scale)

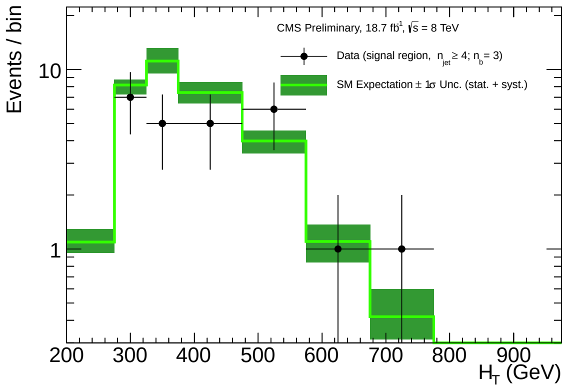

(b) Hadronic sample (logarithmic scale)

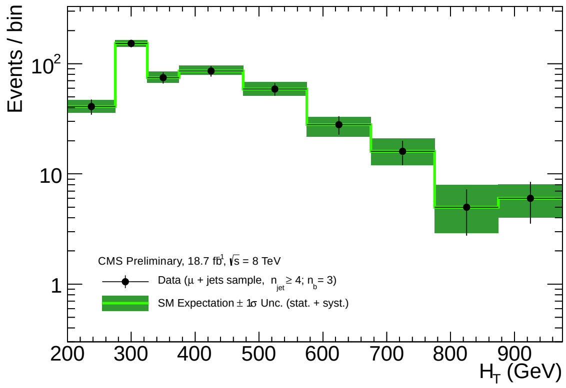

(c) μ+jets sample

Fig. 8.8 Observations in data for the signal and control regions of the analysis, compared to the result of the full likelihood model simultaneous fit, when the hadronic data observations are not considered. The plots shown are for the $n_{\rm jet} \geq 4$, $n_{\rm b} = 3$ analysis category.

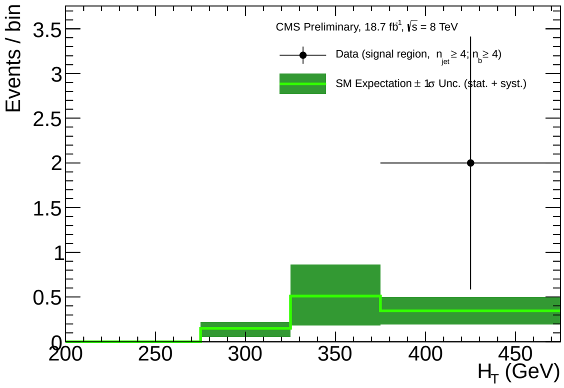

(a) Hadronic sample (linear scale)

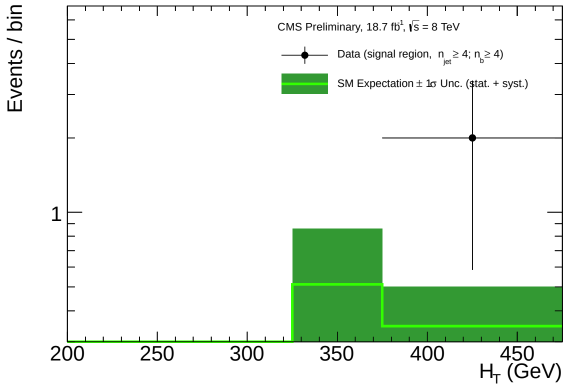

(b) Hadronic sample (logarithmic scale)

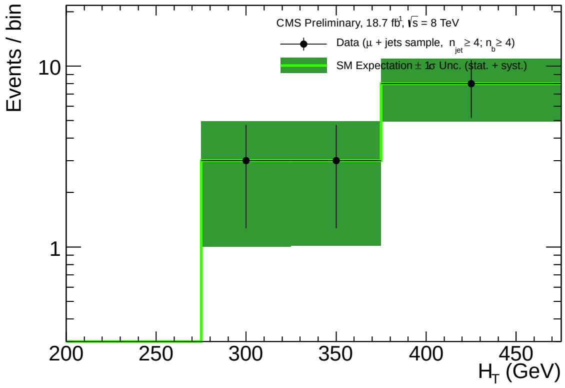

(c) μ+jets sample

Fig. 8.9 Observations in data for the signal and control regions of the analysis, compared to the result of the full likelihood model simultaneous fit, when the hadronic data observations are not considered. The plots shown are for the $n_{\text{jet}} \geq 4$, $n_{\text{b}} \geq 4$ analysis category.

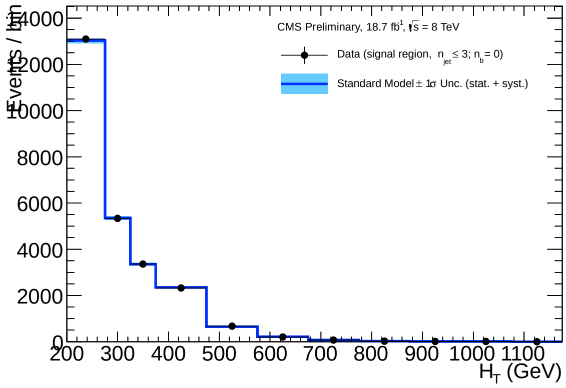

(a) Hadronic sample (linear scale)

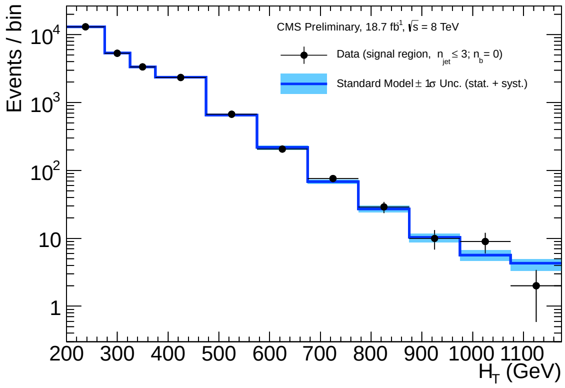

(b) Hadronic sample (logarithmic scale)

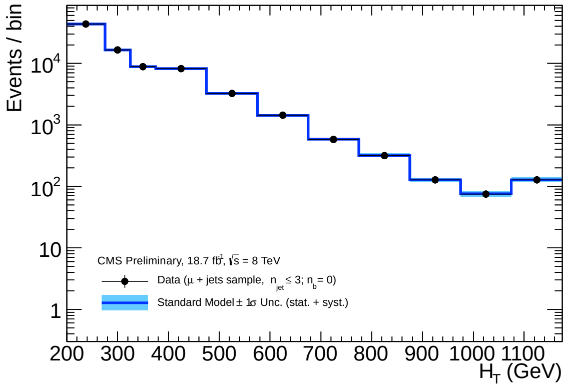

(c) μ+jets sample

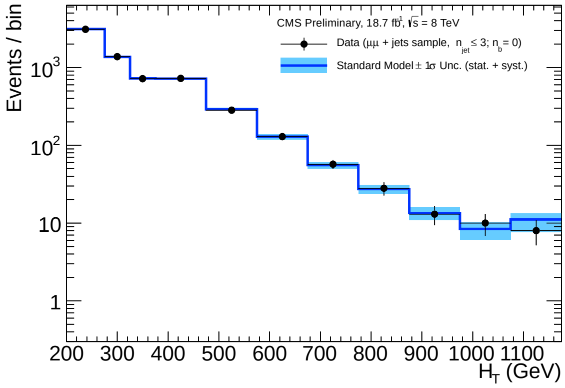

(d) $\mu\mu$+jets sample

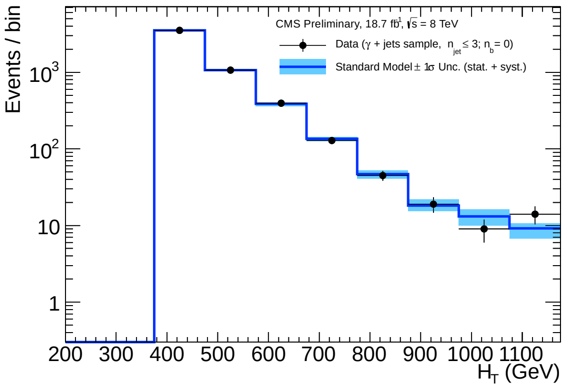

(e) γ+jets sample

Fig. 8.10 Observations in data for the signal and control regions of the analysis, compared to the result of the full likelihood model simultaneous fit. The plots shown are for the $2 \leq n_{\mathrm{jet}} \leq 3$, $n_{\mathrm{b}} = 0$ analysis category.

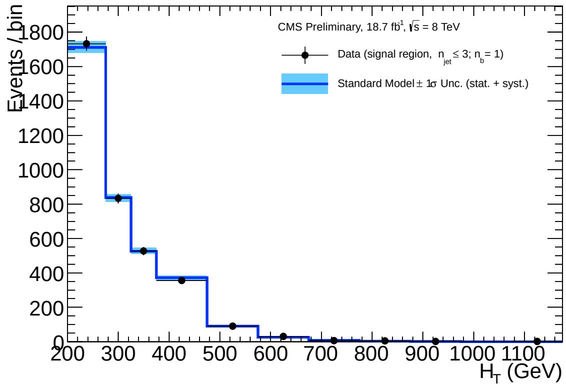

(a) Hadronic sample (linear scale)

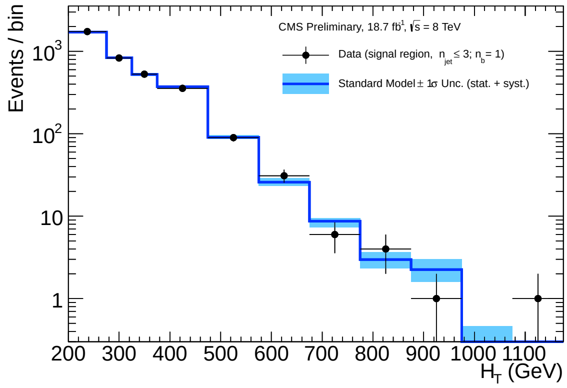

(b) Hadronic sample (logarithmic scale)

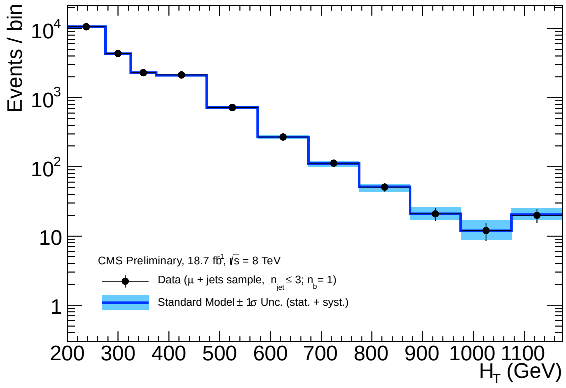

(c) μ+jets sample

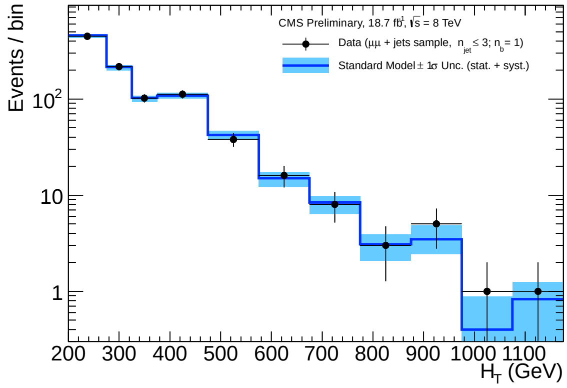

(d) $\mu\mu$+jets sample

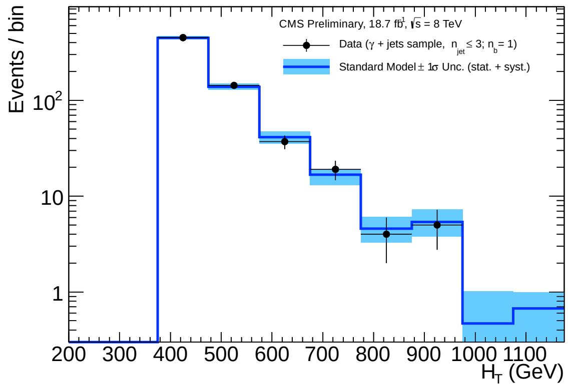

(e) γ+jets sample

Fig. 8.11 Observations in data for the signal and control regions of the analysis, compared to the result of the full likelihood model simultaneous fit. The plots shown are for the $2 \leq n_{\mathrm{jet}} \leq 3$, $n_{\mathrm{b}} = 1$ analysis category.

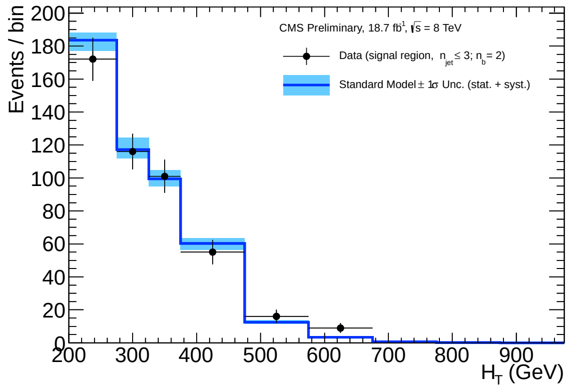

(a) Hadronic sample (linear scale)

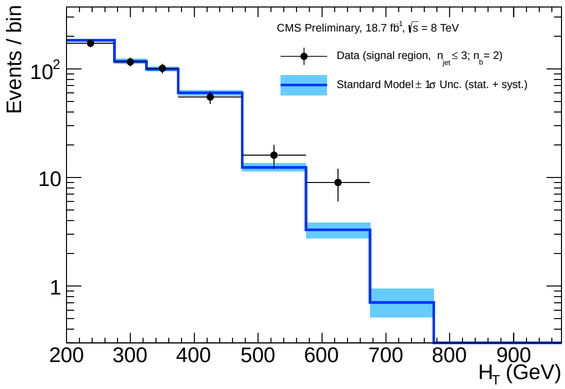

(b) Hadronic sample (logarithmic scale)

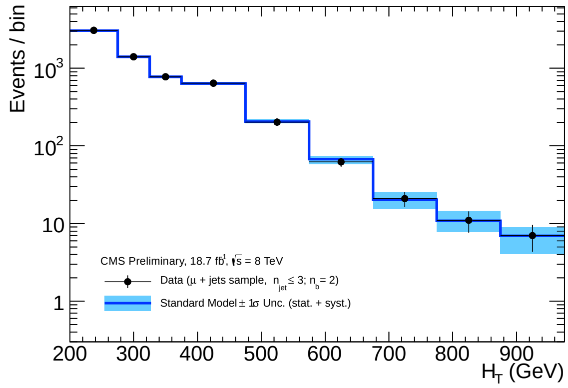

(c) μ+jets sample

Fig. 8.12 Observations in data for the signal and control regions of the analysis, compared to the result of the full likelihood model simultaneous fit. The plots shown are for the $2 \leq n_{\mathrm{jet}} \leq 3$, $n_{\mathrm{b}} = 2$ analysis category.

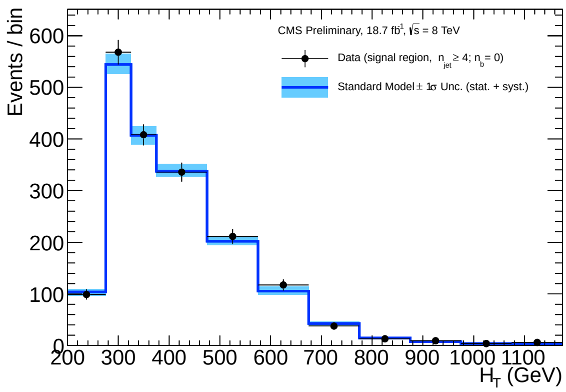

(a) Hadronic sample (linear scale)

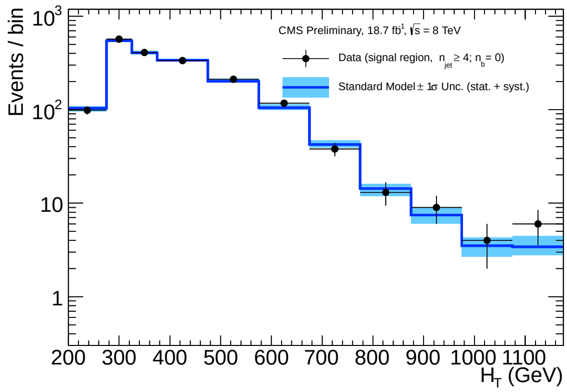

(b) Hadronic sample (logarithmic scale)

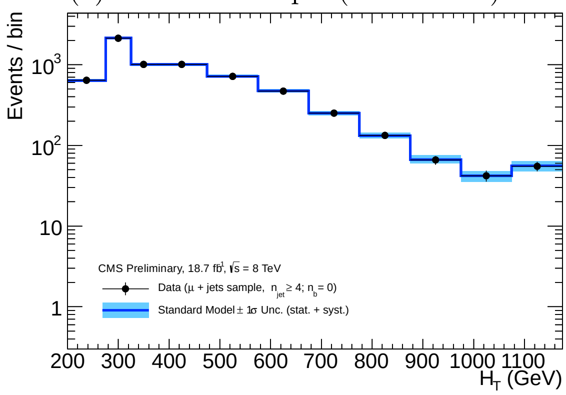

(c) μ+jets sample

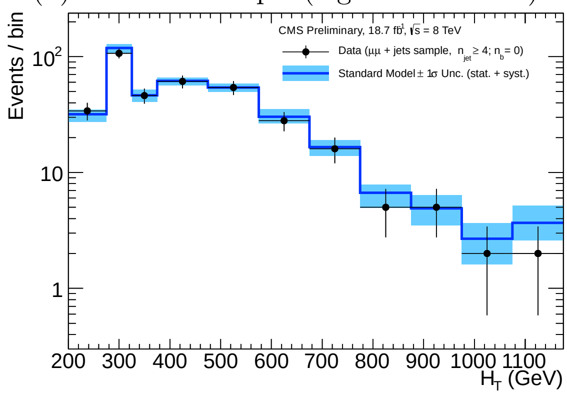

(d) $\mu\mu$+jets sample

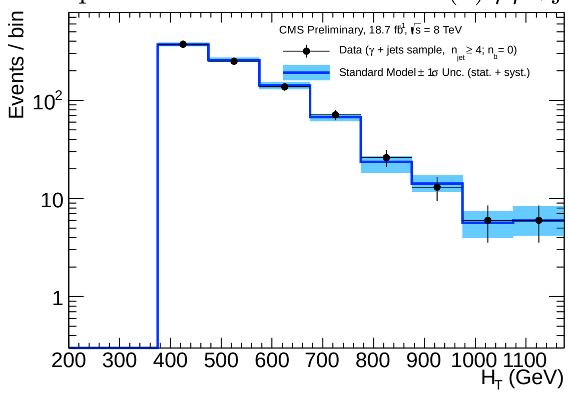

(e) γ+jets sample

Fig. 8.13 Observations in data for the signal and control regions of the analysis, compared to the result of the full likelihood model simultaneous fit. The plots shown are for the $n_{\text{jet}} \geq 4$, $n_{\text{b}} = 0$ analysis category.

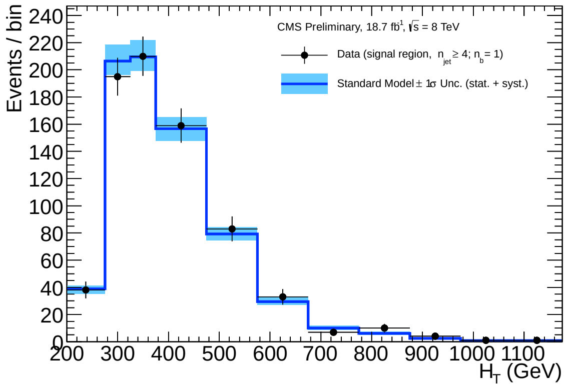

(a) Hadronic sample (linear scale)

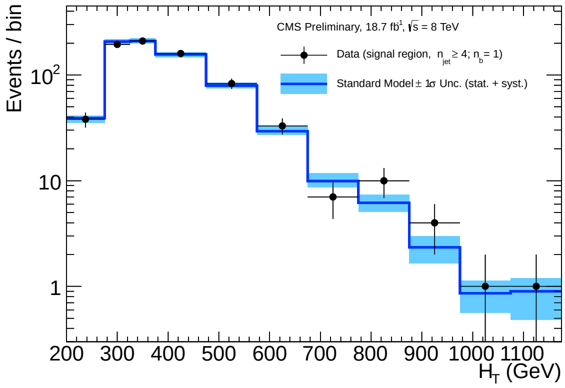

(b) Hadronic sample (logarithmic scale)

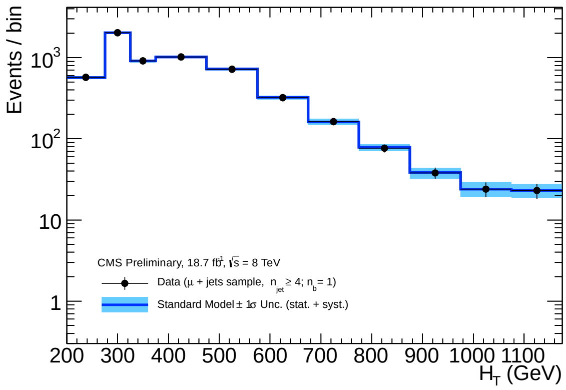

(c) μ+jets sample

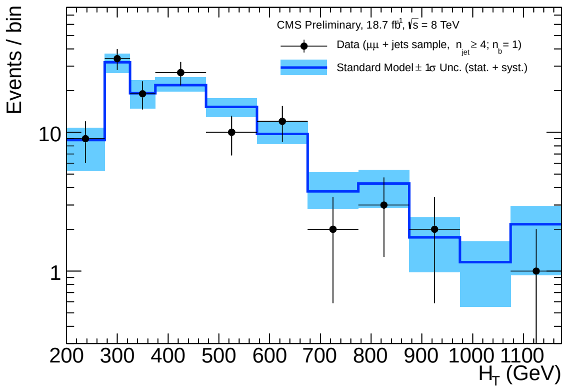

(d) $\mu\mu$+jets sample

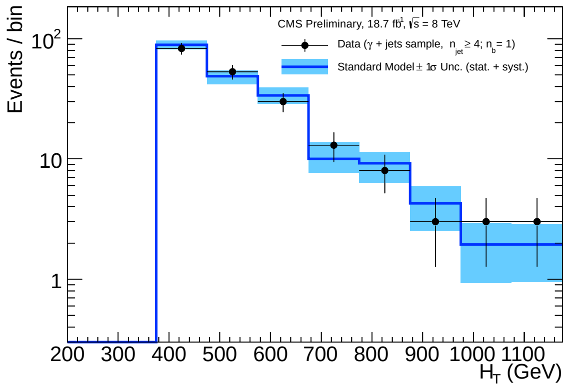

(e) γ+jets sample

Fig. 8.14 Observations in data for the signal and control regions of the analysis, compared to the result of the full likelihood model simultaneous fit. The plots shown are for the $n_{\text{jet}} \geq 4$, $n_{\text{b}} = 1$ analysis category.

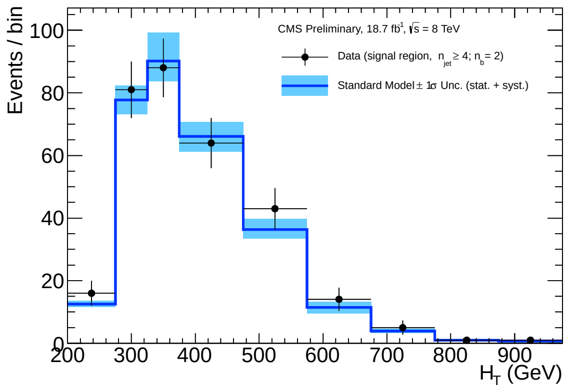

(a) Hadronic sample (linear scale)

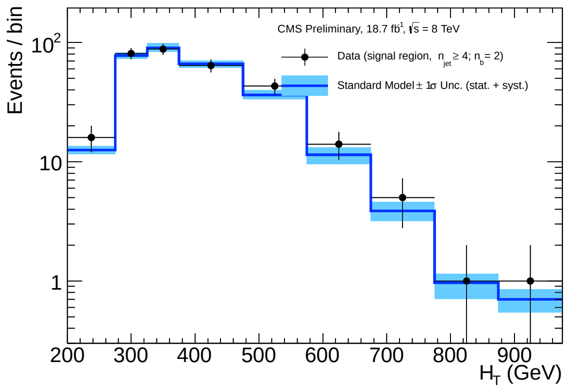

(b) Hadronic sample (logarithmic scale)

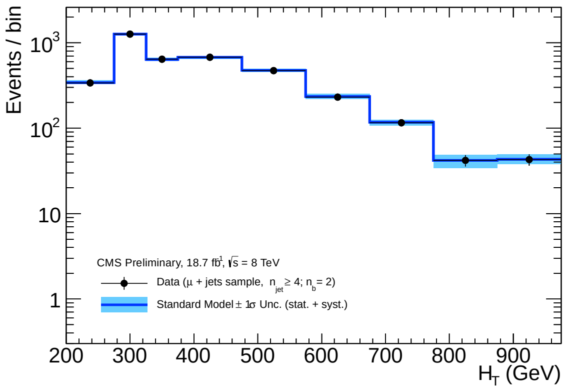

(c) μ+jets sample

Fig. 8.15 Observations in data for the signal and control regions of the analysis, compared to the result of the full likelihood model simultaneous fit. The plots shown are for the $n_{\mathrm{jet}} \geq 4$, $n_{\mathrm{b}} = 2$ analysis category.

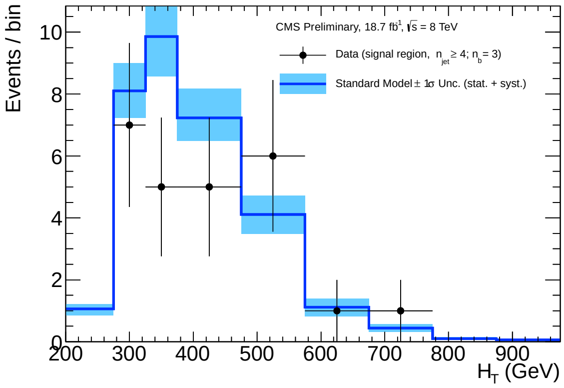

(a) Hadronic sample (linear scale)

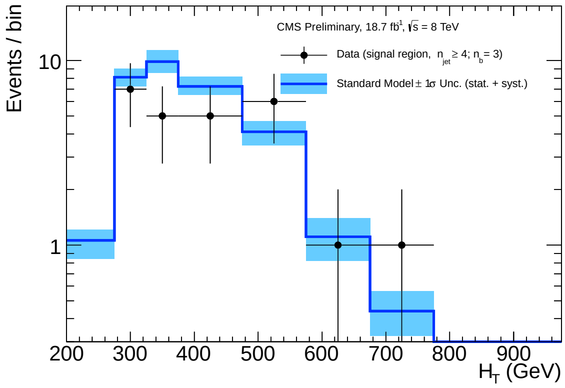

(b) Hadronic sample (logarithmic scale)

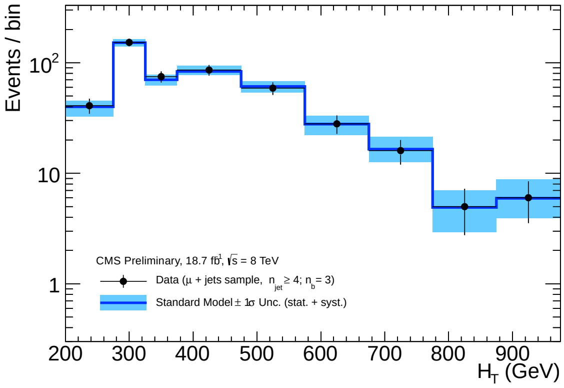

(c) μ+jets sample

Fig. 8.16 Observations in data for the signal and control regions of the analysis, compared to the result of the full likelihood model simultaneous fit. The plots shown are for the $n_{\mathrm{jet}} \geq 4$, $n_{\mathrm{b}} = 3$ analysis category.

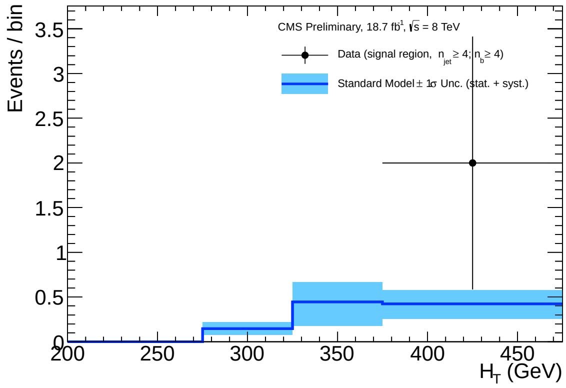

(a) Hadronic sample (linear scale)

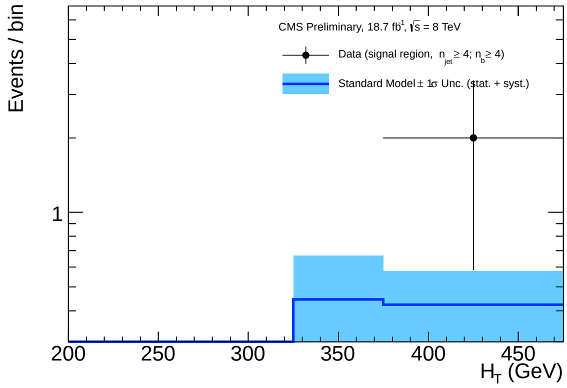

(b) Hadronic sample (logarithmic scale)

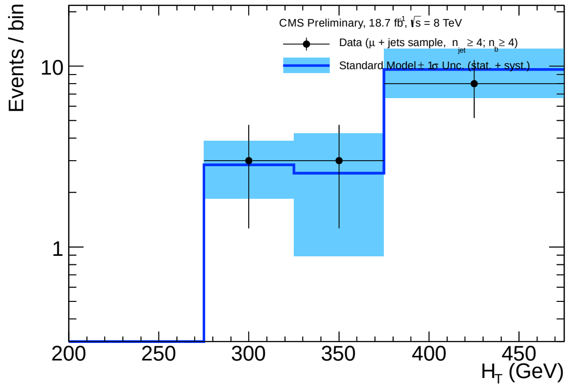

(c) μ+jets sample

Fig. 8.17 Observations in data for the signal and control regions of the analysis, compared to the result of the full likelihood model simultaneous fit. The plots shown are for the $n_{\mathrm{jet}} \geq 4$, $n_{\mathrm{b}} \geq 4$ analysis category.

Chapter 9

Interpretation

9.1 Signal Acceptance

Model acceptance is determined as a function of analysis category (n_{b}, n_{jet}) and H_T bin. This calculation is performed individually for each mass point in the scan plane for both the hadronic and muon selections (to determine signal contamination in the control region). Interpretations are made using a selected subset of the most sensitive analysis categories, but an inclusive H_T selection. The analysis categories are selected after an inspection of each for their significance given signal injection from specific mass points.

9.1.1 Charm decay

Signal efficiency times acceptance for the charm decay model, pp $\rightarrow \widetilde{t}\widetilde{t}^{*} \rightarrow \mathrm{c}\widetilde{\chi}^{0}\,\bar{\mathrm{c}}\widetilde{\chi}^{0}$, is shown in figure 9.1 for the four categories with the greatest sensitivity. The largest acceptance is seen in the $2 \leq n_{\mathrm{jet}} \leq 3$, $n_{\mathrm{b}} = 0$ analysis category (figure 9.1a), where efficiencies are around the percent level. At small mass splittings, nearest the kinematically inaccessible diagonal region, acceptance is due to hard initial state radiation (ISR) jets balancing a soft SUSY decay system. Small mass splittings imply little energy being available for decay products to gain sufficient momentum to be within acceptance, and therefore become invisible to the analysis. In order for such an event to pass the selection criteria of the signal sample, hard ISR jets are required to be within kinematic acceptance and boosting this decay system.

Moving away from the diagonal to increasing values of Δm indicates a drop in acceptance, eventually leading to an increase due to a competing effect from the increase in available kinematic phase space. Far from the diagonal, decay products are able to gain sufficient momentum to enter acceptance and become visible. There is still a dependence on ISR jets boosting this system, however crucially jets originating from charm quarks can now be observed. Contributions to acceptance therefore increase not only for this $n_{\mathrm{b}} = 0$ category, but similarly for $n_{\mathrm{b}} = 1$ categories, due to mistagging of the visible charm jets, where lower acceptance is observed at small Δm.

Finally, increased acceptance is observed in the $n_{\mathrm{jet}} \geq 4$ categories, predominantly away from the diagonal. Again, given the increased kinematic phase space of the larger mass splitting scenarios, more jets are above the analysis threshold and therefore visible.

Signal contamination in the μ+jets selection is shown to be negligible, given the lack of leptons in the final state.

Example cut-flows are shown in table 9.1 for two mass points with the extremal Δm values of the scan, both for values of $m_{\tilde{t}}$ near the limits of sensitivity.

Table 9.1 Cutflow table for two mass points ($m_{\tilde{t}}$ = 250 GeV, $m_{\tilde{\chi}^0}$ = 240 GeV and $m_{\tilde{t}}$ = 250 GeV, $m_{\tilde{\chi}^0}$ = 170 GeV) of the charm decay signal model. The selection represents the hadronic signal region for the $H_T > 375$ GeV region.

Cut Name	Cumulative Eff. (%)	
($m_{\tilde{t}}$, $m_{\tilde{\chi}^0}$)	(250, 240)	(250, 170)
Event Counter	100.00	100.00
$n_{\mathrm{jet}} \geq 2$	12.99	59.52
MET Filters	12.99	59.52
Vertex Noise Filter	12.99	59.52
HBHE Noise Filter	12.99	59.52
DeadECAL Filter	10.77	43.88
$n_e = 0$	10.77	43.88
$n_\gamma = 0$	10.77	43.7
$n_\mu = 0$	10.77	43.7
EMF$_{max}$ for all jets > 0.1	10.77	43.7
Leading jet $p_{\mathrm{T}} > 100$ GeV	7.37	24.79
Leading jet $\eta < 2.5$	7.04	24.21
Sub-Leading jet $p_{\mathrm{T}} > 100$ GeV	2.31	8.92
$n_{j,fail} = 0$	2.26	8.66
$\Delta R(\mu^i_{fail}, jet^j) < 0.5$	2.26	8.65
$(\sum^{n_{vertices}} p_{\mathrm{T}})$ / H_T	2.26	8.65
recHitCut	2.26	8.65
$n_{SIT} = 0$	2.09	8.03
$\Delta\phi^*_{min} > 0.3$	1.84	5.42
$\not{H}_T / \not{E}_T < 1.25$	1.68	4.46
$H_T > 375$ GeV	0.90	2.05
$\alpha_{\mathrm{T}} > 0.55$	0.45	0.40
$\not{H}_T / \not{E}_T < 1.25$	0.45	0.40

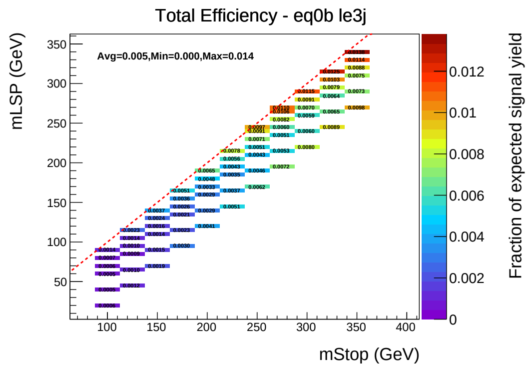

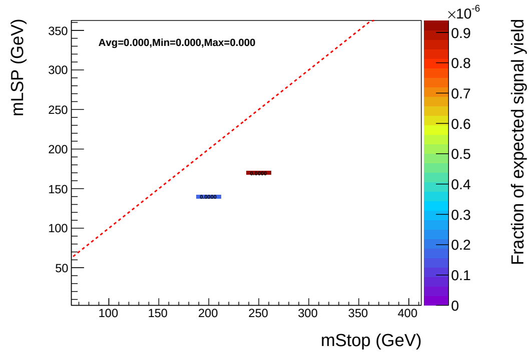

(a) Signal region, (2–3,0) (b) μ+jets region, (2–3,0)

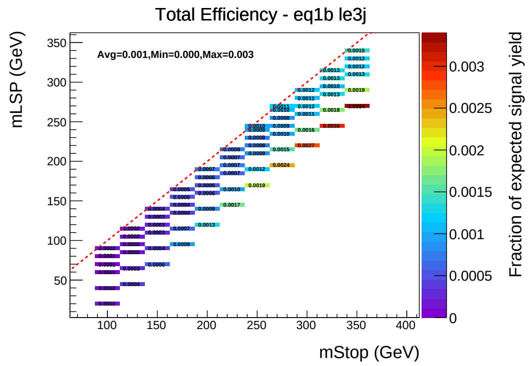

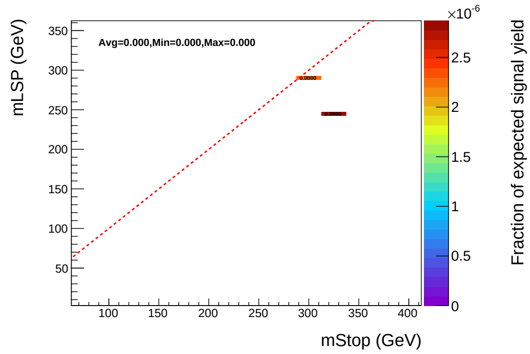

(c) Signal region, (2–3,1) (d) μ+jets region, (2–3,1)

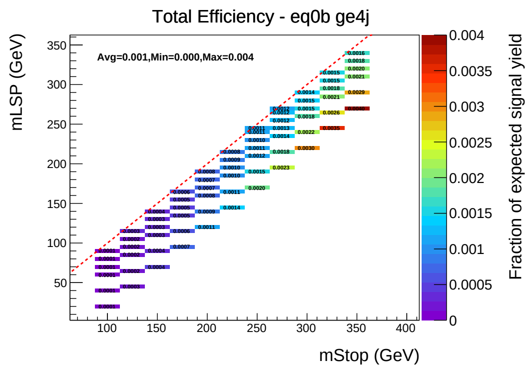

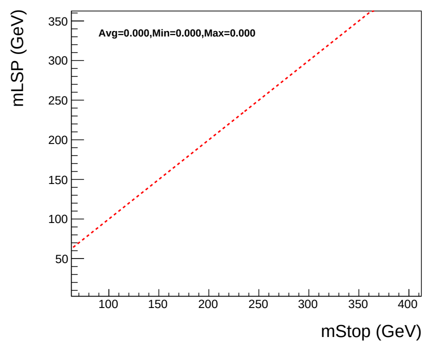

(e) Signal region, ($\geq$ 4,0) (f) μ+jets region, ($\geq$ 4,0)

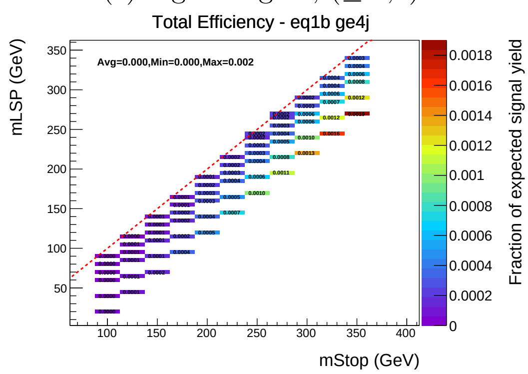

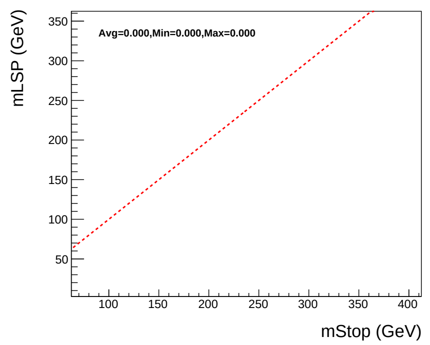

(g) Signal region, ($\geq$ 4,1) (h) μ+jets region, ($\geq$ 4,1)

Fig. 9.1 Signal efficiency times acceptance of the pp $\rightarrow \widetilde{t}\widetilde{t}^{*} \rightarrow c\widetilde{\chi}^{0}\,\bar{c}\widetilde{\chi}^{0}$ simplified model, for the hadronic selection (left) and the μ+jets selection (right), shown for the four most sensitive analysis categories with an inclusive selection on H_T.

9.1.2 Four-body decay

The signal efficiency times acceptance distributions for the four-body model, pp $\rightarrow \widetilde{t}\widetilde{t}^{*} \rightarrow$ b$ff'\widetilde{\chi}^{0}$ b$ff'\widetilde{\chi}^{0}$, are shown in figure 9.2 in the four most sensitive analysis categories. The plots show inclusive H_T selections, both for the hadronic and μ+jets selections. There are strong similarities with the acceptance profiles shown earlier for the charm decay model, both in magnitude and distribution about the plane. At small values of Δm, given that the entire SUSY decay system becomes invisible due to a lack of available kinematic phase space, both models show very similar efficiencies, where acceptance is almost entirely due to hard ISR jets. There is a significant difference however, when a b-tagged jet is required, for example in the $2 \leq n_{\mathrm{jet}} \leq 3$, $n_{\mathrm{b}} = 1$ category (figure 9.2c), where the presence of a jet originating from a real b quark improves acceptance, particularly away from the diagonal where the jet is more likely

Table 9.2 Cutflow table for two mass points ($m_{\widetilde{t}} = 250$ GeV, $m_{\widetilde{\chi}^0} = 240$ GeV and $m_{\widetilde{t}} = 250$ GeV, $m_{\widetilde{\chi}^0} = 170$ GeV) of the four-body decay signal model. The selection represents the hadronic signal region for the $H_T > 375$ GeV region.

Cut Name	Cumulative Eff. (%)	
($m_{\widetilde{t}}$, $m_{\widetilde{\chi}^0}$)	(250, 240)	(250, 170)
Event Counter	100.00	100.00
$n_{\mathrm{jet}} \geq 2$	10.80	32.33
MET Filters	10.80	32.33
Vertex Noise Filter	10.80	32.33
HBHE Noise Filter	10.80	32.33
DeadECAL Filter	9.13	21.30
$n_e = 0$	9.13	19.70
$n_\gamma = 0$	9.13	19.55
$n_\mu = 0$	9.13	17.41
EMF$_{max}$ for all jets > 0.1	9.13	17.41
Leading jet $p_{\mathrm{T}} > 100$ GeV	6.01	8.70
Leading jet $\eta < 2.5$	5.70	8.37
Sub-Leading jet $p_{\mathrm{T}} > 100$ GeV	1.64	2.23
$n_{j,fail} = 0$	1.61	2.17
$\Delta R(\mu^i_{fail}, jet^j) < 0.5$	1.61	2.11
$(\sum^{n_{vertices}} p_{\mathrm{T}})\ /\ H_T$	1.61	2.11
recHitCut	1.61	2.11
$n_{SIT} = 0$	1.50	1.67
$\Delta\phi^*_{min} > 0.3$	1.35	0.93
$\not{H}_T / \not{E}_T < 1.25$	1.24	0.68
$H_T > 375$ GeV	0.55	0.37
$\alpha_{\mathrm{T}} > 0.55$	0.26	0.08
$\not{H}_T / \not{E}_T < 1.25$	0.26	0.08

to pass analysis thresholds. Less significant are the efficiencies seen in the $n_{\text{jet}} \geq 4$ categories, given the larger number of final state objects, each requiring a share of the energy originating from the mass splitting of the mother and daughter sparticles.

Also of note is the increase in signal contamination observed in the μ+jets selection, due to the presence of $f\bar{f}$ in the decay chain, potentially introducing leptons to the final state.

Example cut-flows are shown in table 9.2 for two mass points with extremal Δm, at an $m_{\tilde{t}}$ value near the limit of sensitivity.

9.1.3 ISR Corrections to compressed spectra MC signal samples

Given the reliance of such compressed spectra models on ISR jets for acceptance, a dedicated study was performed within the SUSY Physics Analysis Group (*PAG*) into the accuracy of it's modelling and relevant systematic uncertainties [11].

A comparison of data to MC for a pure, high-statistics selection of Z boson production with associated jets, where the Z decays to an opposite-sign, same-flavour (OSSF) lepton pair, $Z \rightarrow l\bar{l}$. By tagging the leptons in the event, remaining jets can be considered as an ISR jet "recoil system" against that of the Z boson decay. Comparisons of data to MC for both the vectorial sum of the lepton $\overrightarrow{p_{\text{T}}}$'s and the recoil jet system's $\overrightarrow{p_{\text{T}}}$ indicate an over-prediction in MC as a function of the system's p_{T}, of up to 20% in high p_{T} scenarios, shown in figure 9.3.

Correction factors for MadGraph based samples, dependent on the p_{T} of the jet system, can therefore be derived by extracting the ratio of data to MC. These values are summarised in table 9.3. Weights are applied to both signal samples at the event level, where the event's boost p_{T} is determined by calculating the vectorial sum of the two, pair-produced generator level $\tilde{t}$ particles.

Table 9.3 Correction factors for MadGraph based signal samples to account for MC over-prediction of ISR.

$p_{\text{T}boost}$ (GeV)	Correction Factor
$0 < p_{\text{T}} \leq 120$	1.00
$120 < p_{\text{T}} \leq 150$	0.95
$150 < p_{\text{T}} \leq 250$	0.90
$250 < p_{\text{T}}$	0.80

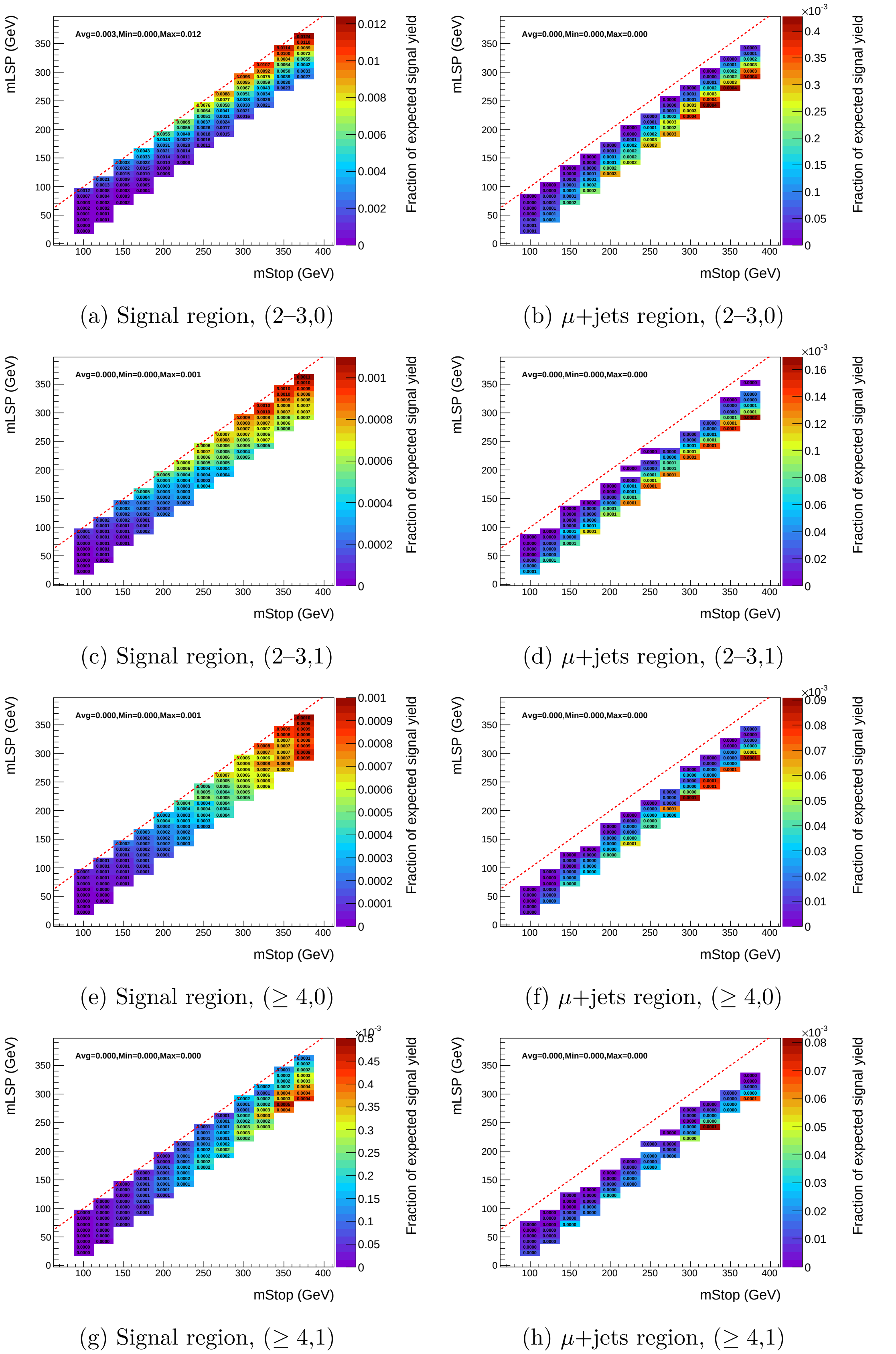

(a) Signal region, (2–3,0) (b) μ+jets region, (2–3,0)

(c) Signal region, (2–3,1) (d) μ+jets region, (2–3,1)

(e) Signal region, ($\geq$ 4,0) (f) μ+jets region, ($\geq$ 4,0)

(g) Signal region, ($\geq$ 4,1) (h) μ+jets region, ($\geq$ 4,1)

Fig. 9.2 Signal efficiency times acceptance of the pp $\rightarrow \widetilde{t}\widetilde{t}^* \rightarrow \mathrm{b}ff'\widetilde{\chi}^0\,\mathrm{b}ff'\widetilde{\chi}^0$ simplified model, for the hadronic selection (left) and the μ+jets selection (right), shown for the four most sensitive analysis categories with an inclusive selection on H_T.

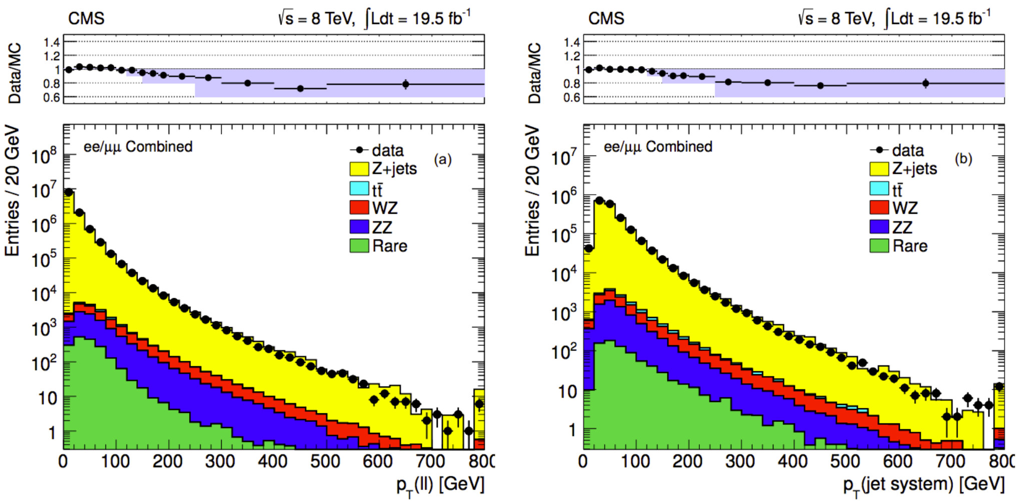

Fig. 9.3 Data to MC comparisons for an enriched $Z \rightarrow l\bar{l}$ selection, with the vectorial sum of lepton p_{T}'s (left) and of the recoil jets (right) [11].

9.2 Systematic Uncertainties on Signal Acceptance

A range of sources of systematic uncertainty on the acceptance times signal efficiency are considered for each signal model. The main sources, namely jet energy scale (JES), initial state radiation (ISR), b tag scale factors, parton distribution function (PDF), the $\not{H}_T/\not{E}_T$ cut and the dead ECAL filter, have systematic values determined per point in the scan plane, as a function of H_T, n_{b} and n_{jet}. The remaining systematics are applied as a flat contribution across the entire plane, considered as a conservative approach.

Although systematics are considered as a function of the H_T dimension of the analysis, all results discussed here are representative of an inclusive selection of H_T >200 GeV.

9.2.1 Jet Energy scale

The acceptance times signal efficiency is tested for sensitivity to jet energies by measuring its sensitivity to upwards and downwards variations of all jet energies by the p_{T} and η-dependent jet energy scale (JES) uncertainty, as prescribed by the JetMET *POG*. When systematic variations in jet energy scale are applied, it is possible for jets to move both in and out of acceptance, therefore moving events between different analysis categories. To negate this effect, the overall acceptance change is probed by considering an inclusive analysis selection, $n_{\mathrm{jet}} \geq 2$ and $n_{\mathrm{b}} \geq 0$.

Distributions showing the acceptance changes due to the variations in JES are shown in Appendix A for both signal models. Systematics are on the order of a few percent for both models.

9.2.2 Initial State Radiation

As described in section 9.1.3, boost-p_{T} dependent event weights are taken from the study performed within the SUSY *PAG*. A procedure is also defined to determine related systematics, by applying upwards and downwards variations of weights corresponding to the magnitude of the corrections themselves, and studying the effect on signal efficiency times acceptance. These weights are summarised in table 9.4.

Table 9.4 Systematic factors for MadGraph based signal samples to determine ISR modelling related systematics.

$p_{\mathrm{T}boost}$ (GeV)	Systematic Variation
$0 < p_{\mathrm{T}} \leq 120$	± 0.0
$120 < p_{\mathrm{T}} \leq 150$	± 0.05
$150 < p_{\mathrm{T}} \leq 250$	± 0.10
$250 < p_{\mathrm{T}}$	± 0.20

As discussed previously in sections 9.1.1 and 9.1.2, acceptance for compressed spectra models at the smallest Δm (i.e. nearest the diagonal) is predominantly due to presence of hard ISR jets. Away from the diagonal, ISR jets are still important, instead to boost the soft SUSY decay system. Subsequently, systematics due to ISR variations are observed to be largest nearest the diagonal for all analysis categories, as shown in figure A.3 and A.9 for the charm and four-body decay models respectively. Due to the overall dependence on ISR, the related systematics are the largest contribution to the total systematic value for the compressed models considered here.

9.2.3 B tag scale factors

Specifically for FastSim signal samples, events are not weighted using the b tag formula method described in section 5.4, but instead using the recommended method for FullSim samples with an additional FullSim to FastSim correction factor applied.

The original correction is dependent on the generator level content of an event, and is defined as:

$$w = \frac{SF_b\epsilon \times (1 - SF_b\epsilon) \times SF_{c,light}m \times (1 - SF_{c,light}m)}{\epsilon \times (1-\epsilon) \times m \times (1-m)}, \tag{9.1}$$

where $\epsilon(p_{\mathrm{T}}, \eta)$ and $m(p_{\mathrm{T}}, \eta)$ are the b tagging efficiency and mistagging rate, respectively. These factors are functions of p_{T} and η, and are measured in SM MC for both the hadronic and μ+jets samples, in each H_T bin.

Applying this event weight provides 'corrected' MC yields, which then have further FastSim to FullSim correction factors applied, as recommended by [79]. Systematic variations equal to the errors of these corrections are applied as upwards and downwards variations, and any effects on signal efficiency times acceptance are studied.

As expected, only small changes in acceptance are found in the charm decay model when b tag scale factor variations are applied, as shown in figure A.4. While not entirely negligible, it is worth noting that systematics are slightly larger for the $n_{\mathrm{b}} = 1$ category (figure A.4f), however still at a low level with respect to other systematic sources.

The four-body decay model exhibits a similar dependence on the b tag scale factor variations, indicating large changes in efficiency nearer the diagonal in $n_{\mathrm{b}} = 1$ categories. This increase is visible in figure A.10f at smaller values of Δm, where the final state b quark is likely out of acceptance, and therefore tags originate from mistagged lighter quarks or gluons.

9.2.4 PDF

MonteCarlo generation includes a simulation of the Parton Density Function (PDF) of the incoming partons, described by a 'PDF set'. Signal samples are produced using the CTEQ6L1 PDF set. The acceptance sensitivity to the PDF set is investigated by comparing results using three other commonly used PDF sets, namely CT10, NNPDF2.1 and MSTW2008. Following PDF4LHC recommendations, the output is combined to determine an 'envelope' value combining the three alternative PDF sets and a related systematic uncertainty [80].

The effect on selection efficiency was studied for charm decay model with the central value and upwards and downwards fluctuation plots summarised in figure A.2. The largest variations are taken as the systematic uncertainty for both signal models, given their identical initial states.

9.2.5 $\not{H}_T/\not{E}_T$ cleaning cut

The efficiency of the $\not{H}_T/\not{E}_T$ cleaning cut is compared between data and MC with the aim of revealing any potential issues due to MC mismodelling of the variable. Efficiencies are compared in the μ+jets control sample, using H_T bins ranging from $200 < H_T < 375$ GeV, in both n_{jet} categories, with no requirement on n_{b}. Efficiencies are summarised in table 9.5, where efficiency comparisons between data and MC are shown to statistically agree with unity.

Table 9.5 Efficiencies of the $\not{H}_T/\not{E}_T$ requirement cut for the μ+jets selection in data ϵ_{data} and MC ϵ_{MC}, as well as the ratio of both. Efficiencies are shown for the two n_{jet} categories and the four lowest H_T bins, with an inclusive requirements are made of n_{b}.

n_{jet}	H_T (GeV)	ϵ_{MC}	ϵ_{data}	$\epsilon_{\mathrm{MC}}/\epsilon_{\mathrm{data}}$
2–3	200–275	0.95 ± 0.00	0.95 ± 0.01	1.00 ± 0.01
2–3	275–325	0.97 ± 0.01	0.97 ± 0.02	1.00 ± 0.02
2–3	325–375	0.97 ± 0.01	0.97 ± 0.02	1.00 ± 0.02
2–3	375–475	0.98 ± 0.01	0.98 ± 0.03	1.00 ± 0.03
≥ 4	200–275	0.90 ± 0.02	0.92 ± 0.04	0.98 ± 0.04
≥ 4	275–325	0.92 ± 0.01	0.93 ± 0.02	0.99 ± 0.02
≥ 4	325–375	0.92 ± 0.01	0.93 ± 0.04	0.99 ± 0.04
≥ 4	375–475	0.95 ± 0.02	0.95 ± 0.04	1.00 ± 0.04

While the relevant systematic for the $\not{H}_T/\not{E}_T$ requirement is taken from the above method, it is also interesting to study the acceptance of this cut as a function of the mass plane for each decay. Model acceptance to the $\not{H}_T/\not{E}_T$ cut is typically lower in the four-body decay. This is attributed to the softer jet spectrum produced due to the increased number of final state particles sharing the finite energy of the decay system.

9.2.6 Dead ECAL Filter

To assess any potential MC mismodelling issues with the dead ECAL filter, a similar analysis is made as described for the $\not{H}_T/\not{E}_T$ cut in section 9.2.5. Efficiencies between data and MC are compared for the μ+jets selection, with an inclusive requirement on both n_{b} and H_T. As shown in table 9.6, the ratio of efficiencies between data and MC for each n_{jet} category agree within statistical errors.

Similarly to the study of the $\not{H}_T/\not{E}_T$ requirement, an inspection of the acceptance of the dead ECAL filter in each scan plane indicates a greater reduction in acceptance for the four-body decay with respect to the charm decay. The larger number of

Table 9.6 Efficiencies of the dead ECAL filter for the μ+jets selection in data ϵ_{data} and MC ϵ_{MC}, as well as the ratio of both. Efficiencies are shown for the two n_{jet} categories and the four lowest H_T bins, with an inclusive requirements are made of n_{b}.

n_{jet}	H_T (GeV)	ϵ_{MC}	ϵ_{data}	$\epsilon_{\text{MC}}/\epsilon_{\text{data}}$
2–3	> 200	0.64 ± 0.01	0.64 ± 0.01	1.00 ± 0.01
≥ 4	> 200	0.58 ± 0.01	0.59 ± 0.01	0.98 ± 0.01

particles in the final state of the four-body decay increases the probability for an energy deposit to be made near a flagged region of the calorimeter system, thereby rejecting more events. Rejection increases away from the diagonal, as more objects move into acceptance.

9.2.7 Generator Level Partons

At the MadGraph matrix element stage of the MC simulation production, a number of additional Feynman diagrams are simulated to account for associated parton interactions, such as Initial State Radiation (ISR) and Final State Radiation (FSR). Given the dependence on such processes in the compressed regime, an additional subsample of the charm decay scan has been produced with up to 3 additional partons, to compare against the up to 2 additional partons of the complete scan. This sample contains two mass points at a stop mass near the region of maximum sensitivity, with mass splittings covering both extremities of the scan (Δm = 10 GeV, 80 GeV). The relative change in efficiency times acceptance between the two scans is shown in table 9.7. These values are interpreted as systematic uncertainties on the number of associated partons modelled for such compressed spectra models, and are applied as flat contributions across the scan plan for all models.

Table 9.7 Relative change in efficiency times acceptance for the 2-parton and 3-parton scans in the signal region, with an inclusive selection on n_{b} and H_T >200 GeV. The scan points are $m_{\tilde{t}}$ = 200 GeV and $m_{\tilde{\chi}^0} = (120, 190)$ GeV in the charm decay model.

Category	Δm (GeV)	
	10	80
(2–3,0)	0.00	0.04
(2–3,1)	0.02	0.04
($\geq$ 4,0)	0.04	0.04
($\geq$ 4,1)	0.00	0.00

9.2.8 Luminosity Measurement

Flat corrections across the scan plane are made to account for the uncertainty of the luminosity measurement, as quoted by the Lumi *POG* at 2.5% [81].

9.2.9 Summary

For each mass point in the scan plane, the total systematic is the sum in quadrature of all individual contributions. Representative values are summarised in tables 9.8 and 9.9, with full results shown in figures A.7 and A.13 in the mass plane of the charm and four-body decay models respectively. The distribution of total systematic values seen in these plots has been corrected to account for statistical fluctuations through the use of an iterative smoothing procedure that considers a weighted average for each mass point of the surrounding point values. This procedure is carefully checked to ensure no loss of total systematic trends throughout the mass plane.

Table 9.8 Representative ranges for each contribution to the total systematic uncertainty on the signal efficiency times acceptance for each relevant event category for the charm decay model interpretation.

Category	(2–3,0)		(2–3,1)		(≥ 4,0)		(≥ 4,1)		(≥ 2,≥ 0)	
Range	Min.	Max.	Min.	Max.	Min.	Max.	Min.	Max.	Min.	Max.
PDF									0.04	0.14
JES									0.02	0.10
ISR	0.11	0.21	0.08	0.21	0.16	0.22	0.14	0.23		
b tag SF	0.01	0.02	0.03	0.07	0.01	0.02	0.02	0.06		
$\not{H}_T/\not{E}_T$	0.02	0.02	0.02	0.02	0.02	0.02	0.02	0.02		
Dead ECAL	0.02	0.02	0.02	0.02	0.02	0.02	0.02	0.02		
Total syst	0.16	0.21	0.15	0.22	0.20	0.20	0.19	0.23		

9.3 Limits on models of Supersymmetry

9.3.1 Overview of limit setting procedure

Signal models are tested for compatibility with observations using a modified frequentist method, namely ‘CLs’ [82]. A test statistic, used to rank experiments from least

Table 9.9 Representative ranges for each contribution to the total systematic uncertainty on the signal efficiency times acceptance for each relevant event category for the four-body decay model interpretation.

Category	(2–3,0)		(2–3,1)		(≥ 4,0)		(≥ 4,1)		(≥ 2,≥ 0)	
Range	Min.	Max.	Min.	Max.	Min.	Max.	Min.	Max.	Min.	Max.
PDF									0.04	0.14
JES									0.01	0.07
ISR	0.15	0.20	0.14	0.21	0.17	0.21	0.16	0.23		
b tag SF	0.01	0.02	0.02	0.07	0.01	0.03	0.00	0.06		
$\not{H}_T/\not{E}_T$	0.02	0.02	0.02	0.02	0.02	0.02	0.02	0.02		
Dead ECAL	0.02	0.02	0.02	0.02	0.02	0.02	0.02	0.02		
Total syst	0.24	0.27	0.25	0.28	0.24	0.34	0.25	0.33		

to most signal-like, is defined as:

$$q_\mu = \begin{cases} -2log\lambda(\mu), & \text{if } \mu \geq \hat{\mu} \\ 0., & \text{otherwise} \end{cases}, \tag{9.2}$$

where:

$$\lambda(\mu) = \frac{L(\mu, \theta_\mu)}{L(\hat{\mu}, \hat{\theta_\mu})}, \tag{9.3}$$

μ is the signal strength parameter (equivalent to the variable f defined in section 8.1, where $\mu = 1$ represents a given signal at it's nominal theoretical cross-section), θ_μ is a set of nuisance parameters for a given μ, $\hat{\mu}$ is the Maximum Likelihood (ML) value of μ, and $\hat{\theta}$ is the corresponding ML set of nuisance parameters.

A cartoon example of distributions of the test statistic, q_μ, is shown in figure 9.4. Distributions of q_μ are populated from pseudo-experiments under signal + background and background only hypotheses. For a given observation, 1 minus the quantiles of each distribution are used to determine CL_{s+b} and CL_b, which are used to define:

$$CL_s = \frac{CL_{s+b}}{CL_b}. \tag{9.4}$$

A model is considered to be excluded at 95% confidence level if $CL_s \leq 0.05$.

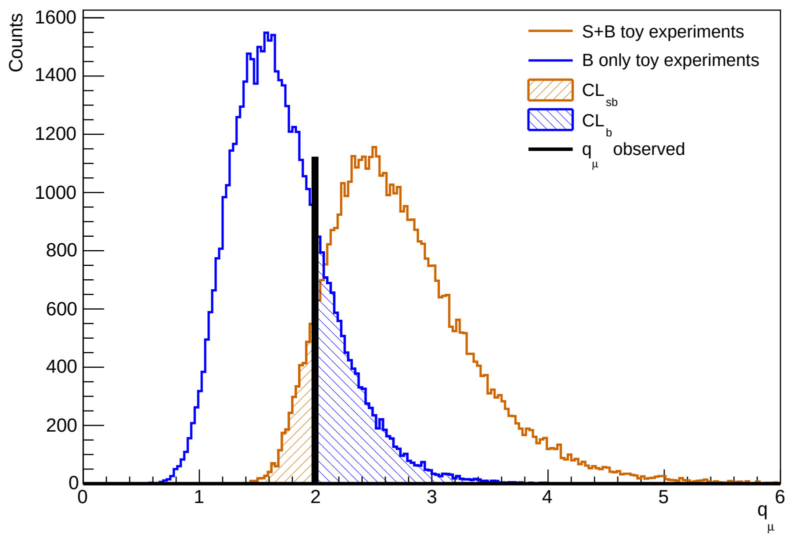

Fig. 9.4 Example distributions of the test statistic, q_μ for Signal+Background (orange) and Background-only (blue) scenarios. The observed value of q_μ is shown in black, with orange and blue quantiles representing CL_{s+b} and CL_b respectively.

9.3.2 Limits

Limits are calculated using 1000 pseudo-experiments per model mass point. Expected limits are determined by considering a scenario where data observations are assumed to be equal to the result of the green-band fits (section 8.2.1), and observed limits by considering the actual data observations. A point is considered excluded if the calculated upper limit cross section is less than the nominal theoretical cross-section (NLO+NLL).

Limits are shown in the $m_{\tilde{t}}$ vs. $m_{\tilde{\chi}^0}$ mass-plane for both the charm (figure 9.5) and the four-body (figure 9.6) decay models. Excluded limits are drawn as dashed red lines, with $\pm 1\sigma_{experimental}$ and $\pm 2\sigma_{experimental}$ uncertainty bands as thin, red dashed lines. The observed limit is drawn as a solid, black line, with $\pm 1\sigma_{theory}$ uncertainty bands as thin black. The 95% confidence upper limit on the cross section is shown as a colour map as a function of the mass plane.

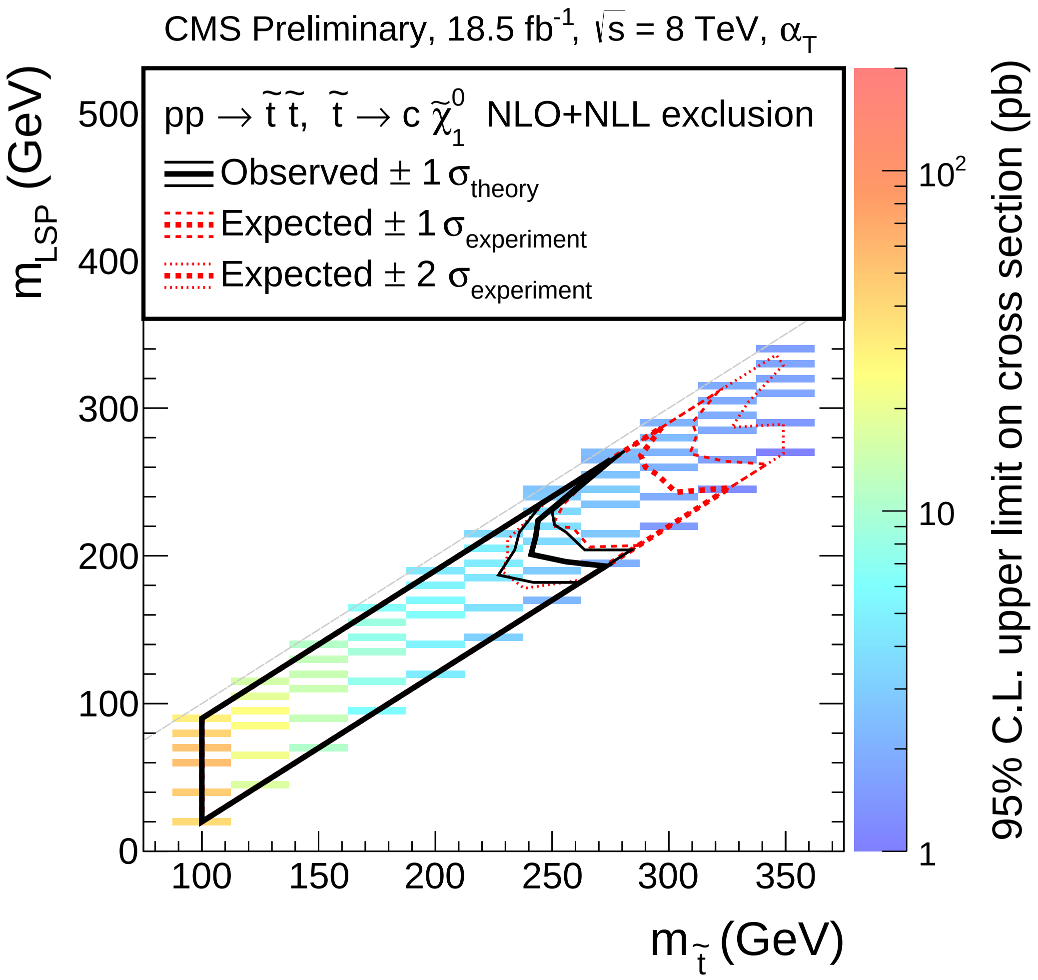

Fig. 9.5 The expected limit (red dashed line) with central band (thick red) and $\pm 1\sigma$ and $\pm 2\sigma$ uncertainty bands (thin red), and the observed limit (thick black) for the charm decay model. The limit is calculated with an inclusive H_T >200 GeV selection, and the analysis categories ($n_\mathrm{b} = 0, 2 \leq n_\mathrm{jet} \leq 3$), ($n_\mathrm{b} = 1, 2 \leq n_\mathrm{jet} \leq 3$), ($n_\mathrm{b} = 0, n_\mathrm{jet} \geq 4$), ($n_\mathrm{b} = 1, n_\mathrm{jet} \geq 4$).

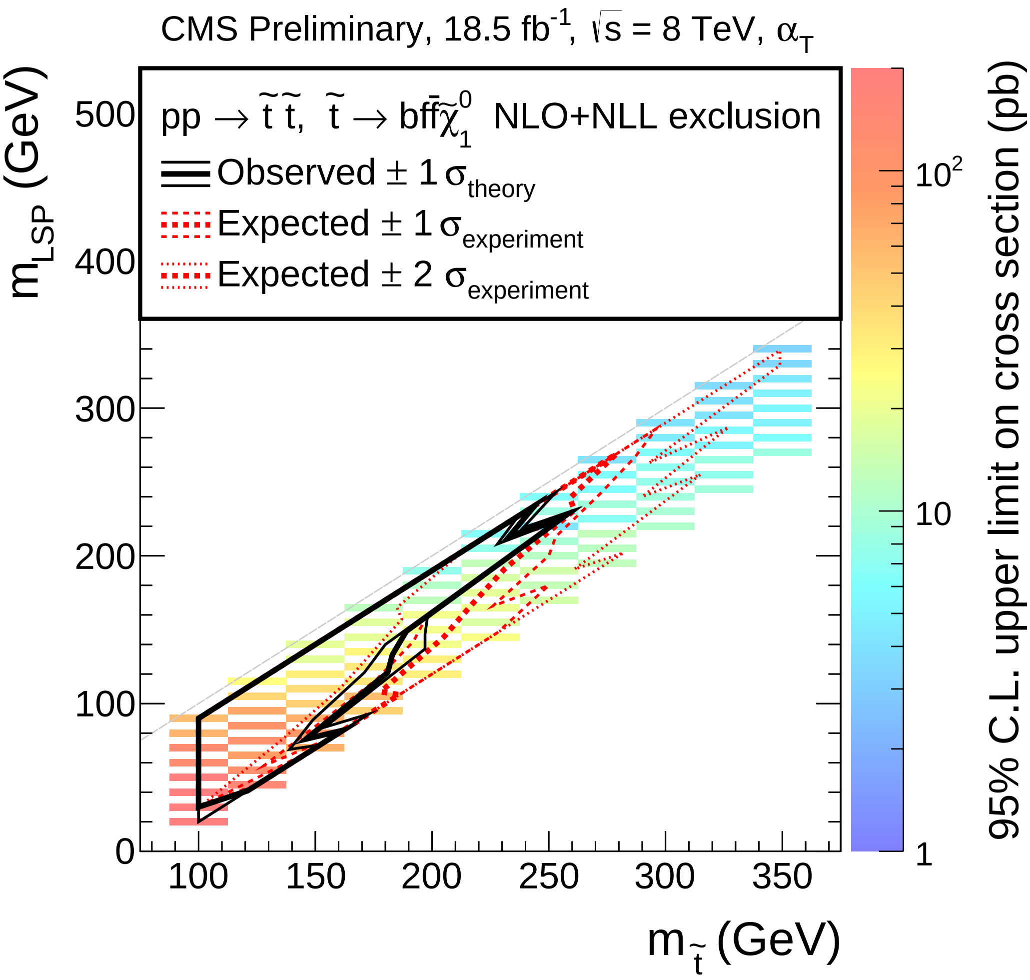

Fig. 9.6 The expected limit (red dashed line) with central band (thick red) and $\pm 1\sigma$ and $\pm 2\sigma$ uncertainty bands (thin red), and the observed limit (thick black) for the four-body decay model. The limit is calculated with an inclusive H_T >200 GeV selection, and the analysis categories ($n_\mathrm{b} = 0, 2 \leq n_\mathrm{jet} \leq 3$), ($n_\mathrm{b} = 1, 2 \leq n_\mathrm{jet} \leq 3$), ($n_\mathrm{b} = 0, n_\mathrm{jet} \geq 4$), ($n_\mathrm{b} = 1, n_\mathrm{jet} \geq 4$).

Chapter 10

Conclusion

A search for Supersymmetry has been presented based on the full 18.5 fb^{-1}, $\sqrt{s} =$ 8 TeV 'Parked' dataset from the CMS detector at the LHC. This dataset was collected using using experimental, low-threshold triggers to increase sensitivity to soft decays of new physics. The analysis searches for pair-produced gluinos or squarks decaying hadronically to jets and missing transverse energy due to the presence of the weakly-interacting lightest supersymmetric particle (LSP). The search is performed in dimensions of the total transverse hadronic energy, and the multiplicity of jets and b-tagged jets.

Dominant hadronic backgrounds from mismeasured QCD events are reduced by several orders of magnitude to a negligible level using the dimensionless kinematic variable α_{T}. Following the full signal selection criteria, remaining backgrounds consist of electroweak decays of heavy bosons or top quarks and are predicted using an extrapolation technique from dedicated control samples, orthogonal to the signal region. A total background estimation is determined from a likelihood model fit simultaneously considering both the signal and control regions. Systematic errors on the background prediction are determined using a suite of statistically powerful closure tests designed to probe the many different aspects of the analysis.

Observations in data statistically agree with the results of the background prediction, and as such interpretations have been made with respect to two simplified spectra SUSY models. Given the increased sensitivity of the triggers used, this thesis focuses on compressed models, where the pair-produced sparticles are near-degenerate in mass with the LSP. In this region of phase space two decays of the stop sparticle become dominant: a decay via a c quark and the LSP, and an off-shell W, b quark and the LSP. Limits on the mass of the stop squark with a c quark decay have been set of up to 275 GeV, with the limit remaining strong across the entire mass-splitting range - a feature currently unmatched by any other single analysis. Similarly for the four-body decay, stop squark mass limits are set of up to 250 GeV, found to be strongest when the neutralino is near-degenerate in mass with the stop.

While many turned to Run I of the LHC hoping for signs of SUSY, Nature has yet to deliver. Instead the phase space in which SUSY may reside has been greatly reduced. While answering many questions about the possible nature of what lies Beyond the Standard Model, the 8 TeV run also left many open. With the large increase of centre of mass energy to 13 TeV, and a similarly large rise in luminosity, Run II of the LHC will aim to address many of these outstanding questions. Thanks to the Large Hadron Collider we find ourselves in a historically familiar position - we are again standing at the edge of the energy frontier, peering into the unknown. Whatever we see, it's going to be exciting.

Appendix A

Signal Model Systematics Plots

Charm decay model

Jet Energy Scale

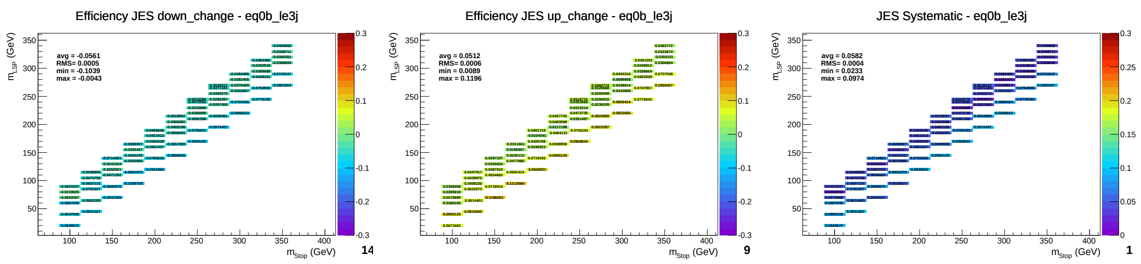

(a) $n_{\text{jet}} \geq 2$, $n_{\text{b}} \geq 0$. (b) $n_{\text{jet}} \geq 2$, $n_{\text{b}} \geq 0$. (c) $n_{\text{jet}} \geq 2$, $n_{\text{b}} \geq 0$.

Fig. A.1 The relative change in acceptance times signal efficiency for the charm decay model for downwards (left) and upwards (middle) fluctuations of all jet energies by the uncertainty of the jet energy scale, and the derived systematic values (right). The plots represent a fully inclusive selection - $n_{\text{jet}} \geq 2$, $n_{\text{b}} \geq 0$ and H_T >200 GeV.

PDF

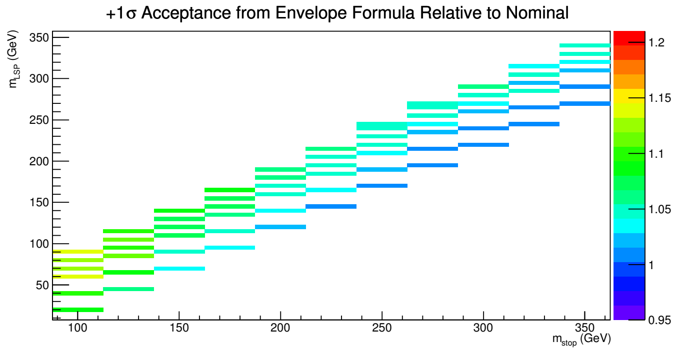

(a) $+1\sigma$

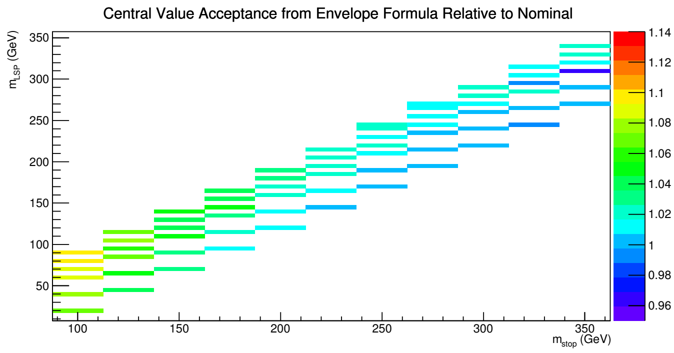

(b) Nominal

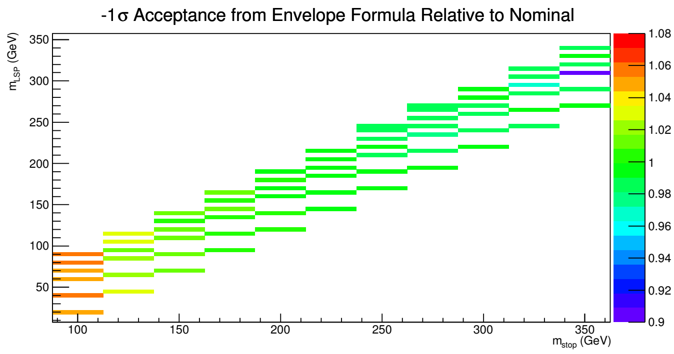

(c) -1σ

Fig. A.2 PDF uncertainties as a function of the charm decay model scan plane, calcualted using a PDF4LHC 'envelope' calculation to determine a central band (A.2b), and $\pm 1\sigma$ variations (A.2a and A.2c). Plots are a for a fully inclusive selection on H_T, n_{jet} and n_{b}.

Initial State Radiation

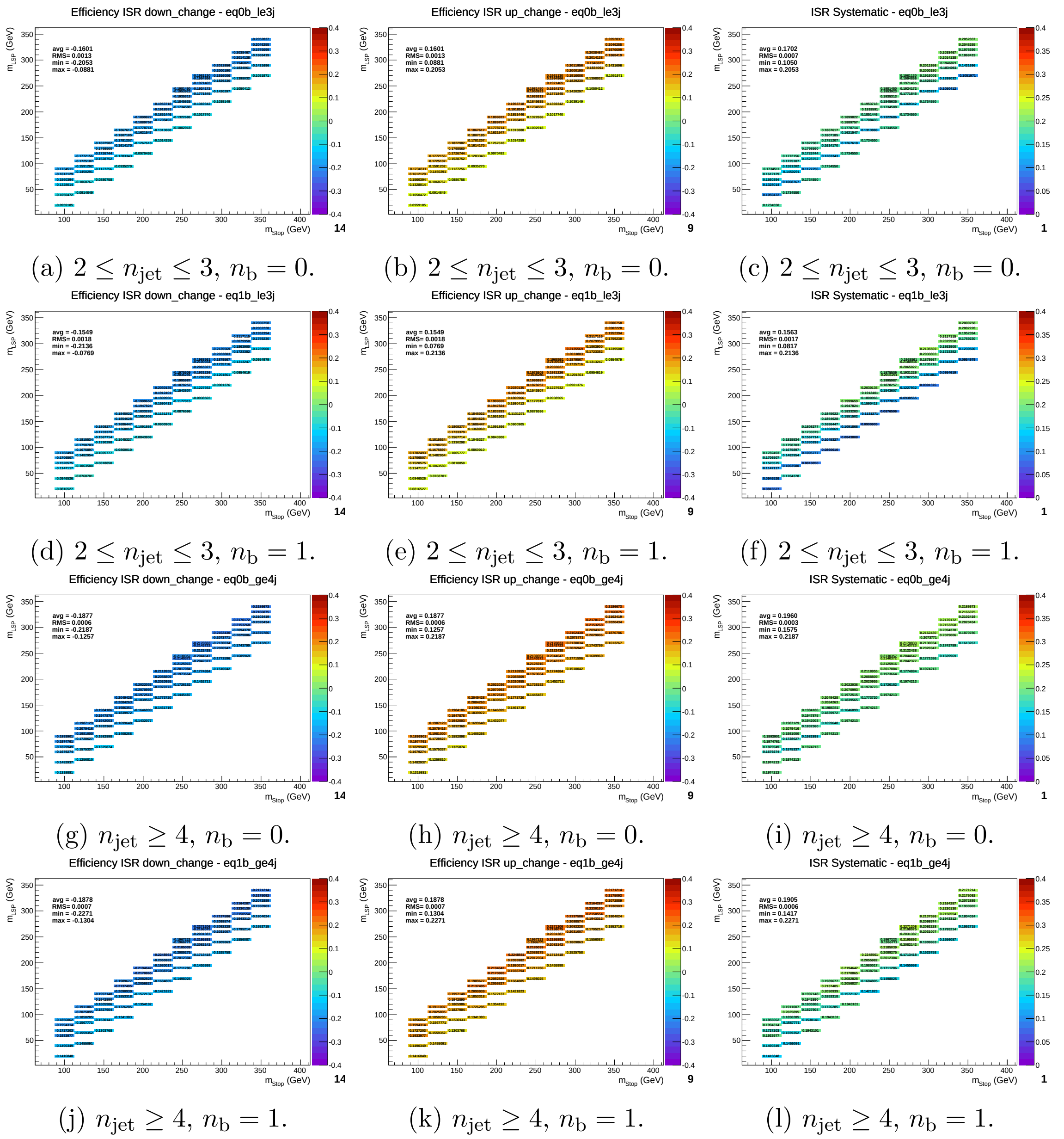

(a) $2 \leq n_{\text{jet}} \leq 3$, $n_{\text{b}} = 0$. (b) $2 \leq n_{\text{jet}} \leq 3$, $n_{\text{b}} = 0$. (c) $2 \leq n_{\text{jet}} \leq 3$, $n_{\text{b}} = 0$.

(d) $2 \leq n_{\text{jet}} \leq 3$, $n_{\text{b}} = 1$. (e) $2 \leq n_{\text{jet}} \leq 3$, $n_{\text{b}} = 1$. (f) $2 \leq n_{\text{jet}} \leq 3$, $n_{\text{b}} = 1$.

(g) $n_{\text{jet}} \geq 4$, $n_{\text{b}} = 0$. (h) $n_{\text{jet}} \geq 4$, $n_{\text{b}} = 0$. (i) $n_{\text{jet}} \geq 4$, $n_{\text{b}} = 0$.

(j) $n_{\text{jet}} \geq 4$, $n_{\text{b}} = 1$. (k) $n_{\text{jet}} \geq 4$, $n_{\text{b}} = 1$. (l) $n_{\text{jet}} \geq 4$, $n_{\text{b}} = 1$.

Fig. A.3 The relative change in acceptance times signal efficiency for the charm decay model for downwards (left) and upwards (middle) fluctuations of the global event weight equal to the magnitude of the ISR corrections, and the derived systematic values (right). Each set of plots corresponds to one of the four most sensitive analysis categories (n_{b}, n_{jet}), with the inclusive requirement H_T >200 GeV.

B-tag Scale Factor

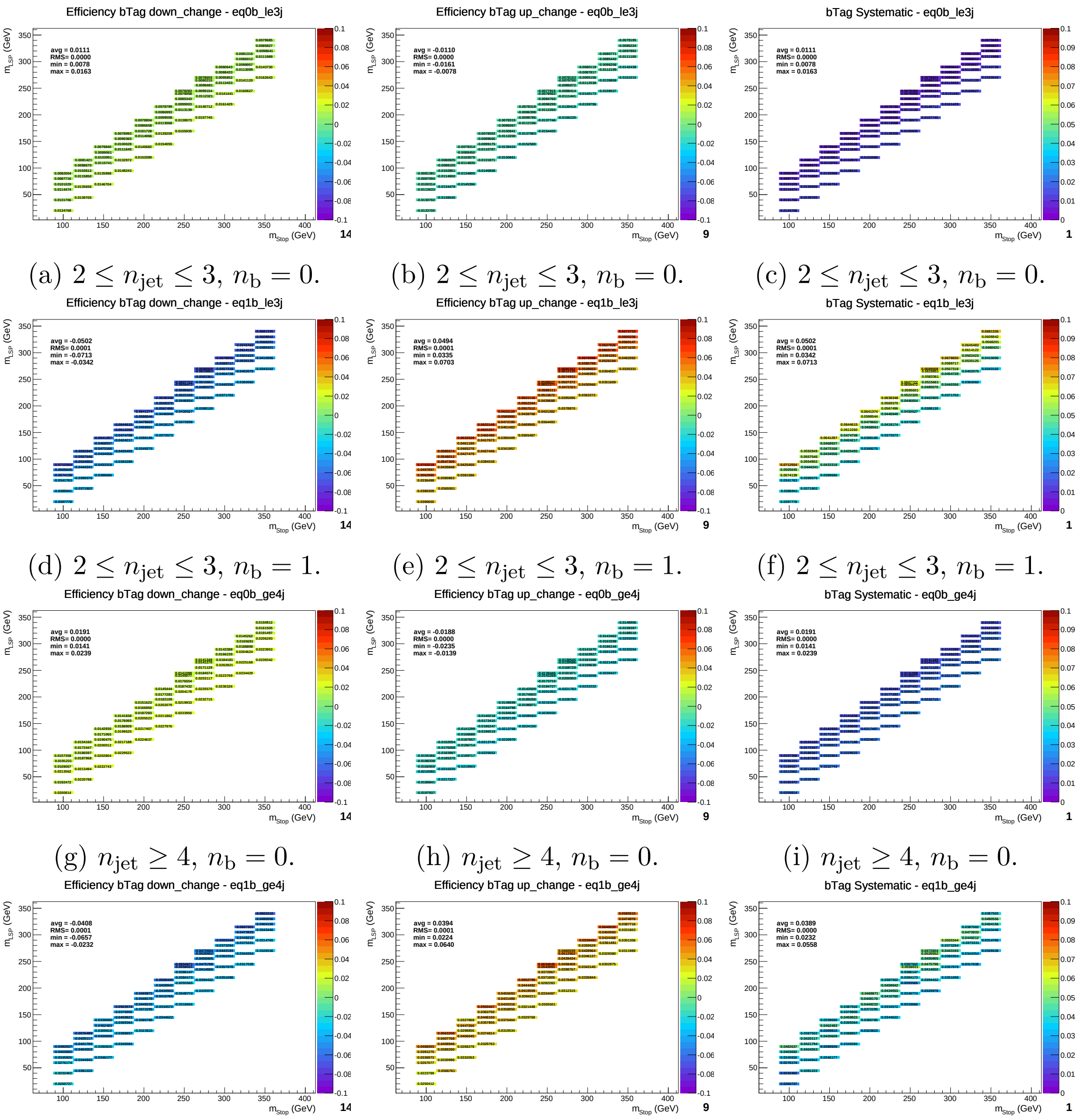

(a) $2 \leq n_{\mathrm{jet}} \leq 3$, $n_{\mathrm{b}} = 0$. (b) $2 \leq n_{\mathrm{jet}} \leq 3$, $n_{\mathrm{b}} = 0$. (c) $2 \leq n_{\mathrm{jet}} \leq 3$, $n_{\mathrm{b}} = 0$.

(d) $2 \leq n_{\mathrm{jet}} \leq 3$, $n_{\mathrm{b}} = 1$. (e) $2 \leq n_{\mathrm{jet}} \leq 3$, $n_{\mathrm{b}} = 1$. (f) $2 \leq n_{\mathrm{jet}} \leq 3$, $n_{\mathrm{b}} = 1$.

(g) $n_{\mathrm{jet}} \geq 4$, $n_{\mathrm{b}} = 0$. (h) $n_{\mathrm{jet}} \geq 4$, $n_{\mathrm{b}} = 0$. (i) $n_{\mathrm{jet}} \geq 4$, $n_{\mathrm{b}} = 0$.

(j) $n_{\mathrm{jet}} \geq 4$, $n_{\mathrm{b}} = 1$. (k) $n_{\mathrm{jet}} \geq 4$, $n_{\mathrm{b}} = 1$. (l) $n_{\mathrm{jet}} \geq 4$, $n_{\mathrm{b}} = 1$.

Fig. A.4 The relative change in acceptance times signal efficiency for the charm decay model for downwards (left) and upwards (middle) fluctuations of global event weight according to the uncertainties of the Btag scale factors, and the derived systematic values (right). Each set of plots corresponds to one of the four most sensitive analysis categories (n_{b}, n_{jet}), with the inclusive requirement H_T >200 GeV.

$\not{H}_T/\not{E}_T$ cut

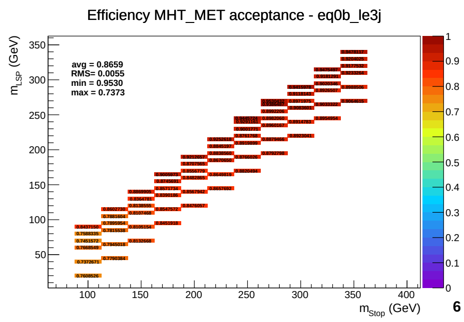

(a) $2 \leq n_{\text{jet}} \leq 3$, $n_{\text{b}} = 0$.

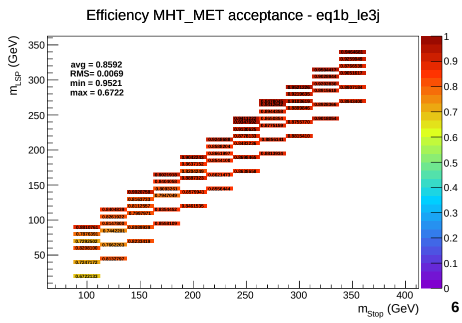

(b) $2 \leq n_{\text{jet}} \leq 3$, $n_{\text{b}} = 1$.

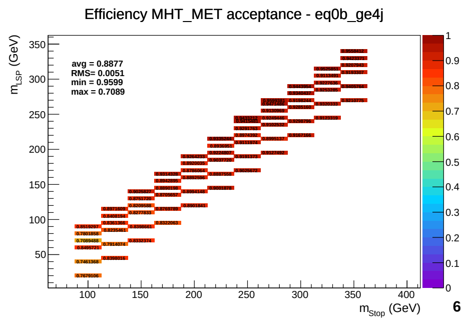

(c) $n_{\text{jet}} \geq 4$, $n_{\text{b}} = 0$.

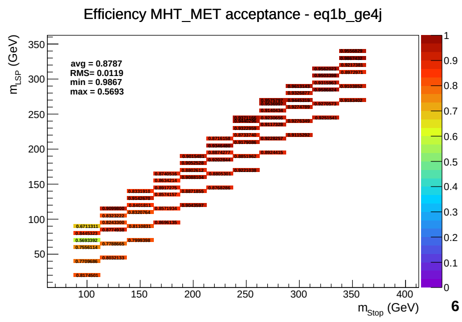

(d) $n_{\text{jet}} \geq 4$, $n_{\text{b}} = 1$.

Fig. A.5 The acceptance of the $\not{H}_T/\not{E}_T$ cut as a function of the charm decay model mass plane. Each plot represents one of the four most sensitive analysis cateogires (n_{b}, n_{jet}), with the inclusive requirement H_T >200 GeV.

Dead ECAL cut

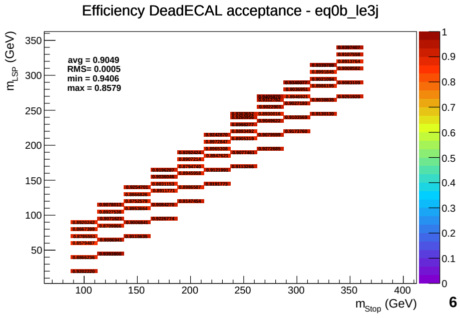

(a) $2 \leq n_{\rm jet} \leq 3$, $n_{\rm b} = 0$.

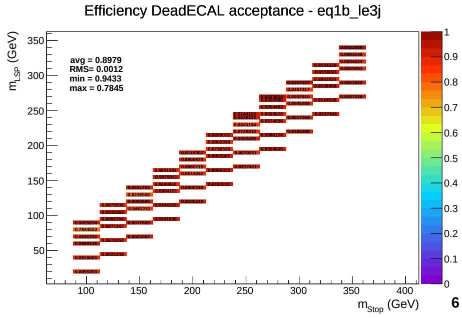

(b) $2 \leq n_{\rm jet} \leq 3$, $n_{\rm b} = 1$.

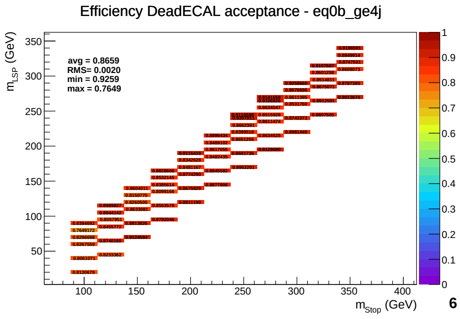

(c) $n_{\rm jet} \geq 4$, $n_{\rm b} = 0$.

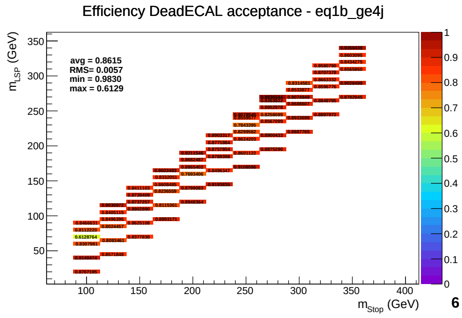

(d) $n_{\rm jet} \geq 4$, $n_{\rm b} = 1$.

Fig. A.6 The acceptance of the DeadECAL cut as a function of the charm decay model mass plane. Each plot represents one of the four most sensitive analysis cateogires ($n_{\rm b}$, $n_{\rm jet}$), with the inclusive requirement H_T >200 GeV.

Total systematic error

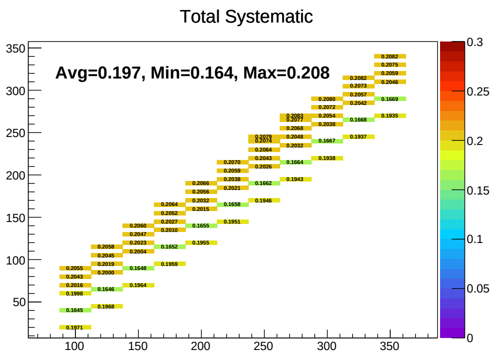

(a) $2 \leq n_{\rm jet} \leq 3$, $n_{\rm b} = 0$.

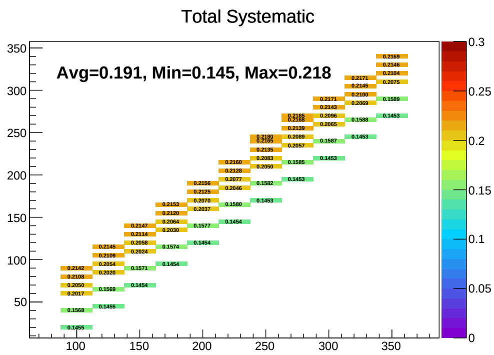

(b) $2 \leq n_{\rm jet} \leq 3$, $n_{\rm b} = 1$.

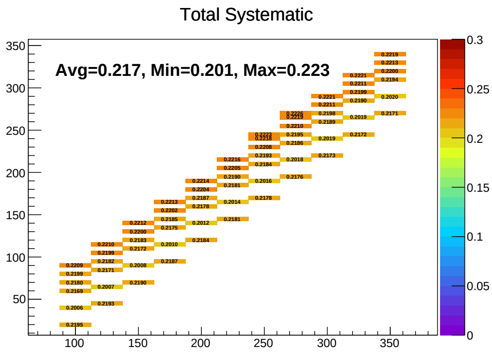

(c) $n_{\rm jet} \geq 4$, $n_{\rm b} = 0$.

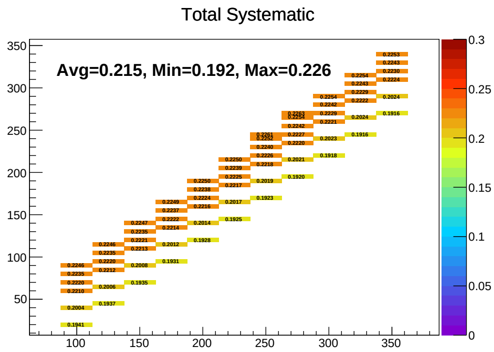

(d) $n_{\rm jet} \geq 4$, $n_{\rm b} = 1$.

Fig. A.7 The total systematic uncertainty as a function of the charm decay model plane, where all individual systematic contributions are summed in quadrature. Each plot represents one of the four most sensitive analysis cateogires ($n_{\rm b}$, $n_{\rm jet}$), with the inclusive requirement H_T >200 GeV.

Four-body decay

Jet Energy Scale

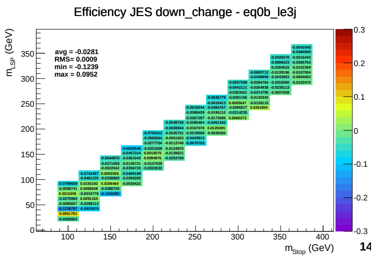

(a) $n_{\text{jet}} \geq 2$, $n_{\text{b}} \geq 0$.

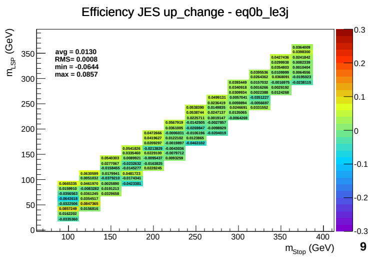

(b) $n_{\text{jet}} \geq 2$, $n_{\text{b}} \geq 0$.

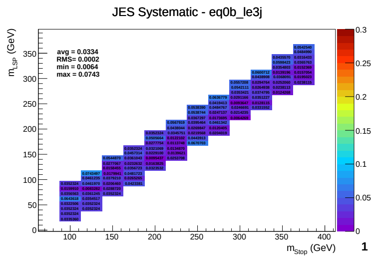

(c) $n_{\text{jet}} \geq 2$, $n_{\text{b}} \geq 0$.

Fig. A.8 The relative change in acceptance times signal efficiency for the four-body decay model for downwards (left) and upwards (middle) fluctuations of all jet energies by the uncertainty of the jet energy scale, and the derived systematic values (right). The plots represent a fully inclusive selection - $n_{\text{jet}} \geq 2$, $n_{\text{b}} \geq 0$ and H_T >200 GeV.

Initial State Radiation

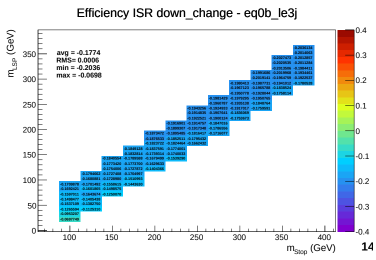

(a) $2 \le n_{\mathrm{jet}} \le 3,\ n_{\mathrm{b}} = 0.$

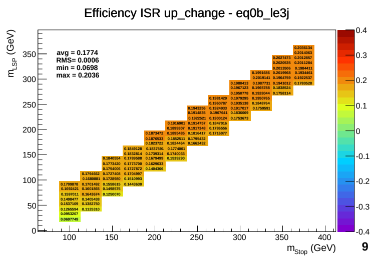

(b) $2 \le n_{\mathrm{jet}} \le 3,\ n_{\mathrm{b}} = 0.$

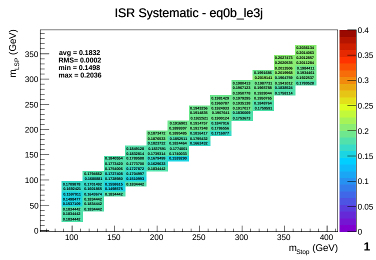

(c) $2 \le n_{\mathrm{jet}} \le 3,\ n_{\mathrm{b}} = 0.$

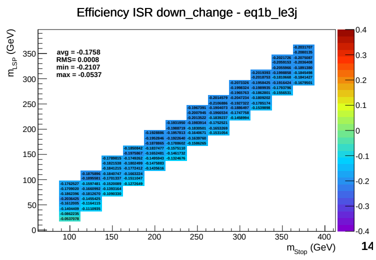

(d) $2 \le n_{\mathrm{jet}} \le 3,\ n_{\mathrm{b}} = 1.$

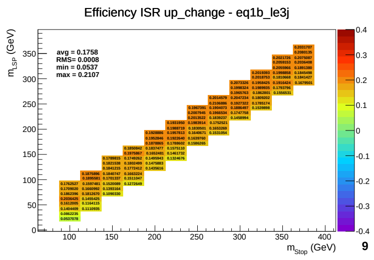

(e) $2 \le n_{\mathrm{jet}} \le 3,\ n_{\mathrm{b}} = 1.$

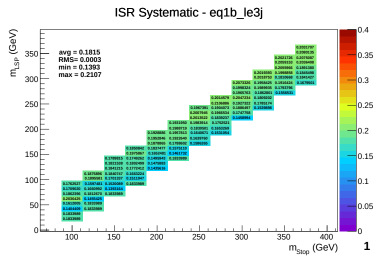

(f) $2 \le n_{\mathrm{jet}} \le 3,\ n_{\mathrm{b}} = 1.$

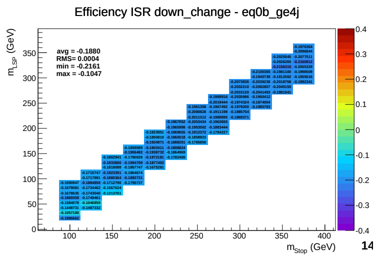

(g) $n_{\mathrm{jet}} \ge 4,\ n_{\mathrm{b}} = 0.$

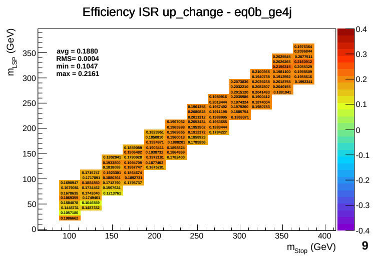

(h) $n_{\mathrm{jet}} \ge 4,\ n_{\mathrm{b}} = 0.$

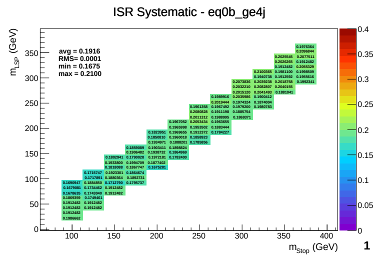

(i) $n_{\mathrm{jet}} \ge 4,\ n_{\mathrm{b}} = 0.$

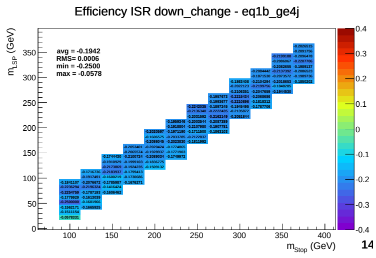

(j) $n_{\mathrm{jet}} \ge 4,\ n_{\mathrm{b}} = 1.$

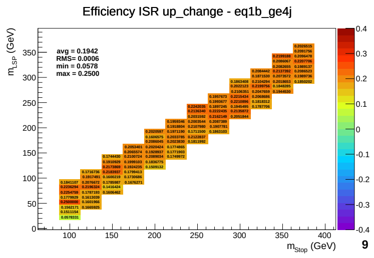

(k) $n_{\mathrm{jet}} \ge 4,\ n_{\mathrm{b}} = 1.$

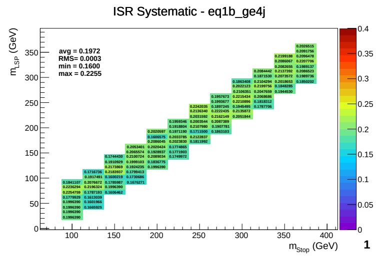

(l) $n_{\mathrm{jet}} \ge 4,\ n_{\mathrm{b}} = 1.$

Fig. A.9 The relative change in acceptance times signal efficiency for the four-body decay model for downwards (left) and upwards (middle) fluctuations of the global event weight equal to the magnitude of the ISR corrections, and the derived systematic values (right). Each set of plots corresponds to one of the four most sensitive analysis categories (n_{b}, n_{jet}), with the inclusive requirement H_T >200 GeV.

B-tag Scale Factor

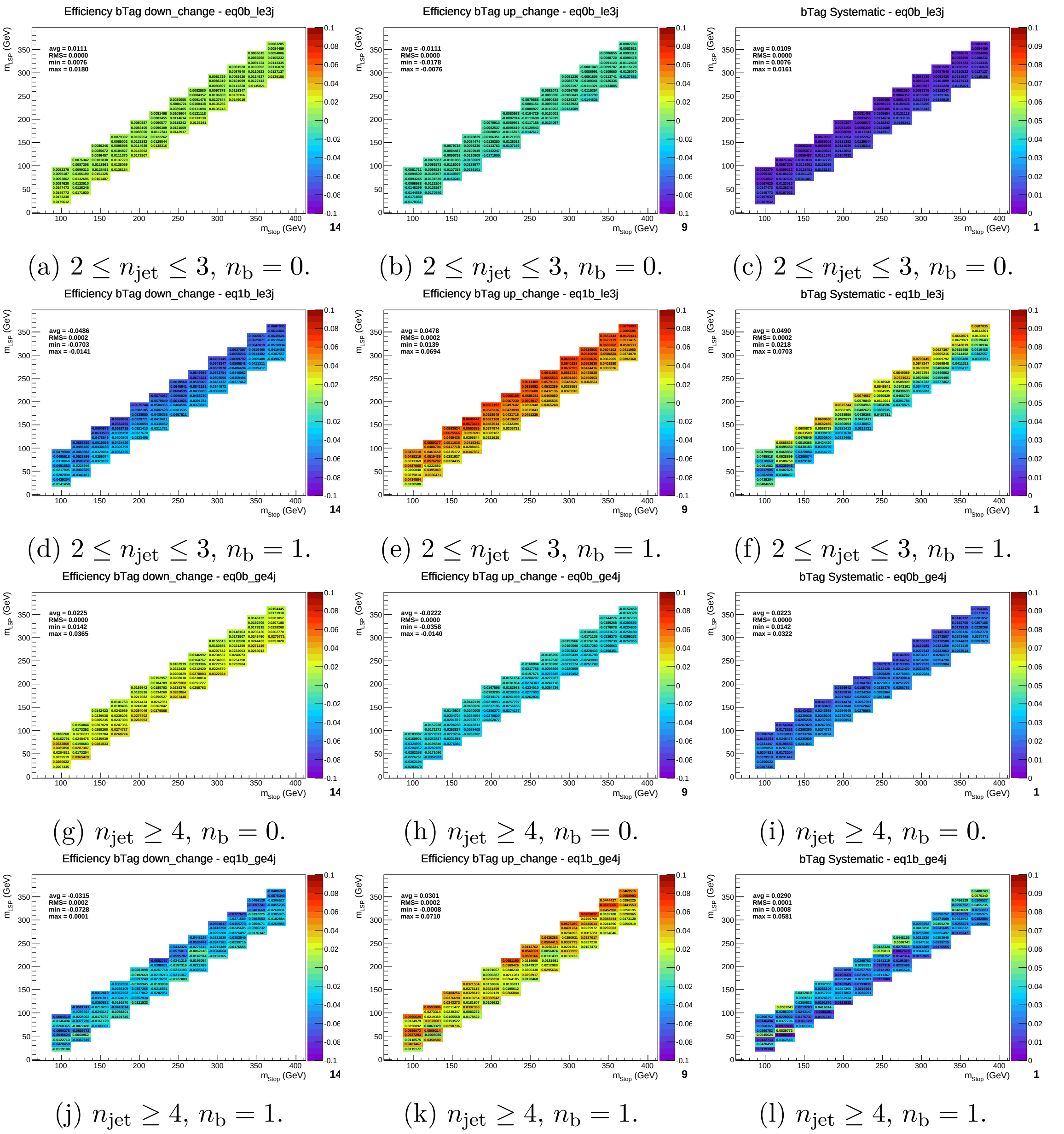

(a) $2 \le n_{\text{jet}} \le 3$, $n_{\text{b}} = 0$. (b) $2 \le n_{\text{jet}} \le 3$, $n_{\text{b}} = 0$. (c) $2 \le n_{\text{jet}} \le 3$, $n_{\text{b}} = 0$.

(d) $2 \le n_{\text{jet}} \le 3$, $n_{\text{b}} = 1$. (e) $2 \le n_{\text{jet}} \le 3$, $n_{\text{b}} = 1$. (f) $2 \le n_{\text{jet}} \le 3$, $n_{\text{b}} = 1$.

(g) $n_{\text{jet}} \ge 4$, $n_{\text{b}} = 0$. (h) $n_{\text{jet}} \ge 4$, $n_{\text{b}} = 0$. (i) $n_{\text{jet}} \ge 4$, $n_{\text{b}} = 0$.

(j) $n_{\text{jet}} \ge 4$, $n_{\text{b}} = 1$. (k) $n_{\text{jet}} \ge 4$, $n_{\text{b}} = 1$. (l) $n_{\text{jet}} \ge 4$, $n_{\text{b}} = 1$.

Fig. A.10 The relative change in acceptance times signal efficiency for the four-body decay model for downwards (left) and upwards (middle) fluctuations of global event weight according to the uncertainties of the Btag scale factors, and the derived systematic values (right). Each set of plots corresponds to one of the four most sensitive analysis categories (n_{b}, n_{jet}), with the inclusive requirement H_T >200 GeV.

$\not{H}_T/\not{E}_T$ cut

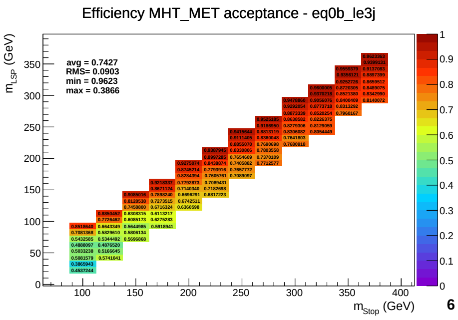

(a) $2 \leq n_{\mathrm{jet}} \leq 3$, $n_{\mathrm{b}} = 0$.

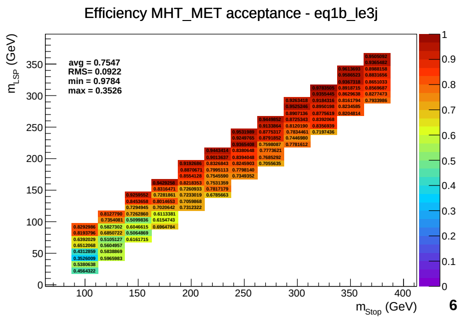

(b) $2 \leq n_{\mathrm{jet}} \leq 3$, $n_{\mathrm{b}} = 1$.

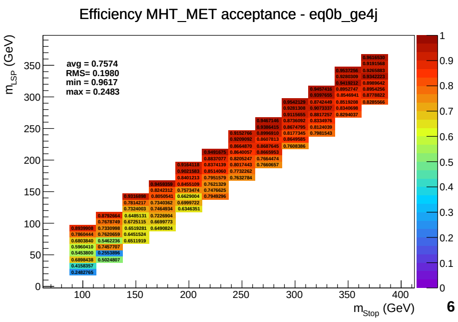

(c) $n_{\mathrm{jet}} \geq 4$, $n_{\mathrm{b}} = 0$.

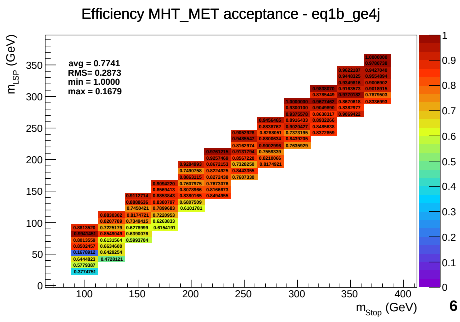

(d) $n_{\mathrm{jet}} \geq 4$, $n_{\mathrm{b}} = 1$.

Fig. A.11 The acceptance of the $\not{H}_T/\not{E}_T$ cut as a function of the four-body decay model mass plane. Each plot represents one of the four most sensitive analysis cateogires (n_{b}, n_{jet}), with the inclusive requirement H_T >200 GeV.

Dead ECAL cut

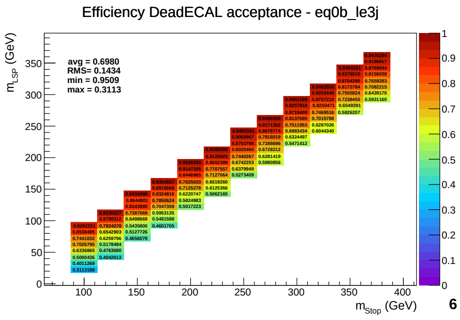

(a) $2 \leq n_{\mathrm{jet}} \leq 3$, $n_{\mathrm{b}} = 0$.

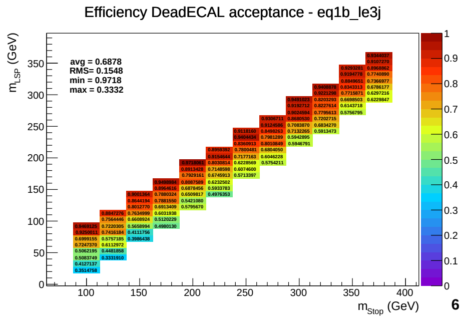

(b) $2 \leq n_{\mathrm{jet}} \leq 3$, $n_{\mathrm{b}} = 1$.

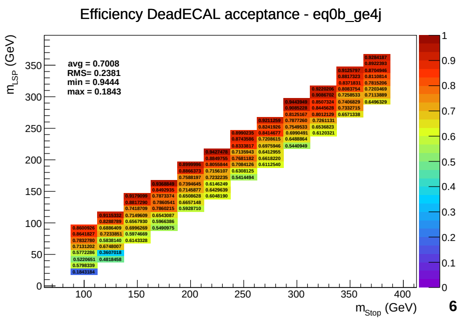

(c) $n_{\mathrm{jet}} \geq 4$, $n_{\mathrm{b}} = 0$.

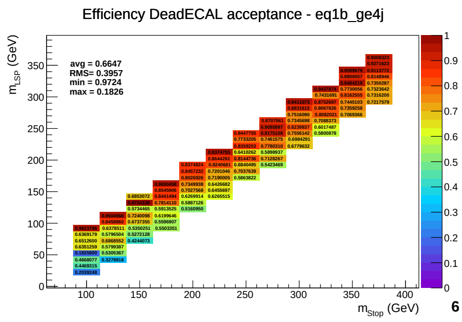

(d) $n_{\mathrm{jet}} \geq 4$, $n_{\mathrm{b}} = 1$.

Fig. A.12 The acceptance of the DeadECAL cut as a function of the four-body decay model mass plane. Each plot represents one of the four most sensitive analysis cateogires (n_{b}, n_{jet}), with the inclusive requirement H_T >200 GeV.

Total systematic error

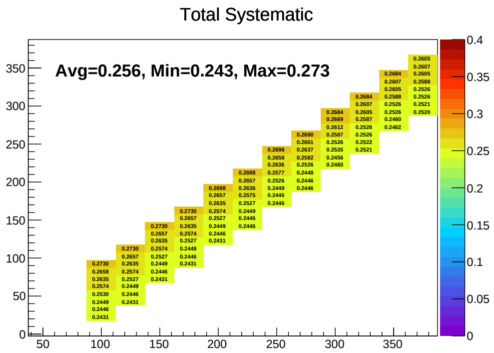

(a) $2 \leq n_{\text{jet}} \leq 3$, $n_{\text{b}} = 0$.

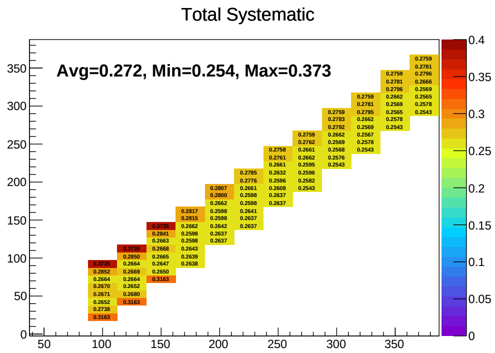

(b) $2 \leq n_{\text{jet}} \leq 3$, $n_{\text{b}} = 1$.

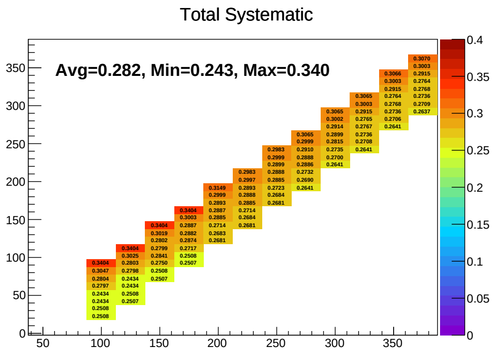

(c) $n_{\text{jet}} \geq 4$, $n_{\text{b}} = 0$.

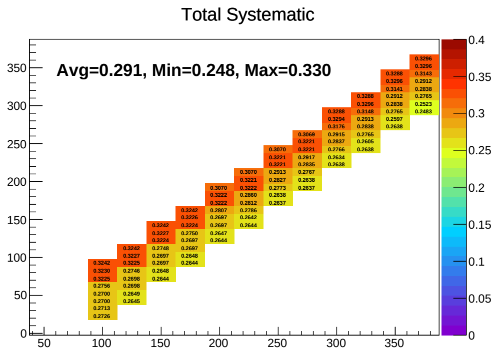

(d) $n_{\text{jet}} \geq 4$, $n_{\text{b}} = 1$.

Fig. A.13 The total systematic uncertainty as a function of the four-body decay model mass plane, where all individual systematic contributions are summed in quadrature. Each plot represents one of the four most sensitive analysis cateogires (n_{b}, n_{jet}), with the inclusive requirement H_T >200 GeV.

Bibliography

[1] S. P. Martin, “A Supersymmetry primer”, *Adv.Ser.Direct.High Energy Phys.* **21** (2010) 1–153, `doi:10.1142/9789814307505_0001`, `arXiv:hep-ph/9709356`.

[2] https://twiki.cern.ch/twiki/bin/view/CMSPublic/PhysicsResultsSUS.

[3] https://twiki.cern.ch/twiki/bin/view/AtlasPublic/SupersymmetryPublicResults.

[4] CERN. http://te-epc-lpc.web.cern.ch/te-epc-lpc/machines/lhc/general.stm. Accessed: 2015-06-10.

[5] V. Frigo, “LHC structure.. Structure LHC.”, (Jan, 1997). AC Collection. Legacy of AC. Pictures from 1992 to 2002.

[6] CMS Collaboration, “CMS Luminosity - Public Results”,.

[7] T. Sakuma and T. McCauley, “Detector and Event Visualization with SketchUp at the CMS Experiment”, *J.Phys.Conf.Ser.* **513** (2014) 022032, `doi:10.1088/1742-6596/513/2/022032`, `arXiv:1311.4942`.

[8] CMS Collaboration Collaboration, G. L. Bayatian et al., “CMS Physics: Technical Design Report Volume 1: Detector Performance and Software”. Technical Design Report CMS. CERN, Geneva, 2006.

[9] CMS Collaboration Collaboration, G. L. Bayatyan et al., “CMS TriDAS project: Technical Design Report, Volume 1: The Trigger Systems”. Technical Design Report CMS. 2002.

[10] CMS Collaboration Collaboration, “Performance of b tagging at sqrt(s)=8 TeV in multijet, ttbar and boosted topology events”, CMS-PAS-BTV-13-001, CERN, Geneva, (2013).

[11] D. Olivito, F. Wurthwein et al., “Hadronic Recoil Studies of Heavy Boosted Systems”, (2012). CMS AN-2013/059.

[12] Particle Data Group Collaboration, “Review of Particle Physics”, *Chin.Phys.* **C38** (2014) 090001, `doi:10.1088/1674-1137/38/9/090001`.

[13] ALEPH, CDF, D0, DELPHI, L3, OPAL, SLD, LEP Electroweak Working Group, Tevatron Electroweak Working Group, SLD Electroweak and Heavy Flavour Groups Collaboration, “Precision Electroweak Measurements and Constraints on the Standard Model”, `arXiv:1012.2367`.

[14] S. L. Glashow, “Partial-Symmetries of Weak Interactions”, *Nuclear Physics* **22** (1961), no. 4, 579 – 588, `doi:http://dx.doi.org/10.1016/0029-5582(61)90469-2`.

[15] S. Weinberg, “A Model of Leptons”, *Phys. Rev. Lett.* **19** (Nov, 1967) 1264–1266, `doi:10.1103/PhysRevLett.19.1264`.

[16] A. Salam, “Weak and Electromagnetic Interactions”, *Conf.Proc.* **C680519** (1968) 367–377.

[17] H. D. Politzer, “Reliable Perturbative Results for Strong Interactions?”, *Phys. Rev. Lett.* **30** (Jun, 1973) 1346–1349, `doi:10.1103/PhysRevLett.30.1346`.

[18] D. J. Gross and F. Wilczek, “Ultraviolet Behavior of Non-Abelian Gauge Theories”, *Phys. Rev. Lett.* **30** (Jun, 1973) 1343–1346, `doi:10.1103/PhysRevLett.30.1343`.

[19] B. Martin and G. Shaw, “Particle Physics”. John Wiley and Sons, Ltd., third edition, 2009.

[20] F. Englert and R. Brout, “Broken Symmetry and the Mass of Gauge Vector Mesons”, *Phys. Rev. Lett.* **13** (Aug, 1964) 321–323, `doi:10.1103/PhysRevLett.13.321`.

[21] P. W. Higgs, “Broken Symmetries and the Masses of Gauge Bosons”, *Phys. Rev. Lett.* **13** (Oct, 1964) 508–509, `doi:10.1103/PhysRevLett.13.508`.

[22] G. S. Guralnik, C. R. Hagen, and T. W. B. Kibble, “Global Conservation Laws and Massless Particles”, *Phys. Rev. Lett.* **13** (Nov, 1964) 585–587, `doi:10.1103/PhysRevLett.13.585`.

[23] Gfitter Group Collaboration, “The global electroweak fit at NNLO and prospects for the LHC and ILC”, *Eur.Phys.J.* **C74** (2014) 3046, `doi:10.1140/epjc/s10052-014-3046-5`, `arXiv:1407.3792`.

[24] A. Riotto and M. Trodden, "Recent progress in baryogenesis", *Ann.Rev.Nucl.Part.Sci.* **49** (1999) 35–75, doi:10.1146/annurev.nucl.49.1.35, arXiv:hep-ph/9901362.

[25] W.-S. Hou, "Source of CP Violation for the Baryon Asymmetry of the Universe", *Chin.J.Phys.* **47** (2009) 134, arXiv:0803.1234.

[26] Y. Fukuda et al., "Evidence for Oscillation of Atmospheric Neutrinos", *Phys. Rev. Lett.* **81** (Aug, 1998) 1562–1567, doi:10.1103/PhysRevLett.81.1562.

[27] Q. R. Ahmad et al., "Measurement of Day and Night Neutrino Energy Spectra at SNO and Constraints on Neutrino Mixing Parameters", *Phys. Rev. Lett.* **89** (Jun, 2002) 011302, doi:10.1103/PhysRevLett.89.011302.

[28] G. Altarelli and F. Feruglio, "Theoretical models of neutrino masses and mixings", *Springer Tracts Mod.Phys.* **190** (2003) 169–207, doi:10.1007/978-3-540-44901-0_6, arXiv:hep-ph/0206077.

[29] ATLAS Collaboration and CMS Collaboration Collaboration, "Combined Measurement of the Higgs Boson Mass in pp Collisions at $\sqrt{s} = 7$ and 8 TeV with the ATLAS and CMS Experiments", *Phys. Rev. Lett.* **114** (May, 2015) 191803, doi:10.1103/PhysRevLett.114.191803.

[30] G. Bertone, D. Hooper, and J. Silk, "Particle dark matter: Evidence, candidates and constraints", *Phys.Rept.* **405** (2005) 279–390, doi:10.1016/j.physrep.2004.08.031, arXiv:hep-ph/0404175.

[31] D. Clowe et al., "A direct empirical proof of the existence of dark matter", *Astrophys.J.* **648** (2006) L109–L113, doi:10.1086/508162, arXiv:astro-ph/0608407.

[32] Y. A. Gol'fand and E. P. Likhtman, "Extension of the Algebra of Poincaré Group Generators and Violation of p Invariance", *JETP Lett.* **13** (1971) 323.

[33] J. Wess and B. Zumino, "Supergauge transformations in four dimensions", *Nucl. Phys. B* **70** (1974) 39, doi:10.1016/0550-3213(74)90355-1.

[34] H. P. Nilles, "Supersymmetry, Supergravity and Particle Physics", *Phys. Reports* **110** (1984) 1, doi:10.1016/0370-1573(84)90008-5.

[35] H. Haber and G. Kane, “The Search for Supersymmetry: Probing Physics Beyond the Standard Model”, *Phys. Reports* **117** (1987) 75, doi:10.1016/0370-1573(85)90051-1.

[36] R. Barbieri, S. Ferrara, and C. A. Savoy, “Gauge Models with Spontaneously Broken Local Supersymmetry”, *Phys. Lett. B* **119** (1982) 343, doi:10.1016/0370-2693(82)90685-2.

[37] S. Dawson, E. Eichten, and C. Quigg, “Search for Supersymmetric Particles in Hadron - Hadron Collisions”, *Phys. Rev. D* **31** (1985) 1581, doi:10.1103/PhysRevD.31.1581.

[38] S. Dimopoulos and D. W. Sutter, “The Supersymmetric flavor problem”, *Nucl.Phys.* **B452** (1995) 496–512, doi:10.1016/0550-3213(95)00421-N, arXiv:hep-ph/9504415.

[39] E. Witten, “Dynamical Breaking of Supersymmetry”, *Nucl. Phys. B* **188** (1981) 513, doi:10.1016/0550-3213(81)90006-7.

[40] S. Dimopoulos and H. Georgi, “Softly Broken Supersymmetry and SU(5)”, *Nucl. Phys. B* **193** (1981) 150, doi:10.1016/0550-3213(81)90522-8.

[41] G. R. Farrar and P. Fayet, “Phenomenology of the production, decay, and detection of new hadronic states associated with supersymmetry”, *Physics Letters B* **76** (1978), no. 5, 575 – 579, doi:http://dx.doi.org/10.1016/0370-2693(78)90858-4.

[42] G. Jungman, M. Kamionkowski, and K. Griest, “Supersymmetric dark matter”, *Phys.Rept.* **267** (1996) 195–373, doi:10.1016/0370-1573(95)00058-5, arXiv:hep-ph/9506380.

[43] R. Barbieri and D. Pappadopulo, “S-particles at their naturalness limits”, *JHEP* **10** (2009) 061, doi:10.1088/1126-6708/2009/10/061.

[44] M. Carena, G. Nardini, M. Quiros, and C. E. Wagner, “The Effective Theory of the Light Stop Scenario”, *JHEP* **0810** (2008) 062, doi:10.1088/1126-6708/2008/10/062, arXiv:0806.4297.

[45] M. Papucci, J. T. Ruderman, and A. Weiler, “Natural SUSY Endures”, *JHEP* **1209** (2012) 035, doi:10.1007/JHEP09(2012)035, arXiv:1110.6926.

[46] G. L. Kane, C. F. Kolda, L. Roszkowski, and J. D. Wells, "Study of constrained minimal supersymmetry", *Phys.Rev.* **D49** (1994) 6173–6210, doi:10.1103/PhysRevD.49.6173, arXiv:hep-ph/9312272.

[47] J. R. Ellis, K. A. Olive, and Y. Santoso, "Constraining supersymmetry", *New J.Phys.* **4** (2002) 32, doi:10.1088/1367-2630/4/1/332, arXiv:hep-ph/0202110.

[48] J. Alwall, P. C. Schuster, and N. Toro, "Simplified models for a first characterization of new physics at the LHC", *Phys. Rev. D* **79** (Apr, 2009) 075020, doi:10.1103/PhysRevD.79.075020.

[49] LHC New Physics Working Group Collaboration, "Simplified Models for LHC New Physics Searches", *J.Phys.* **G39** (2012) 105005, doi:10.1088/0954-3899/39/10/105005, arXiv:1105.2838.

[50] C. Collaboration, "Interpretation of searches for supersymmetry with simplified models", *Phys. Rev. D* **88** (Sep, 2013) 052017, doi:10.1103/PhysRevD.88.052017.

[51] C. Boehm, A. Djouadi, and Y. Mambrini, "Decays of the lightest top squark", *Phys.Rev.* **D61** (2000) 095006, doi:10.1103/PhysRevD.61.095006, arXiv:hep-ph/9907428.

[52] WMAP Collaboration, "First year Wilkinson Microwave Anisotropy Probe (WMAP) observations: Determination of cosmological parameters", *Astrophys.J.Suppl.* **148** (2003) 175–194, doi:10.1086/377226, arXiv:astro-ph/0302209.

[53] C. Balazs, M. Carena, and C. Wagner, "Dark matter, light stops and electroweak baryogenesis", *Phys.Rev.* **D70** (2004) 015007, doi:10.1103/PhysRevD.70.015007, arXiv:hep-ph/0403224.

[54] S. P. Martin, "Compressed supersymmetry and natural neutralino dark matter from top squark-mediated annihilation to top quarks", *Phys.Rev.* **D75** (2007) 115005, doi:10.1103/PhysRevD.75.115005, arXiv:hep-ph/0703097.

[55] L. Evans and P. Bryant, "LHC Machine", *JINST* **3** (2008) S08001, doi:10.1088/1748-0221/3/08/S08001.

[56] CMS Collaboration, "The CMS experiment at the CERN LHC", *JINST* **3** (2008) S08004, doi:10.1088/1748-0221/3/08/S08004.

[57] C. Eck et al., "LHC computing Grid: Technical Design Report. Version 1.06 (20 Jun 2005)". Technical Design Report LCG. CERN, Geneva, 2005.

[58] M. Cacciari, G. P. Salam, and G. Soyez, "The anti-k_{T} jet clustering algorithm", *JHEP* **04** (2008) 063, doi:10.1088/1126-6708/2008/04/063.

[59] CMS Collaboration, "Jet ID". https://twiki.cern.ch/twiki/bin/viewauth/CMS/JetID.

[60] CMS Collaboration, "Jet Energy Scale". https://twiki.cern.ch/twiki/bin/view/CMS/JetEnergyScale.

[61] CMS Collaboration, "Determination of jet energy calibration and transverse momentum resolution in CMS", *Journal of Instrumentation* **6** (November, 2011) 11002, doi:10.1088/1748-0221/6/11/P11002, arXiv:1107.4277.

[62] M. Cacciari and G. P. Salam, "Pileup subtraction using jet areas", *Physics Letters B* **659** (2008) 119 – 126, doi:10.1016/j.physletb.2007.09.077.

[63] M. Cacciari, G. P. Salam, and G. Soyez, "The catchment area of jets", *Journal of High Energy Physics* **2008** (2008), no. 04, 005.

[64] CMS Collaboration, "Determination of Jet Energy Calibration and Transverse Momentum Resolution in CMS", *JINST* **6** (2011) P11002, doi:10.1088/1748-0221/6/11/P11002, arXiv:1107.4277.

[65] CMS Collaboration, "Identification of b-quark jets with the CMS experiment", *JINST* **8** (2013) P04013, doi:10.1088/1748-0221/8/04/P04013.

[66] CMS Collaboration, "Baseline Muon ID". https://twiki.cern.ch/twiki/bin/view/CMSPublic/SWGuideMuonId.

[67] CMS Collaboration, "Photon ID". https://twiki.cern.ch/twiki/bin/view/CMS/PhotonIDAnalysis.

[68] CMS Collaboration, "Electron ID". https://twiki.cern.ch/twiki/bin/view/CMSPublic/SWGuideCutBasedElectronID.

[69] http://cms.cern.ch/iCMS/jsp/db_notes/noteInfo.jsp?cmsnoteid=CMSAN-2013/089. Search for Direct Top Squark Pair Production in the Single Lepton Channel with Transverse Mass at 8 TeV, CMS AN-2013/089.

[70] A. Giammanco, “The Fast Simulation of the CMS Experiment”, *Journal of Physics: Conference Series* **513** (2014), no. 2, 022012.

[71] R. Bainbridge, S. A. Koay, “DY+jets at 8TeV: comparison of HT and Njet binned samples”. https://indico.cern.ch/event/271369/.

[72] A. Agapitos et al., “Search for supersymmetry in final states with missing transverse energy and 0, 1, 2, 3, or ≥ 4 b-quark jets in 8 TeV pp collisions using the variable α_T”, (2012). CMS AN-2012/356.

[73] L. Randall and D. Tucker-Smith, “Dijet Searches for Supersymmetry at the LHC”, *Phys.Rev.Lett.* **101** (2008) 221803, doi:10.1103/PhysRevLett.101.221803, arXiv:0806.1049.

[74] CMS Collaboration Collaboration, “SUSY searches with dijet events”, CMS-PAS-SUS-08-005, CERN, 2008. Geneva, (Oct, 2008).

[75] CMS Collaboration, “Search strategy for exclusive multi-jet events from supersymmetry at CMS”, CMS-PAS-SUS-09-001, CERN, 2009. Geneva, (Jul, 2009).

[76] R. Cousins, “Probability Density Functions for Positive Nuisance Parameters”. http://www.physics.ucla.edu/~cousins/stats/cousins_lognormal_prior.pdf.

[77] W. Verkerke and D. Kirkby, “RooFit”. http://root.cern.ch/drupal/content/roofit.

[78] F. James and M. Roos, “Minuit: A System for Function Minimization and Analysis of the Parameter Errors and Correlations”, *Comput.Phys.Commun.* **10** (1975) 343–367, doi:10.1016/0010-4655(75)90039-9.

[79] https://twiki.cern.ch/twiki/bin/viewauth/CMS/BtagPOG.

[80] M. Botje, J. Butterworth, A. Cooper-Sarkar et al., “The PDF4LHC Working Group Interim Recommendations”, (2011). arXiv:1101.0538.

[81] CMS Collaboration, “CMS Luminosity Based on Pixel Cluster Counting - Summer 2013 Update”,.

[82] A. L. Read, “Presentation of search results: the CL s technique”, *Journal of Physics G: Nuclear and Particle Physics* **28** (2002), no. 10, 2693.